

Applications of Surface Plasmon Resonance Effect based on Gold nanoparticles

A Thesis submitted to the University of Strathclyde for
the degree of

Doctor of Philosophy by

Peng Gu

Photophysics Research Group

Department of Physics

University of Strathclyde, Glasgow

2018

‘This Thesis is the result of the author’s original research. It has been composed by the author and has not been previously submitted for examination which has led to the award of a degree.’

‘The copyright of this Thesis belongs to the author under the terms of the United Kingdom Copyright Acts as qualified by University of Strathclyde Regulation 3.50. Due acknowledgment must always be made of the use of any material contained in, or derived from, this Thesis.’

Signed:

Date :

Abstract

Surface plasmon resonance is a photophysical phenomenon, which attracts broad interest with possible applications in sensing, nanolasers and electrochemical reaction catalysis. Meanwhile, gold nanoparticles are excellent candidates among all plasmonic noble metals, showing good and controllable plasmonic features. The aim of this thesis is to study the unique optical properties of gold nanoparticles and gold composites and demonstrate the energy transfer in plasmon enhanced fluorescence, SPASER and oxygen evolution reaction (OER) catalysis *via* microscopic and spectroscopic techniques.

Firstly, synthesis of colloid gold nanoparticles was introduced in Chapter 3. Surface modifications of gold with silica and polymers were also discussed in this part as well as 2D MnO₂ nanosheets fabrication. In addition, the function of each reaction reagents was also explained as well as the development background of each synthetic method.

Then in Chapter 4, the surface plasmon effect on the energy transfer towards SPASER was investigated with a Rh 800 doped polystyrene-gold nanorod core-shell structure. The steady state and time-resolved fluorescence spectroscopy study disclosed an enhanced energy transfer when the longitudinal surface

plasmon mode of the gold nanorods overlapped with the absorption and emission of Rh 800.

Further study was performed on the metal enhanced fluorescence employing Mega 520 dye loaded mesoporous silica coated gold nanorods in Chapter 5. Fluorescence enhancement was found arising from both increased excitation rate as the transverse surface plasmon mode of gold nanorods overlapped with the excitation wavelength and enhanced quantum yield when the emission of the dye was not coincident with the longitudinal plasmon mode. Furthermore, this study revealed the distance dependence of the enhancement effect.

Finally in Chapter 6, a gold-MnO₂ catalyst was designed and prepared with excellent OER catalytic performance. It is believed that the plasmon-induced Mnⁿ⁺ species provide active sites to extract electrons from OH⁻ to facilitate the oxygen evolution. By tuning the laser intensity from 100 to 200 mW, the overpotential was decreased from 0.38 to 0.32 V, which was comparable to IrO₂ and RuO₂ catalysts.

Table of Contents

| | |
|--|----|
| 1. Introduction | 1 |
| 1.1. Localized Surface Plasmon Resonance | 2 |
| 1.1.1. Mie Theory | 3 |
| 1.1.2. Gans Theory | 6 |
| 1.1.3. Photoluminescence of Gold nanoparticles | 7 |
| 1.2. Principle of Electrochemical Oxygen Catalysis | 9 |
| 1.2.1. Electrochemical Oxygen Catalysis | 9 |
| 1.2.2. Electrochemical Measurements | 14 |
| 2. Fluorescence | 19 |
| 2.1. General Principle of Fluorescence | 19 |
| 2.2. Fluorescence Quenching and Energy Transfer Models | 24 |
| 2.3. Plasmon Enhanced Fluorescence Process | 30 |
| 2.4. Time-correlated Single Photon Counting (TCSPC) | 33 |
| 2.5. Data analysis of fluorescence lifetime measurement | 38 |
| 2.6. SPASER Concept and Purcell Effect | 39 |
| 3. Synthetic Methods | 43 |
| 3.1. Introduction | 43 |
| 3.2. Synthesis of Gold nanoparticles | 44 |
| 3.2.1. Preparation of Gold nanospheres | 44 |
| 3.2.2. Preparation of Gold nanorods | 46 |
| 3.3. Preparation of Gold nanorods Core-shell nanostructures | 49 |
| 3.4. Preparation of Au-MnO₂ nanocomposite | 53 |
| 4. Dye-doped Polystyrene-coated GNRs towards SPASER | 57 |
| 4.1. Introduction | 57 |
| 4.2. Methods | 57 |
| 4.3. Results and Discussion | 58 |
| 4.3.1. PS-coated GNRs | 58 |
| 4.3.2. Rh 800 Doped PS-coated GNRs | 60 |
| 4.3.3. Influence of Surface Plasmon on Energy Transfer | 64 |
| 4.4. Conclusions | 67 |

| | |
|---|------------|
| 5. Revealing the Plasmon Enhanced Fluorescence by Mega 520/Silica Gold Nanorods..... | 69 |
| 5.1. Introduction..... | 69 |
| 5.2. Methods | 71 |
| 5.2.1. Preparation of the Mega 520 doped Silica-coated GNRs..... | 71 |
| 5.2.2. Preparation of the Mega 520 doped Silica Nanoparticles | 71 |
| 5.3. Results and Discussion | 72 |
| 5.4. Conclusions..... | 90 |
| 6. Plasmon-promoted electrochemical oxygen evolution catalysis | 92 |
| 6.1. Introduction..... | 92 |
| 6.2. Methods | 95 |
| 6.3. Results and Discussion | 97 |
| 6.4. Conclusions..... | 111 |
| 7. Summary and Outlook | 113 |
| Reference | 116 |
| Acknowledgement | 138 |
| Publication List | 139 |
| Abbreviations | 140 |

1. Introduction

The length scale of the electronic motion determines materials' properties. When size shrinks to nanometre scale, the electronic and chemical properties of a material change tremendously. In semiconductors at nanoscale, the property change is dominated by quantum confinement of the electronic motion. For noble metal nanoparticles, the coherent charge density oscillation can be excited and leads to an enhanced local electric field, which is called localized surface plasmon resonance. These unique features would provide great potential for the nanoparticles to be used in many applications, such as metal enhanced fluorescence, nanolasers, and electrochemical catalysis.

The overall aim of this project is to provide vital information regards the surface plasmon resonance for optical and electrochemical applications and investigate the chemical physics processes in nanoscale. Firstly, an introduction of fundamental principles of surface plasmon resonance, electrochemical oxygen catalysis and fluorescence techniques used in this project is presented in Chapters 1 and 2. After the introduction of synthetic methods in Chapter 3, the study on the surface plasmon energy transfer towards SPASER is included in Chapter 4, where a polystyrene-gold nanorod core-shell structure was used for the study. Chapter 5 reveals the metal enhanced fluorescence process from the system of Mega 520 dye loaded mesoporous silica coated gold nanorods. In Chapter 6, a gold-MnO₂ catalyst is prepared with excellent OER catalytic performance, and

possible working mechanism is proposed. Finally, in Chapter 7, a brief summary and outlook to future work are presented.

1.1. Localized Surface Plasmon Resonance

Localized surface plasmon resonance (LSPR) represents a collective coherent charge density oscillation confined to metal nanoparticles and metallic nanostructures (Figure 1.1 left), whose resonance wavelength is sensitive to permittivity changes of the environment, as well as to the size and shape of the nanoparticle.^[1-6] In addition, electric fields near the particle's surface are greatly enhanced as shown in Figure 1.1 right.^[7-12]

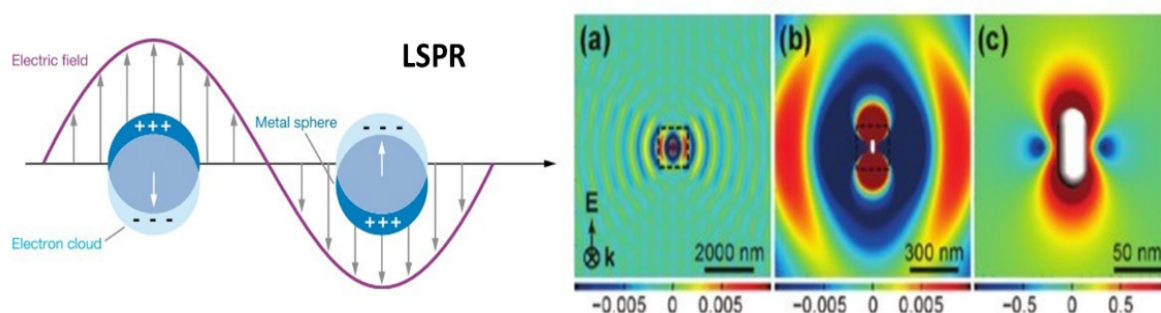


Figure 1.1 (Left) Schematic diagram illustrating a localized surface plasmon resonance.^[13] (Right) Spatial redistribution of the electric field intensity of a gold nanorod (GNR) was illuminated by a plane wave at the longitudinal plasmon resonance wavelength (a); (b) & (c) zoomed-in area of the dashed box in (a) and (b), respectively.^[7]

Compared to other nanocrystals, gold nanorods (GNRs) offer significant advantage as their LSPR properties can be tailored by synthetically tuning their

sizes and shapes. There are two plasmon modes in GNRs, as shown in Figure 1.2: the longitudinal mode (L mode) associated with the electron oscillations along the length axis, and the transverse mode (T mode) excited by light polarized along the transverse direction of the nanorod.^[10,14–18] The L mode is sensitive to the shape (aspect ratio, AR) of the particle and can be synthetically tuned across a broad spectral range covering the visible and near-infrared regions.^[19–21] To understand in depth how this LSPR works, we must turn to the Mie theory.

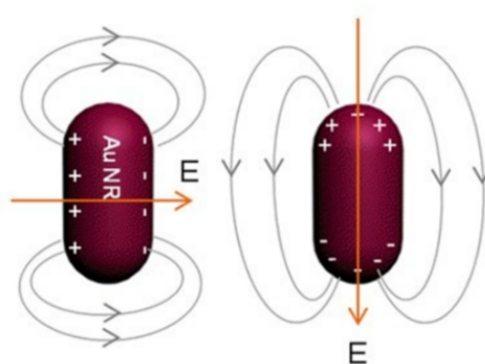


Figure 1.2 Schematic of transverse (left) and longitudinal (right) surface plasmon modes in gold nanorods.^[22]

1.1.1. Mie Theory

In 1908, Gustav Mie published his famous paper on developing an analytical solution on Maxwell's equations that described the scattering and absorption of light by spherical particles.^[19,23–25] This theory evolves rapidly in the following decade with many applications in plasmonic areas.^[26] Finding the scattered fields produced by an incident plane wave on a homogeneous conducting sphere results in the following total scattering, extinction and absorption cross-sections^[1,27]:

$$\sigma_{sca} = \frac{2\pi}{|k|^2} \sum_{L=1}^{\infty} (2L+1) (|a_L|^2 + |b_L|^2) \quad (1.1)$$

$$\sigma_{ext} = \frac{2\pi}{|k|^2} \sum_{L=1}^{\infty} (2L+1) [Re(a_L + b_L)] \quad (1.2)$$

$$\sigma_{abs} = \sigma_{ext} - \sigma_{sca} \quad (1.3)$$

where k is the incoming wavevector and L is integer representing the dipole, quadrupole and higher multipoles of the scattering. a_L and b_L are the parameters composed of Riccati-Bessel functions ψ_L and χ_L :

$$a_L = \frac{m\psi_L(mx)\psi'_L(x) - \psi'_L(mx)\psi_L(x)}{m\psi_L(mx)\chi'_L(x) - \psi'_L(mx)\chi_L(x)} \quad (1.4)$$

$$b_L = \frac{\psi_L(mx)\psi'_L(x) - m\psi'_L(mx)\psi_L(x)}{\psi_L(mx)\chi'_L(x) - m\psi'_L(mx)\chi_L(x)} \quad (1.5)$$

Here, $m = \tilde{n}/n_m$, where n_m is the permittivity of surrounding medium, $\tilde{n} = n_R + in_I$ is the complex permittivity of the metal. n_R and n_I are the real and imaginary permittivity of the metal, respectively. Also, $x = k_m r$, where r is the radius of the particle and k_m is the wavevector in the medium ($k_m = 2\pi/\lambda_m$) other than in vacuum.

To gain insight of the surface plasmon phenomena, simpler expressions are needed. As the nanoparticle is very small ($|m|x \ll 1$), then $|b_1| \ll |a_1|$. With this assumption, the amplitude scattering matrix elements are accurate to terms of x^3 , and Equation 1.4 and 1.5 can be simplified to^[26,27]:

$$a_1 \approx -\frac{i2x^3}{3} \frac{m^2-1}{m^2+2} \quad (1.6)$$

$$b_1 \approx 0 \quad (1.7)$$

and the higher order a_L and b_L are zero (only when keeping terms up to x^3). To find the real part of a_1 as required in Equation 1.2, substitute $m = (n_R + in_I)/n_m$ into Equation 1.6:

$$a_1 = -i \frac{2x^3}{3} \frac{n_R^2 - n_I^2 + i2n_R n_I - n_m^2}{n_R^2 - n_I^2 + i2n_R n_I + n_m^2} \quad (1.8)$$

Next, switch to the complex metal dielectric function $\tilde{\epsilon} = \epsilon_1 + i\epsilon_2$ with the following relations:

$$\epsilon_1 = n_R^2 - n_I^2 \quad (1.9)$$

$$\epsilon_2 = 2n_R n_I \quad (1.10)$$

and switch to the medium's permittivity function: $\epsilon_m = n_m^2$. The substitution leads to:

$$a_1 = \frac{2x^3}{3} \frac{-i\epsilon_1^2 - i\epsilon_1 \epsilon_m + 3\epsilon_2 \epsilon_m - i\epsilon_2^2 + i2\epsilon_m^2}{(\epsilon_1 + 2\epsilon_m)^2 + (\epsilon_2)^2} \quad (1.11)$$

Substitution of a_1 in Equation 1.11 to Equation 1.1 and 1.2 yields the widely quoted expression for nanoparticle plasmon resonance:

$$\sigma_{ext} = \frac{18\pi\epsilon_m^{3/2}V}{\lambda} \frac{\epsilon_2(\lambda)}{[\epsilon_1(\lambda) + 2\epsilon_m]^2 + \epsilon_2(\lambda)^2} \quad (1.12)$$

$$\sigma_{sca} = \frac{32\pi^4\epsilon_m^2V^2}{\lambda} \frac{(\epsilon_1 - \epsilon_m)^2 - \epsilon_2^2}{(\epsilon_1 + 2\epsilon_m)^2 + \epsilon_2^2} \quad (1.13)$$

where V is the particle volume. Although the above approximations are only appropriate to small nanoparticles (less than 10 nm in diameter), these predictions of dielectric sensitivity remain suitable and accurate for larger particles.^[28]

In Equation 1.12, the extinction cross-section would be maximized when the condition of $\epsilon_1 = -2\epsilon_m$ can be made. This reveals that the LSPR extinction peak

is dependent on the surrounding dielectric medium. In addition, the LSPR sensitivity originates from the real part of the dielectric function at the wavelength.^[29] And the imaginary part of the dielectric function plays the important role on plasmon damping, that is the resonance peak broadening observed in experiment. In general, silver suffers lower energy loss than gold, however, gold is more often chosen for plasmon related experiments, such as biosensing, nanolaser and metal enhanced fluorescence, since it is easier to be surface modified, less prone to react with oxygen and shows low toxicity for biosensing and imaging.^[30–32]

1.1.2. Gans Theory

Although some predictions of Mie's theory remain suitable and accurate for particles larger than 10 nm, it is strictly applicable to spherical particles. In 1912, Richard Gans extended Mie's results to spheroidal particles of any aspect ratio in the small particle approximation.^[1,13,19] He proved that the absorption cross-section of a prolate spheroid was similar to the Equation 1.12 of:

$$\sigma_{abs} = \frac{\omega}{3c} \varepsilon_m^{3/2} V \sum_j \frac{(1/P_j^2)\varepsilon_2}{\{\varepsilon_1 + [(1-P_j)/P_j]\varepsilon_m\}^2 + \varepsilon_2^2} \quad (1.14)$$

Here, the sum over j considers the three dimensions of the particle. P_j includes P_A , P_B and P_C , which are the depolarization factors of each axis of the particle ($A > B = C$ for a prolate spheroid), and they could be expressed as follows:

$$P_A = \frac{1-e^2}{e^2} \left[\frac{1}{2e} \ln \left(\frac{1+e}{1-e} \right) - 1 \right] \quad (1.15)$$

$$P_B = P_C = \frac{1-P_A}{2} \quad (1.16)$$

where e is the factor in Equation 1.17 including the particle aspect ratio R .

$$e = [1 - (\frac{B}{A})^2]^{1/2} = (1 - \frac{2}{R^2})^{1/2} \quad (1.17)$$

The extinction spectrum for a prolate spheroid should have two peaks based on the Equation 1.14. One is corresponding to the transverse plasmon mode from the x and y contributions to the sum and the other is corresponding to the longitudinal plasmon mode from the z contribution. The scheme of transverse and longitudinal plasmon modes are shown in Figure 1.2. Meanwhile, the Equation 1.14 also provides a simple and direct understanding of the geometric effect on the LSPR peak wavelength. The factor weighting ϵ_m is 2 for spherical particles and $(1 - P_j)/P_j$ for prolate spheroids. As the increase of aspect ratio, the $(1 - P_j)/P_j$ could be much larger than 2 and this would lead to a redshift of the plasmon peak as well as the increased sensitivity to the dielectric environment.^[1,10]

1.1.3. Photoluminescence of Gold nanoparticles

In recent studies, the photoluminescence from gold nanoparticles has proven to be a promising property for the applications of imaging and sensing.^[6,33–35] Although the luminescence quantum yield (QY) of gold nanoparticles is much lower than that of fluorescent molecules or quantum dots, their large absorption cross section compensates for their low QY and makes them high-contrast imaging agents. The first observation of photoluminescence of gold dates back to

1969, when Mooradian observed a broad luminescence spectrum with a QY of about 10^{-10} from bulk gold.^[36] Photoluminescence from bulk gold originates from radiative transitions of conduction electrons toward empty electron states, which can be either holes in the *d*-band (electron-hole inter-band transitions), or empty electron states or holes within the *sp*-band (intra-band transitions).^[34] Later, the surface roughness enhanced photoluminescence of gold was studied, and the enhancement was attributed to the presence of localized surface plasmons.^[33] Since the observation of plasmon-enhanced emission, the effect of localized surface plasmons has been investigated in colloidal nanoparticles with different sizes and shapes.^[37] Figure 1.3 shows the production of hot electron and hot hole pairs *via* inter-band and intra-band relaxations led by plasmonic oscillation decay, respectively. In general, the observed photoluminescence enhancement can be simply explained by the plasmon-enhanced local fields. The reported luminescence QY are from 10^{-7} to 10^{-4} for gold nanoparticles with different sizes and shapes.^[12] In particular, Dulkeith et al. proposed a process in which *d*-band holes could also recombine non-radiatively with *sp* electrons instead of the radiative recombination of e-h pairs.^[38] In this process, each excited *d*-band hole polarizes the particle and triggers a collective electron oscillation (surface plasmon). These plasmons decay either radiatively by emitting photons or non-radiatively *via* transformation into excited e-h pairs.

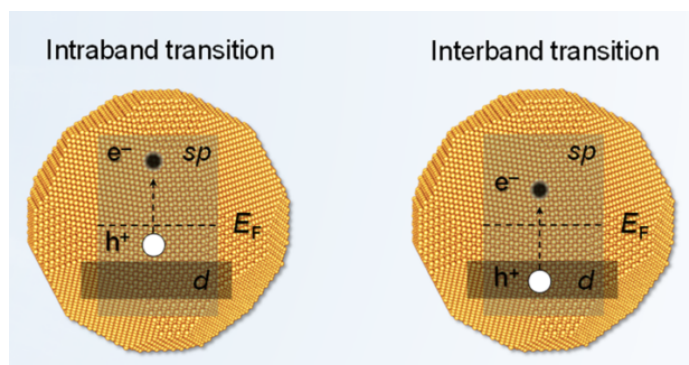


Figure 1.3 Decay of the plasmonic oscillation leads to the production of hot electron and hot hole pairs *via* inter-band and intra-band relaxations, respectively.^[12]

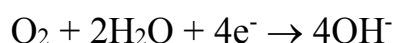
1.2.Principle of Electrochemical Oxygen Catalysis

1.2.1. Electrochemical Oxygen Catalysis

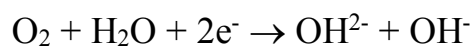
Energy and environment are of great concerns in current age. The demand for clean energy has been growing rapidly.^[39] Therefore, energy conversion from renewable sources has been a promising solution to reduce the dependency of conventional fossil fuel. In particular, electrochemical water splitting and metal air batteries are the simplest and most efficient classifications. Oxygen evolution reaction (OER) is the core reaction for the aforementioned reversible systems along with oxygen reduction reaction (ORR) and hydrogen evaluation reaction (HER).^[40–42] Typically, ORR process in a zinc-air battery contains a few steps: oxygen diffusion through the porous electrode, oxygen absorption to catalyst surface, electrons movement from the anode to the oxygen molecules, weakening and breaking of the oxygen-oxygen bond and the hydroxyl ion transfer through

electrolyte to metallic anode.^[43,44] Though the mechanism of ORR involves a series of complicated reactions, it is believed that a direct four-electron pathway or a peroxide two-electron pathway may proceed for the oxygen reduction depending on adsorption type.^[45] Even for the same catalyst, the ORR behaviours may be different depending on its structure. In a four-electron pathway, the oxygen directly reduced to OH⁻ under bidentate O₂ adsorption, where two O atoms coordinate with the catalyst. On the contrary, oxygen indirectly reduced to OH⁻ *via* HO₂⁻ in a two-electron pathway under end-on O₂ adsorption where one O atom coordinates perpendicularly to the catalyst. Then, this two-electron oxygen reduction may be followed by either a two-electron reduction of peroxide or the chemical disproportionation of peroxide. The four-electron pathway is preferable, because the two-electron pathway forms corrosive peroxide species and shows low energy efficiency.^[46,47] It is widely believed that the four-electron reduction predominates on noble metal catalysts, whereas the two-electron reduction primarily participates on carbonaceous materials. For other materials such as transition metal oxides, different ORR pathways may occur due to their specific crystal structure and molecular composition. The aforementioned reactions are given as follows:

Four-electron pathway:

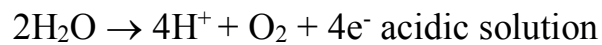
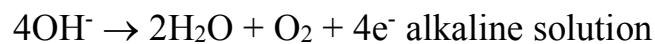


Two-electron pathway:

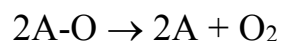
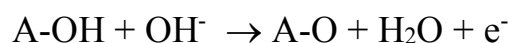
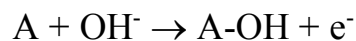




Oxygen evolution reaction plays a key part on electrically rechargeable metal air batteries and water splitting.^[48-50] As the reverse reaction of ORR, OER is also a complex process involving several reactions. As oxygen is generally evolved from an oxide phase, the mechanism largely depends on the electrode materials and the site geometry of the metal cation.^[39,51,52] In addition, the reaction is highly pH dependent. In acidic and neutral environments, two H₂O molecules are oxidized into four H⁺ ions and one O₂ molecule; whereas in basic conditions, OH⁻ ions are oxidized and transformed into H₂O and O₂ molecules, as shown as follows:



Since the current research of OER focuses on the transition metal oxides materials, it is necessary to detailed introduce the OER mechanism in alkaline conditions, as transition metal oxides are not stable at acidic environment. One of the highly recognized mechanism is the electrochemical oxide pathway:



The major difference of OER in alkali is the first-step absorption of hydroxide ion other than absorption of water on the surface of active site (A) in acid.^[53] Importantly, the active site S undergoes a cycle of oxidation and reduction during OER to evolve oxygen and regenerate the surface active sites for the next cycle. This means that only metals with variable oxidation states (chemical states) could be the catalysts for efficient OER catalysis.^[54,55] For the iron group (mainly Fe, Co and Ni), they undergo oxidation from the positive divalent to the positive trivalent state while coordinating with a hydroxide ion in alkaline environment, which leads to the formation of key intermediate, MOOH. Then, the intermediate, MOOH, undergo deprotonation-coupled reduction of the active site with the evolution of oxygen.^[56,57] The common reaction sequences of OER with the oxides/hydroxides of iron group metals are given below:



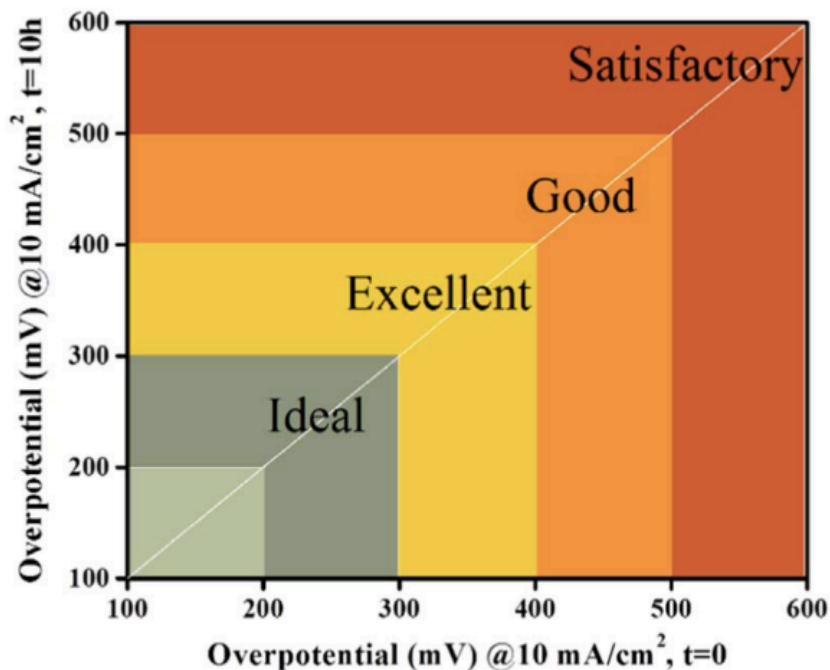


Figure 1.4 The figure of merit for OER. Notably, this protocol is applicable to a full pH range, which is more suitable for real device fabrication. To compare different catalysts, one should keep in mind the nature of electrode, mass loading and pH.^[39]

It is believed that the transition metal ions in materials undergo progressive oxidation to higher valence states or electron confinement prior to the OER, during the electrochemical process.^[52,58-60] This indicates that the highly oxidative metal ions may be the active sites of OER catalysts. And the corresponding investigations confirm that the OER catalytic performance may depend on the outer electron states of the transition metal species.^[61-63] During the LSPR process, hot electrons will be excited and transferred, and simultaneously leading to the hole generation on the surface of plasmonic materials to capture external electrons.^[13] Inspired by the above phenomena,

hybridizing the transition metal catalyst with plasmonic metal nanoparticles would cause electron-confined transition metal species, and eventually promote the OER catalytic performance. In addition, transition metals, such as Mn, have multiple chemical states and are easy to form 2D nanostructures. Thus, the investigation of transition metal species of Mn with plasmonic nanoparticle is highly necessary.

1.2.2. Electrochemical Measurements

In general, the electrochemical measurements deal with response of working electrode in the electrolyte under the influence of applied potentials. For the work in this project, we are interested in the response of the working electrode in a potential range, where the oxygen evolution reaction occurs. The conventional three-electrode system were used, including a working electrode, a counter electrode and a reference electrode. The working electrode contains the catalyst (sample). To discuss the electrochemical measurements, the first thing needed to know is the reversible hydrogen electrode (RHE). As a reference electrode, it is more likely a subtype of the standard hydrogen electrode for electrochemical processes. The standard hydrogen electrode (SHE) is a redox electrode which forms the basis of the thermodynamic scale of oxidation-reduction potentials. The absolute electrode potential forms a basis for comparison with all other electrode reactions, and hydrogen's standard electrode potential is declared to be zero volts at all temperatures.^[64] Unlike the SHE, RHE measured potential does not change

with the pH, so it can be directly used in the electrolyte. The name refers to the fact that the electrode is in the actual electrolyte solution and not separated by a salt bridge. Therefore, the hydrogen ion concentration corresponds to that of the electrolyte solution. In this way, a stable potential can be achieved.^[65,66] Thus, all the experiments performed by other reference electrodes, such as Hg/HgO, need to be converted to reversible hydrogen electrode for easy comparison. According to the Nernst equation scale:

$$E_{\text{RHE}} = E_{\text{Hg/HgO}} + 0.059 \times \text{pH} + 0.098 \quad (1.18)$$

the overpotential (η) of OER at $j = 10 \text{ mA/cm}^2$ was determined using the following equation:

$$\eta = E_{\text{RHE}} - 1.23 \text{ V} \quad (1.19)$$

where $E_{\text{Hg/HgO}}$ is the measured potential in experimental system on Hg/HgO reference electrode and E_{RHE} is the standardized potential.^[67]

The most significant factor for evaluating the performance of OER catalysts is the onset potentials, however, it is difficult to observe the exact value. Therefore, the value of potential at 10 mA/cm^2 is more reliable and commonly used. Overpotential is the potential difference between the potentials achieving a specific current density (commonly used, 10 mA/cm^2) and 1.23 V . Generally, a catalyst that has overpotential below 0.4 V is considered to be an excellent catalyst for OER (as shown in Figure 1.4); however, there is few catalysts that have overpotentials less than 250 mV .

Tafel slope is another significant factor to evaluate the performance of OER catalysis. The Tafel equation in electrochemical kinetics relates the rate of an electrochemical reaction to the overpotential, which is named after Swiss chemist Julius Tafel. Tafel analysis is usually employed to understand the reaction kinetics and mechanism and to compare the catalytic activity of different catalysts. The Tafel slope also helps to define the rate determining step by examining the sensitivity of the current response to the given voltage by Equation 1.20:

$$\eta = b \log(j/j_0) \quad (1.20)$$

where η denotes the overpotential, b represents the Tafel slope, j is the current density and j_0 is the exchange current density. The quality of good OER catalysts should have a lower Tafel slope and larger current density.^[39,52] In particular, the exchange current density is the current in the absence of net electrolysis at zero overpotential (at 1.23 V vs RHE). It can be understood as a background current density by which the net current observed at various potentials can be normalized.^[66,68]

In order to facilitate comparison between samples and experimental setups, it is necessary to identify the Ohmic loss for each experiment. Ohmic losses may come from resistance in connections, interfaces, samples and the electrolyte. In fact, the ionic conductivity of the electrolyte is a dominant factor and it is quite necessary to keep a fixed distance between electrodes for a series of experiments. The magnitude of the Ohmic loss can be evaluated by impedance spectroscopy,

where the impedance is measured as a function of current frequency. A simple equivalent circuit model of an electrochemical interface includes a resistor and a constant phase element (CPE) in parallel. The capacitance contribution to the impedance vanishes at high frequencies, then the resistance can be revealed as the real component of the impedance.^[69]

Zeta-potential is a scientific term for electro-kinetic potential in colloidal dispersions, which is always denoted as ζ -potential by using the Greek letter zeta (ζ). It is the potential difference between the dispersion medium and the stationary layer of fluid (such as surfactant and polyelectrolyte) attached to the dispersed particle. As shown in Figure 1.5, Zeta-potential is caused by the net electrical charge difference within the region between Stern layer and the slipping plane, and it also depends on the location of the slipping plane.^[70] Thus, it is widely used to quantify the surface charge and stability of nanoparticles. Notably, Zeta-potential is not equal to the Stern potential or electric surface potential in the double layer, since their location definitions are very different. Commonly, differential light scattering technique is used for Zeta-potential measurement, and electrophoretic mobility is the key experimentally-revealed parameter for the indirect Zeta-potential measurement.^[71] Zeta-potential is a key indicator of colloidal stability. The magnitude of the Zeta-potential indicates the degree of electrostatic in a dispersion. For nanostructures, a high Zeta-potential will confer stability and resist aggregation. When the potential is small, attractive force may exceed this repulsion and the dispersion may break and flocculate. Therefore,

high positive or negative Zeta-potential over 30 mV would lead to monodispersity, and low values (smaller than 5 mV) could lead to agglomeration.^[72,73]

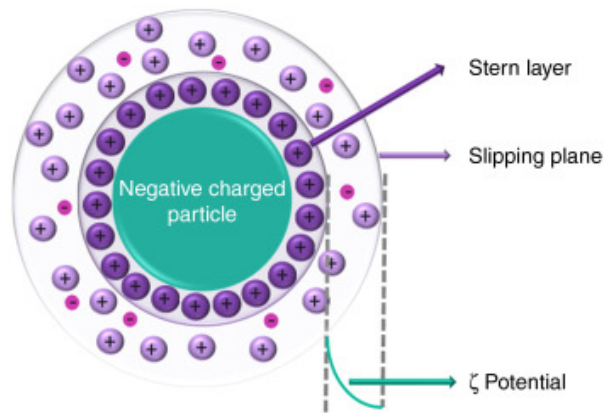


Figure 1.5 Schematic diagram of Zeta-potential.^[70]

2. Fluorescence

2.1. General Principle of Fluorescence

The physical process of light emission involves both luminescence and incandescence. As a special case of thermal radiation, incandescence is the emission of light (electromagnetic radiation) from a hot matter as a result of the temperature.^[74] The physical mechanism of luminescence can be described as the emission of light from electronically excited states of any substances and could formally be divided into two categories: fluorescence and phosphorescence.^[75,76] Generally, absorption occurs in about 10^{-15} s. For the fluorescence process, an electron is usually excited to a higher S_1 or S_2 electronic level which has the opposite spin state to the second electron in the ground state. For some special cases, molecules in condensed phases rapidly relax to the lowest vibrational level of S_1 , which is called internal conversion and generally occurs less than 10^{-12} s. Consequently, the excited electron (spin allowed) rapidly returns to the ground state (S_0) by releasing a photon. Typically, the emission rates of fluorescence are around 10^8 s⁻¹; thus, the fluorescence lifetime is near 10 ns, where the lifetime of a fluorophore is the average decay time from the excited state (S_1) to the ground state (S_0).^[77,78] The notation of S_0 , S_1 and S_2 refers to the singlet ground, first and second states. On the other hand, in the case of phosphorescence the excited electron undergoes intersystem crossing from the S_1 state to the excited triplet state (T_1). Since the same spin state in the orbital, the direct transition to the

ground state is not allowed. Therefore, the emission rate of phosphorescence is much lower and the lifetime is in the millisecond to second range.^[79,80] Intersystem crossing is more likely to take place when the vibrational levels of the singlet and triplet state overlap, since only a small amount of energy is lost in the transition.^[80] A Jablonski diagram can be utilised to show the physical processes involved in luminescence, as shown in Figure 2.1.

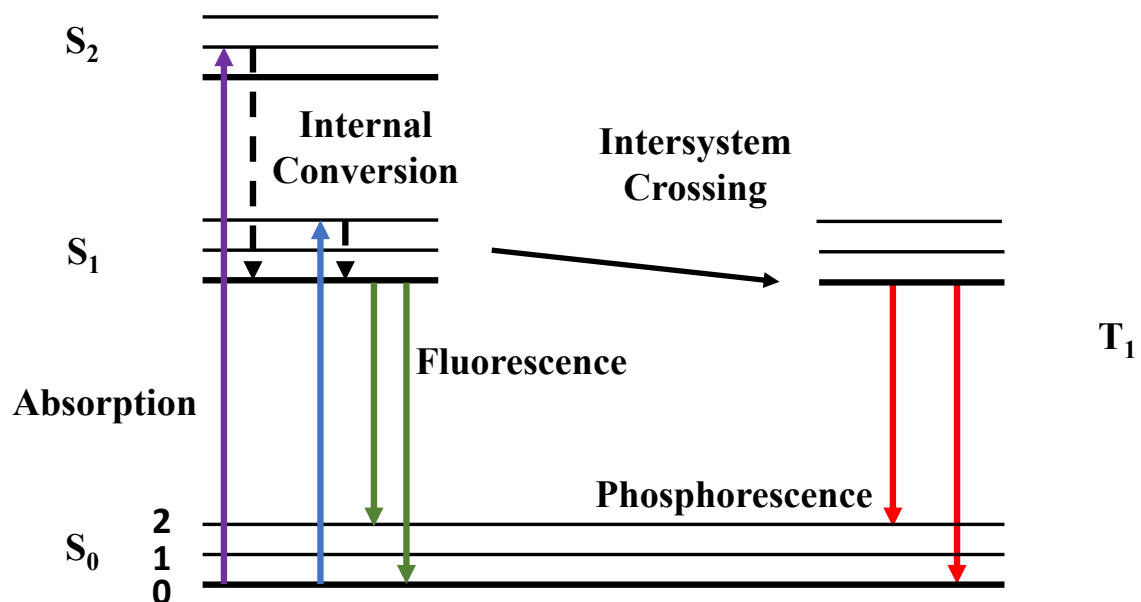


Figure 2.1 Jablonski diagram of physical processes that take place during fluorescence and phosphorescence.^[75]

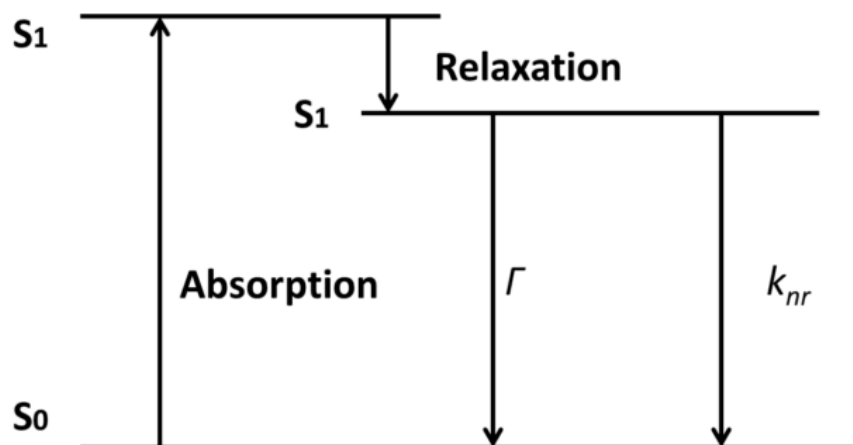


Figure 2.2 Simplified diagram of the physical process of fluorescence decay.

As shown in Figure 2.2, the excited electron of a fluorophore can return to the ground state through either a radiative decay (emission of a photon) or non-radiative process. The fluorescence quantum yield is the ratio of the number of photons emitted to the number absorbed, which can be defined as:

$$Q = \Gamma / (\Gamma + k_{nr}) \quad (2.1)$$

where Q , Γ and k_{nr} represent the quantum yield, the radiative decay rate and the non-radiative decay rate, respectively. Since the existence of Stokes loss (Stokes shift), the quantum yield is always less than the unity. The Jablonski diagram, Figure 2.1, shows that the energy of emission is less than that of absorption and fluorescence always occurs at longer wavelength. After first observation by Sir G. G. Stokes at University of Cambridge in 1952, this phenomenon is named as Stokes shift.^[74,75,80] Figure 2.3 shows the absorption and emission spectra of Mega

520 dye which has a large Stokes shift of around 150 nm. Indeed, energy loss between excitation and emission is widely observed for fluorophore molecules in

solution. The common cause of the Stokes shift is the rapid decay to the lowest vibration level of S_1 as well as the decay to the higher vibrational levels of S_0 , which result the loss of excitation energy to heat of the vibrational energy. In addition, solvent effects, complex formation and energy transfer may also lead to further Stokes shift.

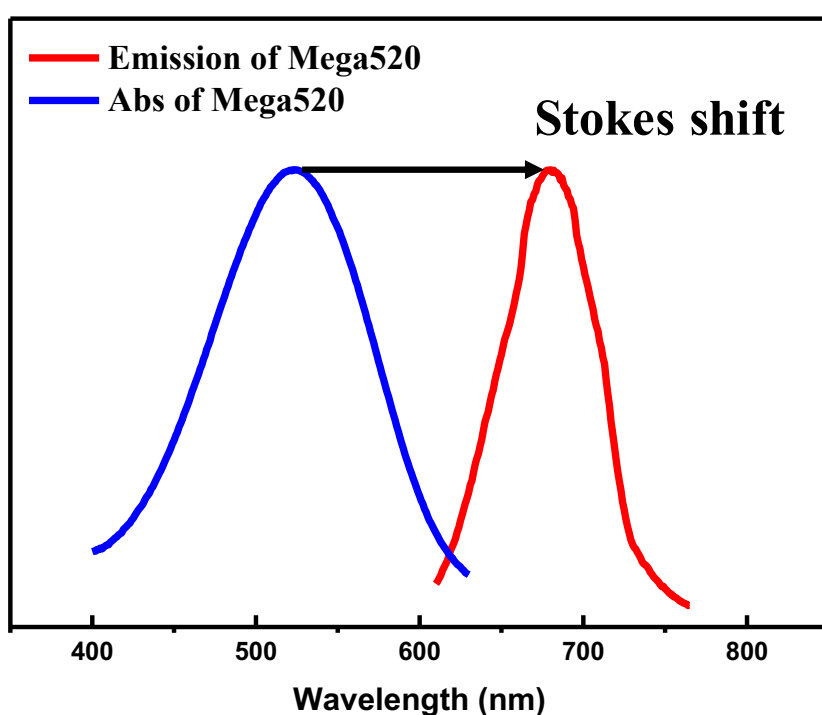


Figure 2.3 Absorption and emission spectra of Mega 520, which show a large Stokes shift of around 150 nm.

The easiest way to estimate the quantum yield of a fluorophore is to compare with standards which have known quantum yield. Some of the most used standards are quinine sulfate, fluorescein, rhodamine 6G and rhodamine 101. The quantum yields of standards are mostly independent of excitation wavelength, so

that they can be used wherever they show useful absorption. Determination of the quantum yield is generally accomplished by comparison of the absorption and emission of the unknown to that of the standard. The optical densities of the sample and reference (r) either need to be kept below 0.05 to avoid inner filter effects (self-quenching effects), or should be matched at the excitation wavelength.^[75] The quantum yield of the unknown sample is calculated using:

$$Q = Q_R \frac{I}{I_R} \frac{OD_R}{OD} \frac{n^2}{n_R^2} \quad (2.2)$$

where Q and Q_R are the quantum yields, I and I_R are the integrated emission peak areas, OD and OD_R are the absorbance and n and n_R are the solution refractive index of the sample and reference, respectively. In this expression it is assumed that the sample and reference are excited at the same wavelength, so that it is not necessary to correct for the different excitation intensities of different wavelengths.^[75,81,82]

Another main distinguishing characteristic of fluorescence is the time spends in the excited states, which is also known as the fluorescence lifetime. As described before, the lifetime of a fluorophore molecule is the average time the electron stayed in the excited orbital before returning to the ground state, and can be expressed as:

$$\tau = 1/(\Gamma + k_{nr}) . \quad (2.3)$$

Importantly, the fluorescence emission is a random process and few molecules emit their photon at $t = \tau$. The fluorescence lifetime is an average value of the time spent in the excited state.^[75]

2.2. Fluorescence Quenching and Energy Transfer Models

Fluorescence quenching is the decrease of fluorescence emission intensity of a fluorophore by a wide variety of physical and chemical processes.^[74,83,84] It can occur under different mechanisms. As the most common one, collisional quenching occurs when the excited fluorophore is deactivated upon contact with other molecule (quencher) in solution leading to the excited electron to relax to the ground state without emitting, which is illustrated on the Jablonski diagram in Figure 2.4. The energy is released as heat and dispersed into the surrounding environment. This collision between the fluorophore and quencher will cause no chemical alteration of the fluorophore. Thus, collisional quenching can be used as a probe to locate the fluorophores within proteins and macromolecules.^[85] Due to the nature of collisional quenching, temperature and pressure of the environment are the key factors linking to the process, which would affect the diffusive property of the quencher. Meanwhile, the fluorophores with longer fluorescence lifetime are more likely to experience a collisional quenching. The decrease in fluorescence intensity is described by the Stern-Volmer equation, as follow:

$$\frac{I_0}{I} = 1 + K[Q] = 1 + k_q\tau_0[Q] \quad (2.4)$$

where K is the Stern-Volmer quenching constant; k_q is the bimolecular quenching constant; τ_0 is the unquenched lifetime; $[Q]$ is the quencher concentration; and I_0 and I are the unquenched and quenched fluorescence intensity, respectively. The Stern-Volmer quenching constant K indicates the sensitivity of the fluorophore to a quencher. For instance, a fluorophore buried in a macromolecule is usually difficult to access to soluble quenchers, so that the K is small.^[85] Larger value of K is found if the fluorophore is free in solution or on the surface of a biomolecule. Common collisional quenchers found are oxygen, metallic ions and electron-deficient molecules such as acrylamide, which are all water soluble.^[75,83,85–87] Except for collisional quenching, the static quenching can occur by forming non-fluorescent complexes with quenchers, which does not rely on diffusion. In addition, quenching may also occur under non-molecular mechanisms, such as attenuation of the incident light by other absorbing species.

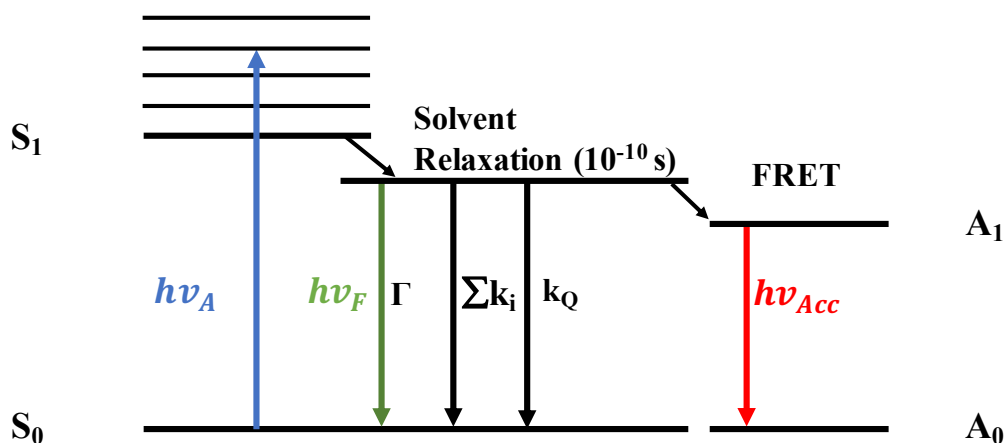


Figure 2.4 Diagram with collisional quenching and Förster resonance energy transfer (FRET). The term $\sum k_i$ represents all non-radiative decays to the ground state aside from quenching and FRET.

Förster resonance energy transfer (FRET) is an important process which occurs whenever the emission spectrum of a fluorophore (donor) overlaps with the absorption spectrum of another molecule (acceptor).^[88,89] In general, FRET takes place over a donor-acceptor distance between 2 nm and 10 nm. The donor and acceptor are coupled through a dipole-dipole interaction without intermediate photon, which results in the excited molecule being quenched and causes the acceptor fluorophore to fluoresce, as shown in Figure 2.4.^[90] The extent of energy transfer process is determined by the factors of spectral overlap and distance between donor and acceptor. The rate of energy transfer is shown in Equation 2.5:

$$k_{\tau}(r) = \frac{1}{\tau_D} \left(\frac{R_0}{r}\right)^6 \quad (2.5)$$

where r is the distance between donor and acceptor and τ_D is the original lifetime of the donor. And the spectral overlap is described in terms of Förster distance (R_0), as shown in Equation 2.6.^[91]

$$R_0 = 0.211 (Q_D n^{-4} k^2 J)^{1/6} \quad (2.6)$$

where Q_D is the quantum yield of the donor fluorophore, n is the refraction index of the environment, k is the orientation between donor and acceptor dipoles and J is the spectral overlap integral between donor (emission) and acceptor (absorption) spectra. Since the Förster distance is comparable in size to biomacromolecules, FRET has been used as a “spectroscopic ruler” for measurements of distance between sites on proteins.^[75,92,93]

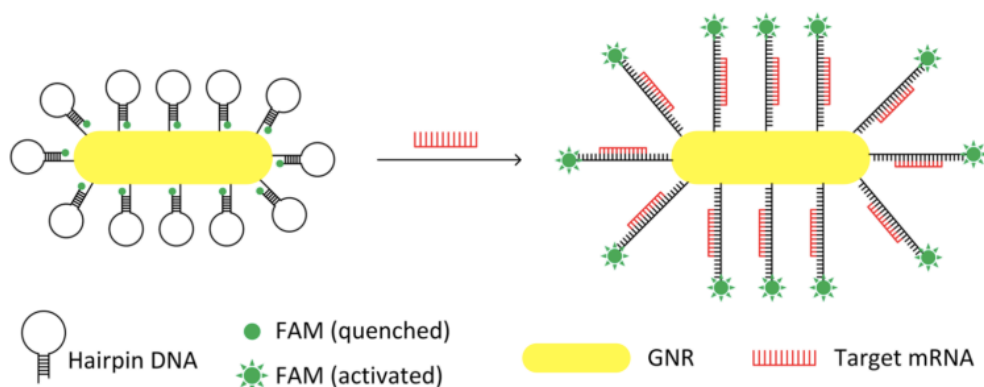


Figure 2.5 Schematic illustration of FAM attached hairpin DNA-functionalized gold nanorod for mRNA detection.^[94]

Another method of utilizing FRET involves the hybridization of hairpin DNA models to GNRs to sense mRNA, as shown in Figure 2.5. When the FAM (carboxyfluorescein) attached hairpin DNA was bound to the GNRs, the

fluorescence from donor FAM were largely quenched for the shorter donor-acceptor separation length. Upon interacting with target mRNA, the hairpin unfolds leading to the much larger separation of FRET pairs, where the fluorescence from FAM would be largely recovered.^[94,95] However, FRET is only efficient for separation distances up to 10 nm, which limits this optical-based distance measurements on tracking biomolecular conformational changes, drug discovery, and cell biology. Thus, the model of surface energy transfer (SET) was proposed by Professor Strouse at Florida State University, which described the interaction of a dipole (fluorophore) and a surface (noble metal nanoparticles).^[92,96,97] This SET model is the extension of the seminal work on oscillators interacting with bulk metal or thin film.^[98,99] This process is of great interest due to its long-range interaction, more than double the range of Förster resonance energy transfer (up to 22 nm).^[100] The interaction of the emitting fluorophore with the metal are strongly dependent on the separation distance between donor and the metal nanoparticle acceptor, the frequency of the oscillator and the extent of the coupling.^[88,99] The SET rate of k_{SET} and SET distance of d_0 are given in Equation 2.5 and 2.6, respectively:

$$k_{SET} = 0.225 \frac{c^3}{\omega_{dye}^2 \omega_F k_F d^4} \frac{Q_{dye}}{\tau_{dye}} \quad (2.6)$$

$$d_0 = \left(0.225 \frac{c^3 Q_{dye}}{\omega_{dye}^2 \omega_F k_F} \right)^{1/4} \quad (2.7)$$

where c is the speed of light, Q_{dye} is the quantum yield of the donor, ω_{dye} is the angular frequency for the donor, ω_F is the angular frequency for metal, k_F is the Fermi wavevector for metal, τ_{dye} is the original lifetime of the fluorophore and d is the distance between fluorophore and metal surface. In particular, d_0 is the convenient distance value for calculation, where a fluorophore would display equal likeness for energy transfer and spontaneous emission.^[24,101] Notably, both FRET and SET models does not include the effect of localized surface plasmon resonance from the noble metal nanoparticle. Previous studies show that FRET from donor to acceptor molecules can be enhanced within the presence of noble metal nanoparticles (surface plasmon resonance).^[102–105] In particular, Zhang and co-workers found that neither FRET nor SET model could explain the difference between the energy transfer efficiency of DAPI (4'-6-Diamidino-2-phenylindole) donor and gold nanosphere/gold nanorod acceptor. When the incident light wavelength overlaps with the L mode surface plasmon of GNRs, the enhanced local field caused by the surface plasmon resonance would lead to a stronger surface energy transfer effect.^[98] Other than the dipole-dipole interaction of FRET, the LSPR modes from noble metal nanoparticles represent the collective oscillation of many strongly coupled electrons. Therefore, the coupling of the oscillator in energy transfer is best described as an interaction between a fluorophore and 3D arrays of dipoles.^[99,101]

2.3. Plasmon Enhanced Fluorescence Process

In the fluorescence emission process, the observation of fluorescence intensity can be described by Equation 2.8:

$$I = \gamma_{ex} \cdot Q \cdot f_{eq} \quad (2.8)$$

where γ_{ex} is the excitation rate of the fluorophore, Q is the emission quantum yield of the fluorophore and f_{eq} is the light collection efficiency of the measurement system.^[80,84,106] Since the light collection efficiency is a constant which is system-dependant, studies that focus on γ_{ex} and Q need to be considered. The excitation rate is determined by Fermi's golden rule, as shown in Equation 2.9:

$$\gamma_{ex} = \left(4\pi^2/h\right) | \langle e | E \cdot p | g \rangle |^2 \rho_e \quad (2.9)$$

where h is the Plank's constant; E is the local field; p is the absorption transition dipole momentum; ρ_e is the density of the excited state; and e and g are the wave functions of the excited and ground states, respectively. If a fluorophore is in the vicinity of a plasmonic nanoparticles, the modification of fluorescence emission intensity is usually realized in two ways. First of all, the excitation rate would arise as the result of the enhanced local electric field caused by the excitation of surface plasmon resonance.^[107] Secondly, the excited fluorophore would undergo non-radiative decay to excite the localized surface plasmon resonance of plasmonic nanostructures by energy transfer.^[7,108] The localized surface plasmon resonance could alter both radiative and non-radiative decay of the fluorophore.

Then, the localized surface plasmon resonance would either radiate or undergo non-radiative decay to heat energy.^[73,109] That is why quenching could also be observed instead of fluorescence enhancement as the excited fluorophores would relax rapidly through non-radiative energy transfer into the surface plasmon resonance.^[84,110,111] Of course, both quenching and enhancement are distance dependent and scientists have observed almost 100 % quenching to more than 1000-fold enhancement in fluorescence emission intensity.^[73,112–114]

The lifetime of plasmon is very short of about 10 fs, which suggests that the energy transfer is essentially one way from fluorophore to metal.^[115,116] With the existence of plasmons, as shown in Figure 2.6, the former of increased excitation rate ($E + E_m$) would result in enhanced brightness without changing the quantum yield. In addition, the latter is to increase the radiative decay by plasmon effects.^[117,118] In this case, if the non-radiative decay induced by plasmon (k_m) is negligible, which means that the separation between dye and plasmonic metal is larger than 10 nm, the quantum yield and lifetime of the fluorophore near the metal surface are given by:

$$Q_M = \frac{\Gamma + \Gamma_m}{\Gamma + \Gamma_m + k_{nr}} \quad (2.10)$$

$$\tau_M = \frac{1}{\Gamma + \Gamma_m + k_{nr}} \quad (2.11)$$

where Q_M , τ_M and Γ_m are the quantum yield, fluorescence lifetime and radiative decay rate due to the metal, respectively. As the value of Γ_m increased, the

quantum yield also increases while the lifetime decreases. The enhancement of the quantum yield for fluorophore molecules near metal surface could be explained as a result of rapid energy transfer to plasmons with a radiation to the far field.^[119–123] This rapid energy transfer from a donor to an acceptor would result in an increased overall quantum yield of the system, where the energy transfer is proportional to the radiative rate of the donor and independent of the non-radiative decay rate.^[112,113,124–126] This effect is larger for fluorophores with low quantum yield.^[119,127,128]

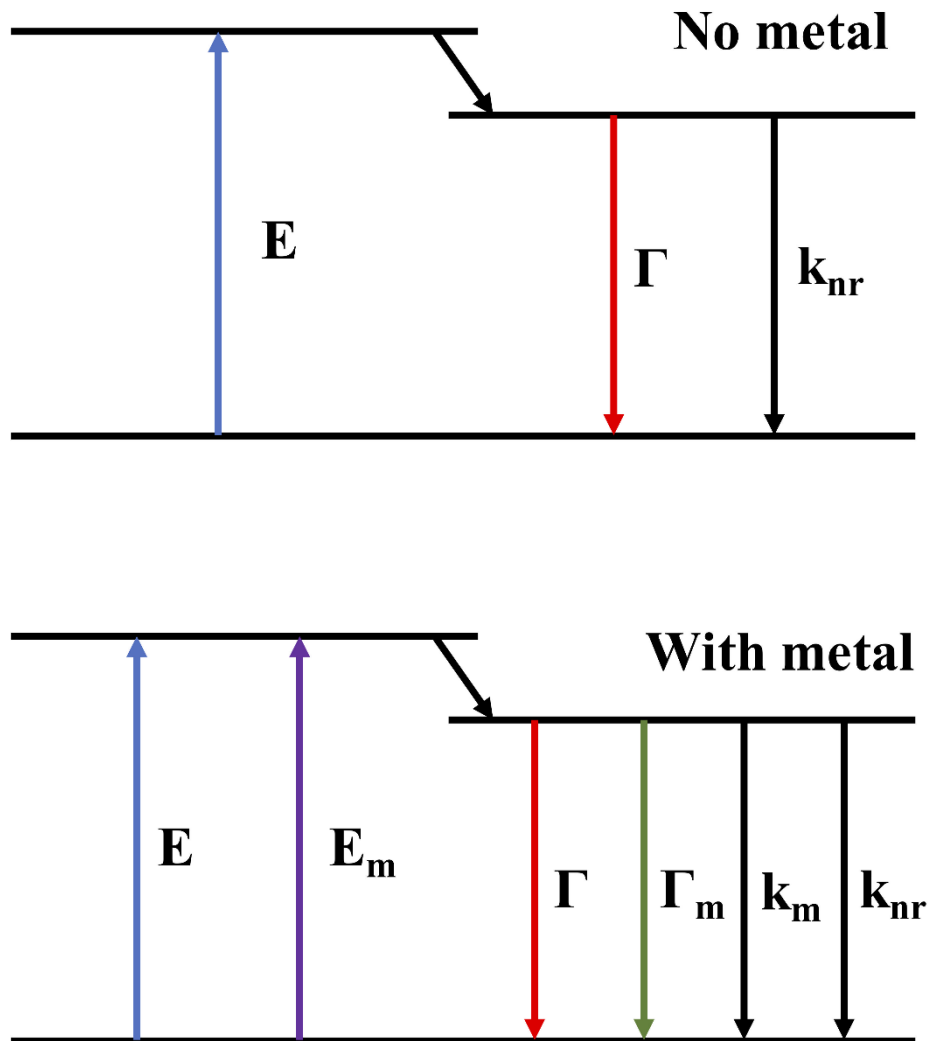


Figure 2.6 Simplified diagram of the fluorescence process with and without metal surface. The transition labels are defined in section 2.3.

2.4. Time-correlated Single Photon Counting (TCSPC)

Fluorescence lifetime spectroscopy measures the average time that fluorophores stay in the excited state. Currently, there are two methods to measure the fluorescence lifetime, frequency domain and time domain lifetime measurements.

Since the Time Correlated Single Photon Counting technique were used throughout this project, it is necessary to introduce this technique in detail. The principle of TCSPC is unique, which is based on the concept that the probability of detection of a single photon at time t is proportional to the fluorescence intensity at that given time. By accurately measuring the arrival time of every single photon, the decay waveform could be reconstructed. The sample is excited with a pulsed light source. The typical detection rate is 1 photon per 100 excitation pulses, which is critical to avoid bias on detecting shorter lifetimes. As shown in Figure 2.7, when a single emitting photon from the fluorophore is detected, the arrival time of the corresponding photon to the detector is measured, which adds '1' count in a memory located at an address proportional to the detection time. After many signal periods, many photons have been detected and the distribution of the photons over time in the signal period builds up. The results represent the 'waveform' of the optical pulse.

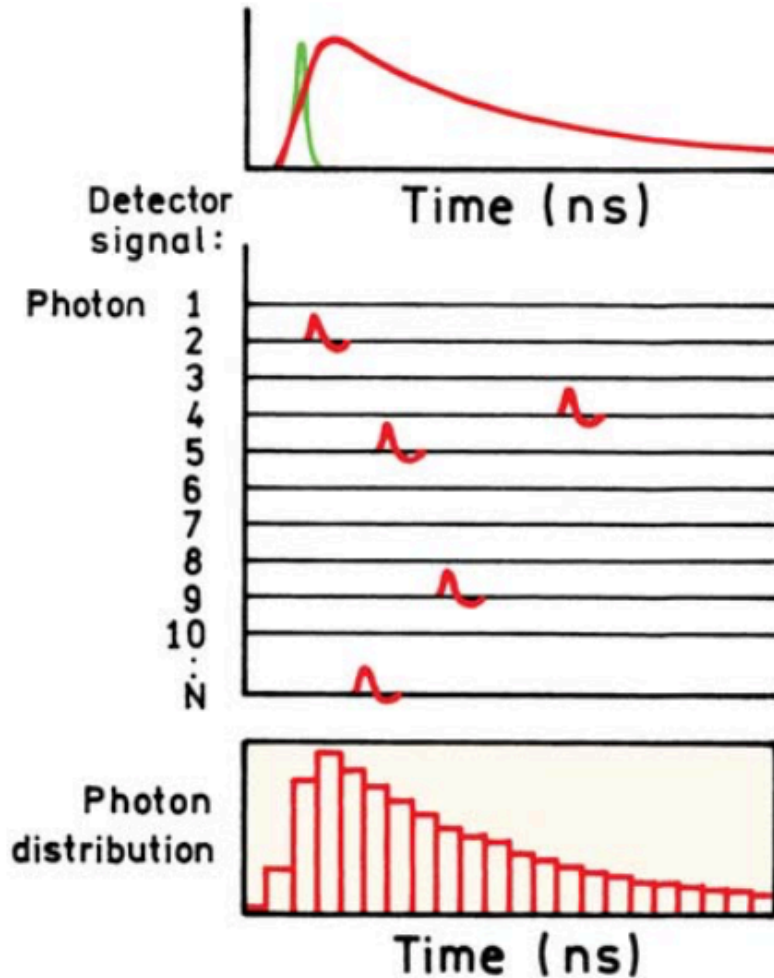


Figure 2.7 Schematic illustration of Time-correlated Single Photon Counting (TCSPC).^[129]

A classic TCSPC setup is shown in Figure 2.8. In a single measurement process, the experiment starts from the excitation of the samples and sends a signal to the electronics. This signal is passed through a constant function discriminator (CFD), which accurately measures the arrival time of the pulse. Then, the signal is passed to the time-to-amplitude converter (TAC) to form a voltage, which increases linearly with time on the nanosecond scale. The voltage now is proportional to the time delay between excitation and emission signals or

between start and stop pulses. Meanwhile, a second channel detects the pulse from the single detected photon. The arrival time of the signal is then accurately determined by a CFD and a signal is sent to stop the voltage. The voltage is amplified by a programmable gain amplifier (PGA) and the output of analog-to-digital converter (ADC) is used to convert the voltage to the numerical value.

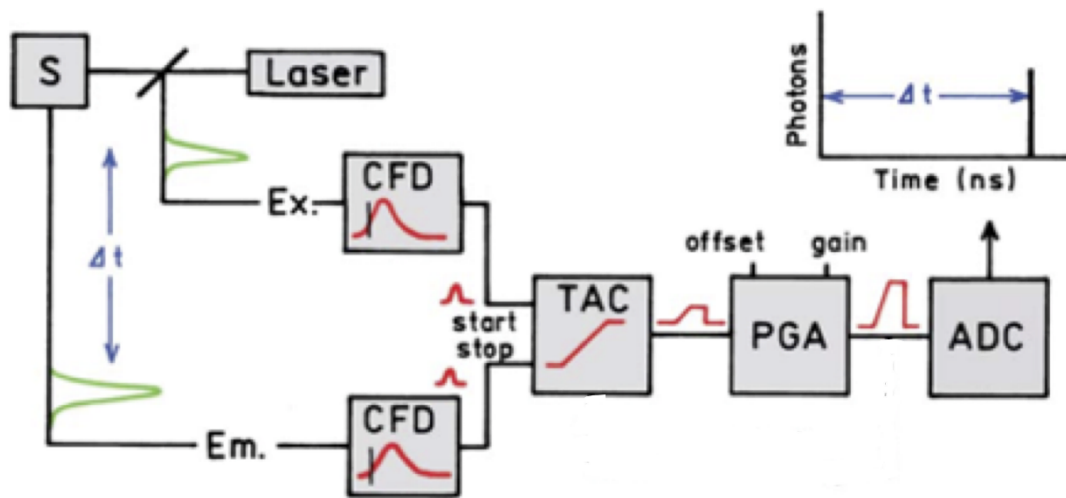


Figure 2.8 Electronic schematic for Time-correlated Single Photon Counting (TCSPC).^[129]

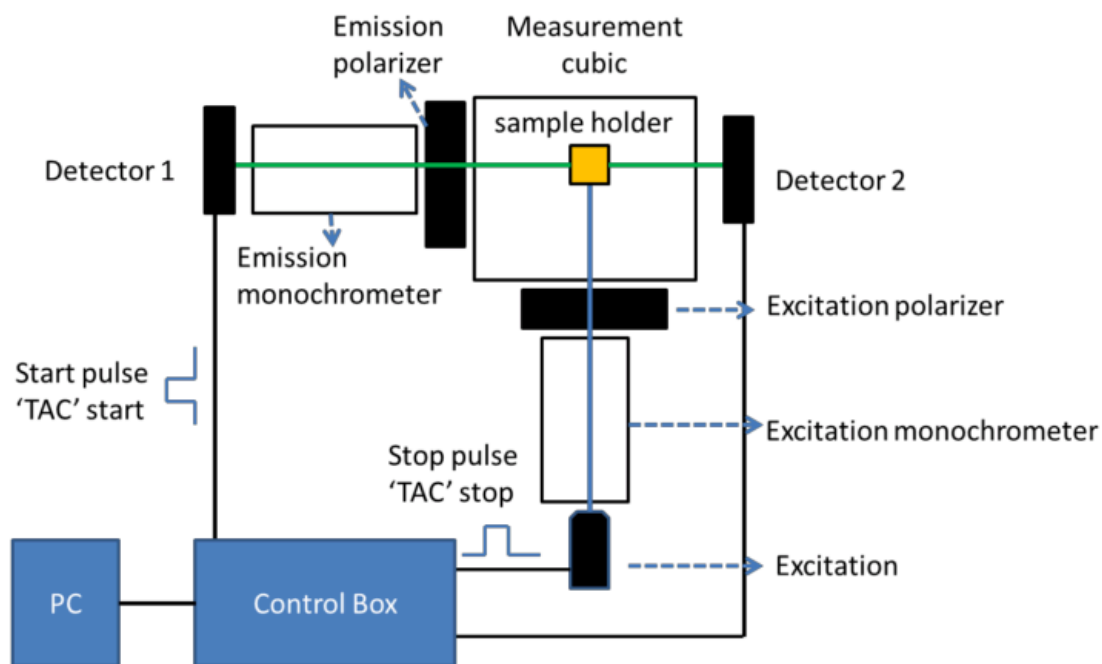


Figure 2.9 Schematic setup of Horiba Jobin Yvon IBH fluorescence lifetime measurement kit.^[79]

If the TAC range is selected in a time longer than the measured time, it can be beneficial to measure in the “reverse mode”. In practical, many experiments were performed through a ‘reverse mode’, where the pulse from the detector will be the start pulse while the pulse from light source is to stop the TAC. Due to the high repetition rate of modern pulsed-light sources, the TAC can be constantly in reset mode if the start signals arrive too rapidly. As the emission pulses are much less frequent than the excitation ones, a ‘reverse mode’ would be more efficient. “Reverse mode” switches the start and stop signals, which makes every measurement be for emission event rather than excitation and reduces the total data collecting time. Figure 2.5 shows the schematic setup of TCSPC kit from

Horiba Jobin Yvon IBH, which was used for all lifetime measurements in this thesis.^[74]

2.5. Data analysis of fluorescence lifetime measurement

To seek the accurate value for fluorescence lifetime, it is necessary to use correct mathematical model to fit the data. However, utilizing experimental data from TCSPC measurement is complex due to the complexity of the fluorescence characteristics. In this thesis, a one or multiple exponential model was used to analyze the fluorescence lifetime values, as shown in Equation 2.12:

$$I(t) = \sum_{i=1}^n b_i \exp\left(-\frac{t}{\tau_i}\right) \quad (2.12)$$

where $I(t)$ is the lifetime decay function as regards time, b_i is the fluorescence lifetime intensity, τ_i is the fluorescence lifetime and t is the time after excitation.

In the multi-exponential mode, the intensity is assumed to decay as the sum of individual single exponential decays. In order to test the quality of the fitting between theoretical function and the measured decay, non-linear least squares analysis is employed. The parameter, chi squared value (χ^2), shows if a fit is good.

The formula is shown in Equation 2.13:

$$\chi^2 = \sum_N \left[\frac{Y(i) - F_D(i)}{\sigma(i)} \right]^2 \quad (2.13)$$

where $Y(i)$ is the measured data, $F_D(i)$ is the fitting function, $\sigma(i)$ is the standard deviation of $Y(i)$ and N is the number of data channels selected for analysis.

Typical, a perfect fit should have a χ^2 value of 1.0. However, a value of $1.3 < \chi^2 < 0.9$ is widely accepted as a good fit.

In addition to exponential model, analysis using maximum entropy method (MEM) allows recovery of lifetime distributions without assumption shape functions, which makes the decay distribution be easily visualized. Though the commercial algorithms are not completely explained, it has now been widely utilized in complex decay analysis.^[110,130,131] The MEM is also mathematically complex, which is based on the Skilling-Jaynes entropy function as shown in Equation 2.14:

$$S = \int_0^{\infty} \alpha(\tau) - m(\tau) - \alpha(\tau) \log \frac{\alpha(\tau)}{m(\tau)} d\tau \quad (2.14)$$

where $\alpha(\tau)$ is the recovered distribution, $m(\tau)$ is an assumed mode that is in $\log \tau$ space. The MEM method is also used along with non-linear least square analysis to ensure that the analyzed result is consistent with experimental data. The MEM is very useful since it provides enough detail to reveal the shape of lifetime distribution.^[75]

2.6.SPASER Concept and Purcell Effect

SPASER is short for surface plasmon amplification by stimulated emission of radiation, which was first introduced by Stockman and Bergman in 2003.^[3,132,133] Thereafter, the possibility of fabricating a SPASER source has attracted considerable attentions during the past 15 years, because of its potential

applications from sensing and biomedicine to imaging and information technology.^{[134–136],[132]} The SPASER concept can be described as: the gain media near a noble metal core transfers energy to a resonant surface plasmon (SP) mode of the metal core.^[3,137–139] The SP stimulates further transitions in the gain medium, leading to the excitation of more identical SPs in the same SP mode, driving the action of the SPASER.^[137] The idea is to confine light in the form of localized surface plasmons overlapping with the gain medium to achieve stimulated emission and light amplification, and create a coherent light source at the nanoscale, eventually.^[140]

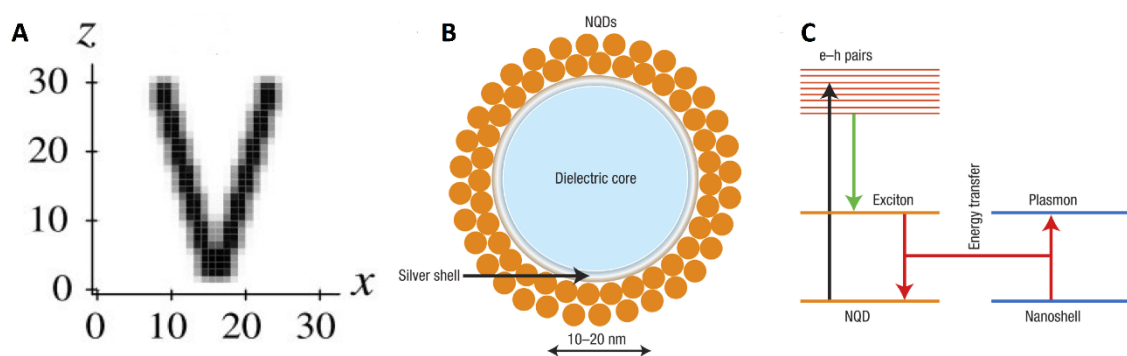


Figure 2.10 (a) Theoretical model of a V-shape SPASER proposed in 2003.^[3] (b) Theoretical model of a quantum dots-based SPASER proposed in 2008 and (c) the corresponding energy transfer scheme.^[134]

On the nanoscale, optical fields are almost purely electric oscillations, where the magnetic field component does not significantly participate in. The ability of a nanomaterial to support and concentrate such optical fields is due to the presence of localized optical modes smaller than optical wavelength.^[134] These

energy concentrated modes are surface plasmons, which are corresponding to oscillations of the electrons. Thus, noble metal nanoparticles, especially for gold nanoparticles, are chosen to provide the plasmon modes in experiments. Coupled surface plasmon of metal nanoparticles have attracted significant attentions, since the large electric field enhancement can be exploited for amplifying electromagnetic radiation. However, surface plasmon suffers from strong absorption loss that seriously limits the applications in waveguide, metal enhanced fluorescence as well as SPASER, due to the non-radiative surface plasmon relaxation.^[141] Amplification of surface plasmons could be a solution to this problem. Thus, an active medium has to be introduced, which provides gain at the plasmon frequency.^[142] A typical active medium is a system with dye molecules embedded in silica/polymer shells.

Under this mechanism, a SPASER based nanolaser was demonstrated in 2009 using a core-shell structure consisting of a gold spherical core and dye-doped silica shell that completely overcame the energy loss of localized surface plasmon and realized the SPASER concept.^[143] Since then, a series of investigations have been performed experimentally and theoretically towards understanding the mechanisms of a SPASER process.^[22,110,136,144–148] However, the experimental realization of SPASER is still a major challenge.

For a system coupled to an electromagnetic resonator, the spontaneous emission probability is increased over its bulk value. This is the concept of Purcell effect, which was introduced by Edward Mills Purcell in 1946.^[149] And the

recombination time reduced by a factor, which is now called Purcell factor. The equation of Purcell factor is as follow:

$$F_p = \frac{3\lambda_c^3 Q}{4\pi^2 V} \quad (2.15)$$

where V is the volume of the resonant mode, Q is the quality factor and λ_c is the wavelength in the material. It is a powerful tool for understanding and controlling light-matter interaction in resonators, and most of recent related works focus on the enhancement of spontaneous emission.^[150]

3. Synthetic Methods

3.1. Introduction

Nanoscience is the exploration of materials on nanoscale. The wet-chemical synthesis of such novel materials is an area at the crossroad of conventional inorganic cluster and classical colloid chemistry.^[19] These new materials will be on the foundation for nanotechnologies, which use and manipulate objects with at least one dimension in the nanometre range. Although quite a few approaches have been developed for the creation of such objects, wet chemistry promises to become the preferred choice, because of its relative simplicity and use of inexpensive materials.^[151,152] The aim of such synthesis is the preparation of various nanoparticles with controlled composition, shape and size. In this way, the influence factors on the physical, chemical, optical, electronic and catalytic properties of the material can be easily studied *via* various analytical methods. One of the most successful examples is the synthesis of gold nanoparticles with various shapes (nanorods, nanospheres, nanowires and nanocubes).^[153–157] To date, the mechanisms governing geometry control over particle growth are still far from being fully understood. It is obvious that the studies of morphology control are quite necessary to synthesize more complex and customized architectures.

2D materials are atomically thin sheets that exhibit unique electronic, optical and mechanical properties with remarkable potential for various applications.^[158]

For example, graphene is the prototypical 2D material composed of a honey comb network of sp^2 -hybridized carbon atoms, which exhibits high charge carrier mobilities, chemical inertness and high mechanical strength.^[159,160] So far, most conventional 2D materials have been derived from limited number of bulk solids consisting of weakly linked sheets, which reduces the opportunities to realize 2D materials by design. Therefore, it is highly required to develop the synthetic 2D materials, which could expand the variety of 2D materials with new and tailorable properties.^[158]

As the major work in this project is the synthesis of new nanoparticle and nanosheet systems, it is quite necessary to describe the materials preparation in detail. In this chapter, various synthetic methods involved in this project are stated in full including synthesis of colloid gold nanoparticles and their surface modifications with silica and polymers as well as 2D MnO_2 nanosheets fabrication. In addition, the function of reaction reagents is also introduced as well as the development background of each synthetic method.

3.2.Synthesis of Gold nanoparticles

3.2.1. Preparation of Gold nanospheres

Gold nanoparticles have been intensively studied because of their morphology-dependent physicochemical properties, which are of enormous interest for applications in photonics, catalysis and biomedicine.^[98,161,162] Among the conventional methods of synthesis of gold nanoparticles, the most popular one

for a long time has been the citrate-stabilized gold nanospheres. Initially developed by Turkevich et al. in 1951 and further modified by Frens in 1973, these citrate-stabilized gold nanospheres (size between 16 to 147 nm) could be acquired by reduction of HAuCl_4 *via* sodium citrate in aqueous solution.^[157,163,164] These citrate-capped gold nanospheres always show negative surface charges. Meanwhile, the seeding-growth procedure is another popular technique that has been used for a century. Recent studies have successfully prepared cetyltrimethylammonium bromide-capped gold nanospheres (positive surface charge) in the range 5-40 nm, whereas the sizes can be manipulated by varying the ratio of seed to metal salt.^[165,166] Typically, the step-by-step particle enlargement is more effective than a single-step seeding method to prepare fine gold nanospheres, where weak reducing agent and aqueous surfactant were used to control the growth condition and avoid secondary nucleation.

Here in this project, a facile method was used to prepare the positive-charged gold nanospheres.^[15,161,167] Typically, a CTAB (cetyltrimethylammonium bromide) solution (7.5 ml, 0.2 M) was mixed with 2.5 ml of 0.001 M HAuCl_4 and the mixture was stirred for 10 min. Then, 0.6 ml of ice-cold 0.01M NaBH_4 was added to the mixture, and slowly stirred for another 2 min. The colour of the solution turned from yellow to brown and then to soft pink in one hour. The solution was kept in room temperature for a day before usage. Double distilled water was used throughout the experiments. After two times of wash and centrifugation (12000 rpm, 30 min) by double distilled water, the gold colloid

was obtained and kept in water solution. As shown in Figure 3.1, the resulting particles is 12.9 ± 2.1 nm in diameter with a concentration of 1012 NPs/mL (calculated from its extinction coefficient).^[15,161,167]

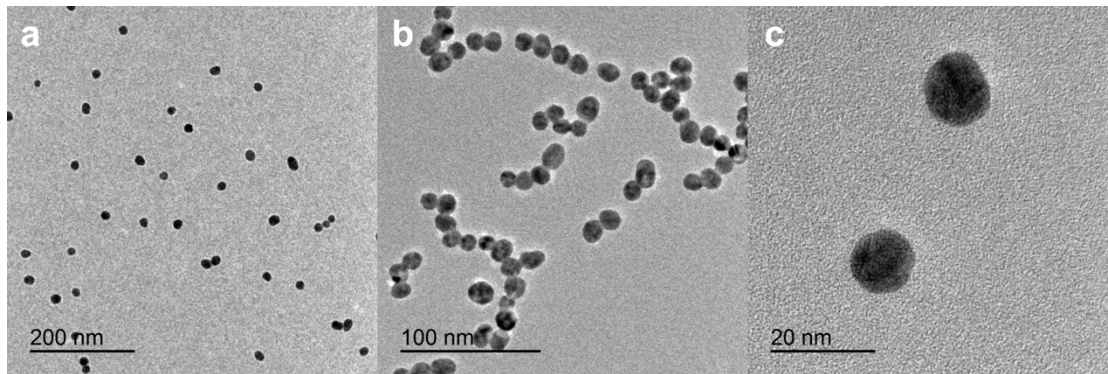


Figure 3.1 TEM images of gold nanospheres at (a) 200 nm, (b) 100 nm and (c) 20 nm scale.

3.2.2. Preparation of Gold nanorods

Based on the step-by-step growth of gold nanospheres, gold nanorods have been conveniently fabricated using the seeded-mediated synthetic route (also called seeded growth method) that was developed by Murphy's group in 2001. The basic idea of these syntheses is to use a strong reducing agent (sodium borohydride) in solution to prepare seed particles from gold salts; then, a weak reducing agent (ascorbic acid) is used to reduce more metal salt onto the seed particles, as shown in Figure 3.2.^[152,153,168] It is important to perform the second growth step in the presence of structure-directing agents (surfactant, e.g. CTAB) that would promote the formation of rod shapes.^[169] There are two general ways to grow GNRs. First of all, they can be prepared in the absence of additive impurity ions,

which normally result in longer rods but lower overall yields. Secondly, they could also be prepared in the presence of additive impurity ions, silver ions, which results in finer control of the nanorod aspect ratio and increased yield of rod-shaped particles, but does not work for growing extra longer nanorods.^[20] Although the exact growth mechanism is still unclear, silver ions in the growth solution are critical for the dimensional control of gold nanorods.^[15,168] In general, the higher the silver ion concentration, the higher the aspect ratio of the resulting GNRs.

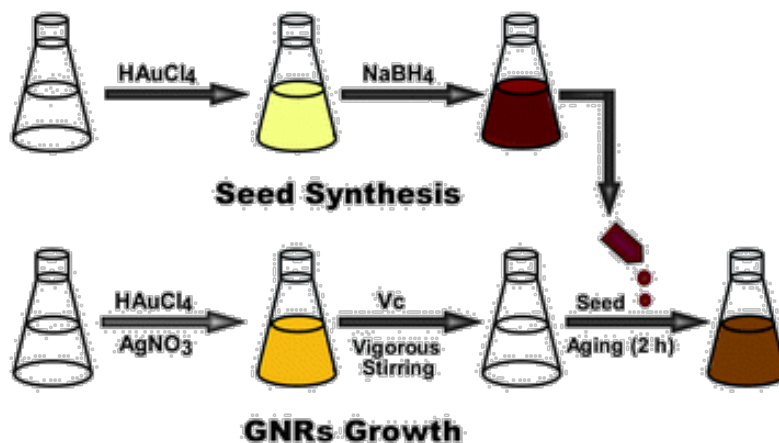


Figure 3.2 Schematic illustration of seeded-mediated method of gold nanorod growth.^[170,171]

In this project, GNRs were synthesized using a typical seeded growth method. To prepare the seed solution, a CTAB solution (9.75 mL, 0.1 M) was mixed with 0.25 mL of 0.001 M $\text{HAuCl}_4 \cdot 3\text{H}_2\text{O}$ and the mixture was stirred for 10 min. Then, 0.6 mL of ice-cold 0.01 M NaBH_4 was quickly added to the mixture, and slowly stirred for another 2 min. The solution was kept in room temperature for at least 3 h before usage. To prepare a growth solution, two flasks containing 475 mL of

0.1 M CTAB solution were prepared. After 10-minute's stirring, 25 mL of 0.01 M $\text{HAuCl}_4 \cdot 3\text{H}_2\text{O}$ was added under vigorous stirring for 7 min. To this solution, 2.50 and 3.75 mL of 0.01 M AgNO_3 was added to the two flasks, respectively. After 5-minute's gentle stirring, 2.75 mL of 0.1 M ascorbic acid was added to the growth solution and stirred for 5 min. Finally, 600 μl seeds were slowly added to the growth solution. The solution was kept 20 h at room temperature for rod growth. Afterwards, the as-prepared gold nanorods were purified *via* centrifugation at 12000 rpm for 20 min and dispersed in distilled water for further use. Figure 3.3 shows the SEM and TEM images of as-prepared short GNRs (AR=2.5) and long GNRs (AR=3.5) used in Chapter 4.

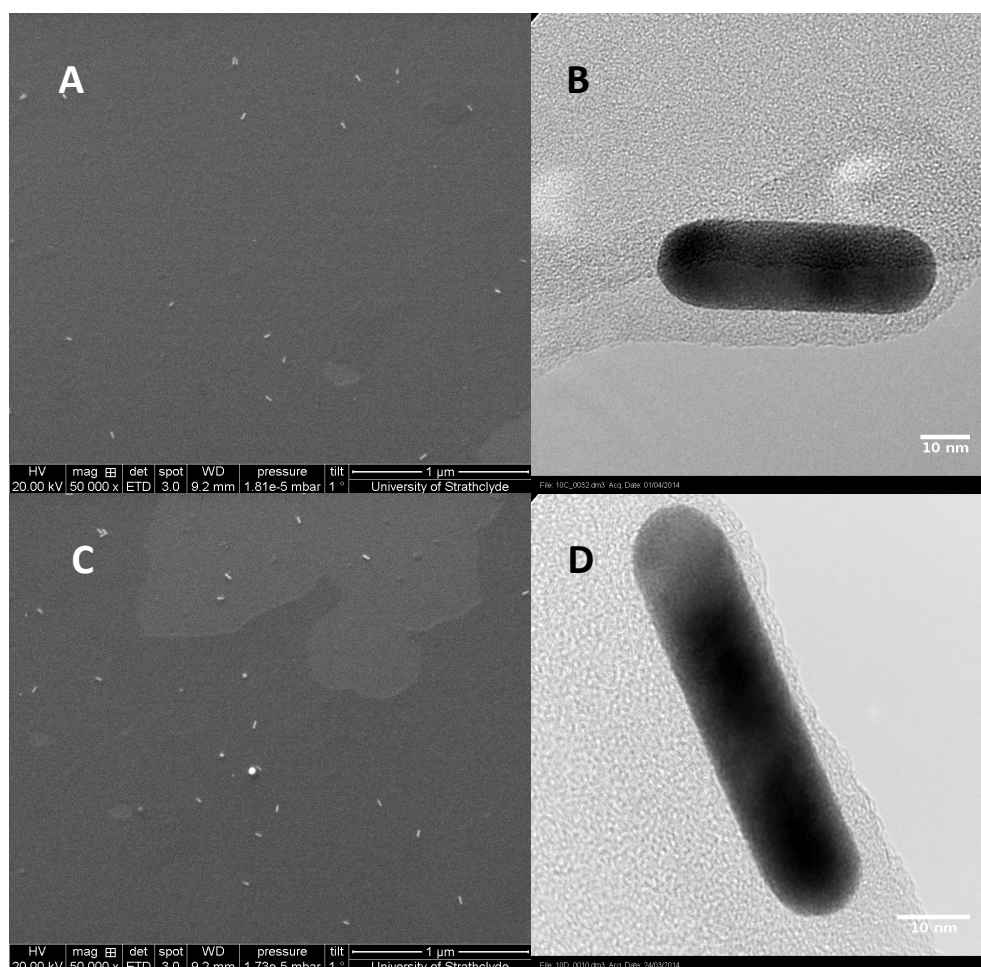


Figure 3.3 SEM and TEM images of short GNRs (a and b, AR 2.5) and long GNRs (c and d, AR 3.5).

3.3.Preparation of Gold nanorods Core-shell nanostructures

Effective wet chemical synthesis methods for nanoparticles of different shapes, sizes, and materials have been extensively studied. However, the successful integration of as-synthesized nanoparticles into useful devices is of great importance, because these nanoparticles often require application-specific coatings to passivate and/or fuse the nanoparticle to target molecules or surfaces. In addition, the extra coating may also be attractive, for it could provide enhanced

colloidal stability. Silica is an excellent candidate, for it is biocompatible and its surface can be further modified.^[172] Smooth, uniform silica shells have been successfully deposited based on the well-known Stöber method, where a surface modification procedure is always involved to neutralize the core surface charge before silica coating.^[173,174]

Meanwhile, a simpler mesoporous silica coating can be fabricated by a modified Stöber method for CTAB-capped nanoparticles, where CTAB surfactants were added to assist the silica growth.^[175,176] Previous studies suggest a three-step mechanism for the formation of the mesoporous shell: silica oligomerization in alkaline environment, formation of silica/CTAB primary particles and the aggregation of the primary particles to form the mesopores.^[176,177] In particular, the CTAB concentration is critical for the silica shell growth. As the increase of CTAB concentration, there are more free CTAB molecules than that on the surface of cores, which would lead to the generation of free mesoporous silica nanoparticles. This will reduce the amount of TEOS that can form the silica shell on core surface, which leads to the thickness decrease of silica shell.

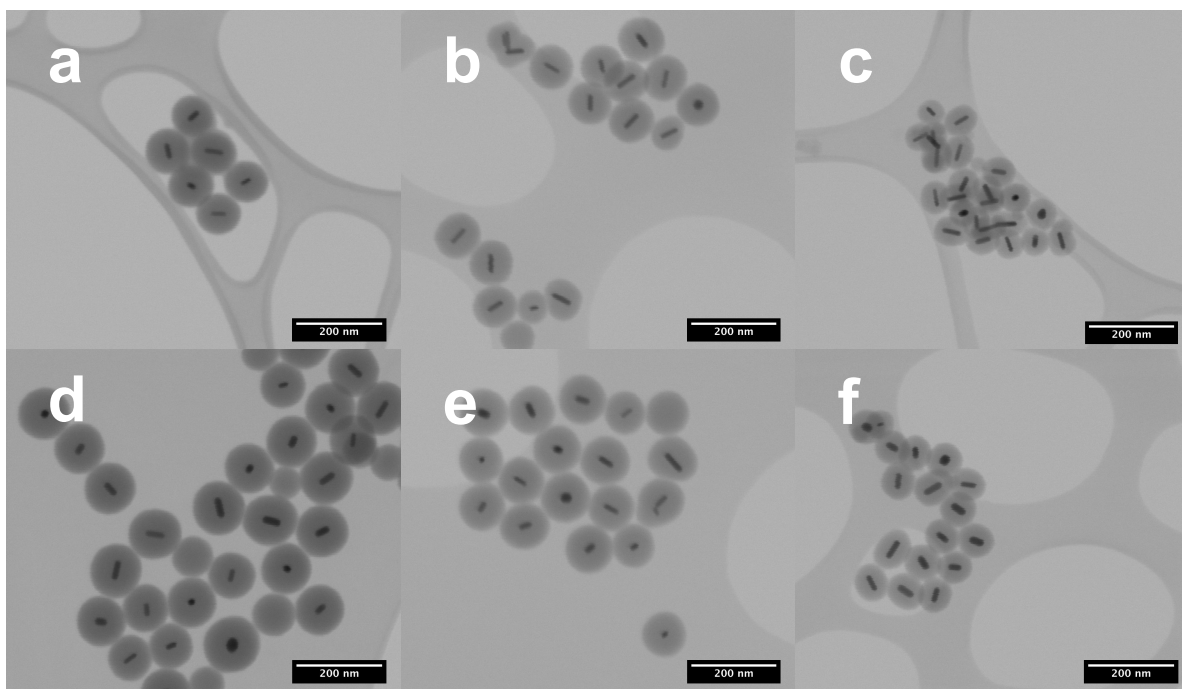


Figure 3.4 Bright field STEM images of the silica-coated long GNRs (AR 3.5) (a-c) and short GNRs (AR 2.5) (d-f).

In this project, a modified Stöber method was used to fabricate mesoporous silica-coated gold nanorods. After initial gold preparation, the as-prepared samples were centrifuged a second time at 8000 rpm for 20 min to minimize the CTAB concentration (less than 0.1 mM). Then, 0.1 M CTAB was added to 3 tubes to adjust the CTAB concentration to 0.4, 0.9 and 1.2 mM, respectively. After overnight mixing to allow the equilibration, 0.1 M NaOH was added and stirred for 30 min. Finally, 90 μ L of 20 % TEOS in methanol was slowly injected and mixed for another 20 h at room temperature. The as-prepared silica-coated gold nanorods were purified *via* centrifugation at 8000 rpm for 20 min and dispersed in 5 mL of ethanol. The morphology of these as-prepared samples is shown in Figure 3.4.

Silica coating of gold nanoparticles can be obtained with a good degree of control using the Stöber method. However, the extreme alkaline or acidic environment required by this method can limit the choice of dyes; Rh 800, for example, suffers a dramatic decrease in fluorescence intensity at $\text{pH} > 10$. A simple synthesis method was used to coat GNRs with polystyrene (PS), as schematically shown in figure 3.5. The growth of PS layer on GNRs is through an emulsion polymerization process. It is likely that hydrophobic styrene monomer diffuses into the CTAB surfactant bilayer on gold surface and forms a CTAB/styrene mixture structure on GNR.^[178,179] Arrival of the free APS molecules triggers polymerization of monomers inside this structure and initiates the growth of PS shell. At the same time, monomer droplets in the solution supply monomers which diffuse through the aqueous phase to facilitate the further polymerization and growth of the PS layer.^[180] To grow PS shells on different GNRs, 4 μl of styrene monomer were added to 10 ml GNRs solutions ($\text{OD} = 1$), respectively. After stirring for 5 min, 16 μl of 0.1M solutions of the initiator ammonium persulfate (APS) were added to above solutions and kept stirring for 15 min. The PS-coated GNRs were centrifuged (12000 rpm, 30 min) and re-suspended in 10 ml distilled water after growth for 1 day. The average PS shell thickness is around 3 nm, as shown in Figure 3.6.

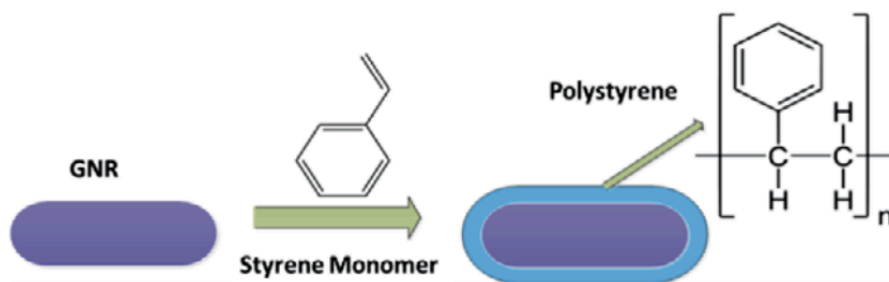


Figure 3.5 Scheme of polystyrene coating on CTAB-capped gold nanorod.

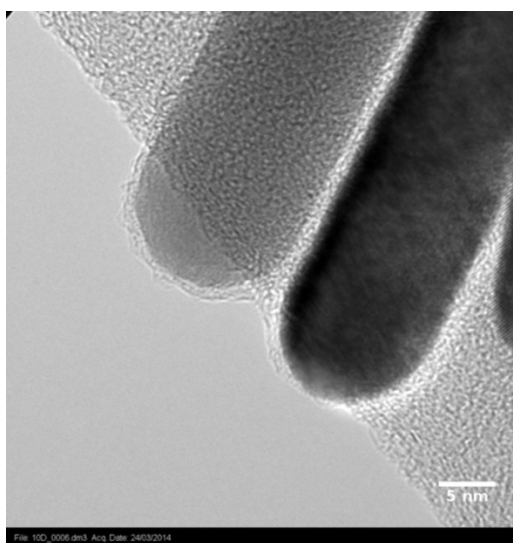


Figure 3.6 High resolution TEM image of PS-coated GNRs with a shell thickness of 3 nm.

3.4. Preparation of Au-MnO₂ nanocomposite

Nanosheets are a class of 2D nanomaterials with high specific surface area, characterized by a thickness of nanometres and lateral dimensions of sub-micrometres to micrometres. It is envisioned that single-layer MnO₂ nanosheet could expose maximal active sites for redox reactions to improve its electrochemical performance.^[181–184] Traditionally, MnO₂ nanosheets have been prepared through top-down methods, which always include a time-consuming

process of bulk material preparation, ion exchange and exfoliation.^[185] Recently, bottom-up strategies have emerged to synthesize MnO₂ nanosheets, such as chelating agent method and biphasic interface redox method, which show the advantages of easier operation and better thickness control.^[185,186] In particular in this project, a biphasic interface redox method was used to synthesize ultrathin δ -MnO₂ nanosheets. This biphasic interface redox method involves two simple reactions. First of all, ethyl acetate undergoes slow hydrolysis and forms acetic acid and ethanol under refluxing condition at the interface between pure ethyl acetate and aqueous KMnO₄. Then, the generated ethanol reacts with KMnO₄ to form brown MnO₂ nanosheets. And the ultrathin 2D δ -MnO₂ structures are stabilized by the CH₃COO⁻ group.^[187]

To prepare the ultrathin δ -MnO₂ nanosheets, 150 mL of 2 mM KMnO₄ was mixed with 40 mL ethyl acetate (99.8 %) in a 250 mL boiling flask under vigorous stirring. The reaction was heated by a water bath at 85 °C for 12 h. Meanwhile, a condenser was utilized to prevent the evaporation of the solvent. This process continued until a great deal of brownish particles formed, which revealed the end of the reaction. The ultrathin δ -MnO₂ nanosheets could be obtained by centrifugation (4000 rpm, 5 min), washed by double distilled water and ethanol several times to remove the excess potassium permanganate and ethyl acetate. Finally, 15 mL ethanol was added to the centrifuge tube to obtain 10 g/L δ -MnO₂ standard suspension. Figure 3.7 and 3.8 shows the SEM and HRTEM images of

δ -MnO₂ with an \sim 3 nm thickness, where the ultrathin 2D nanostructures were clearly identified.

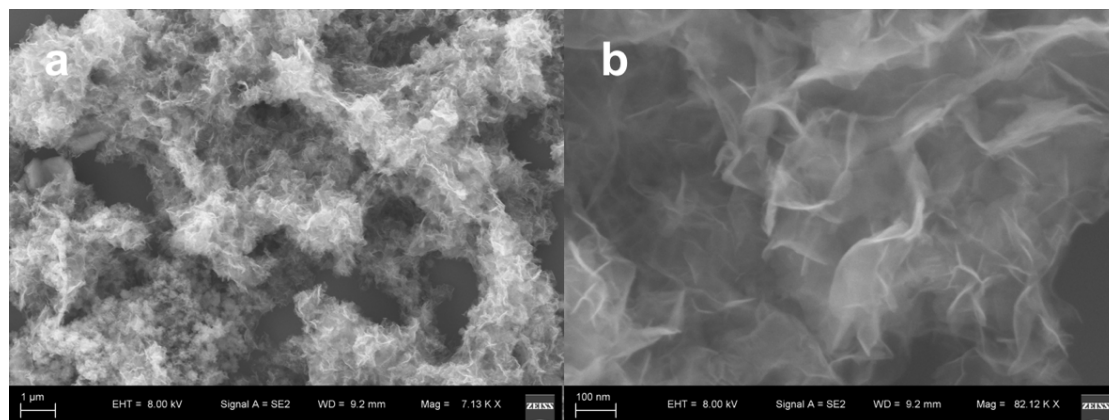


Figure 3.7 SEM images of 2D δ -MnO₂ nanosheets on (a) 1000 nm and (b) 100 nm scale.

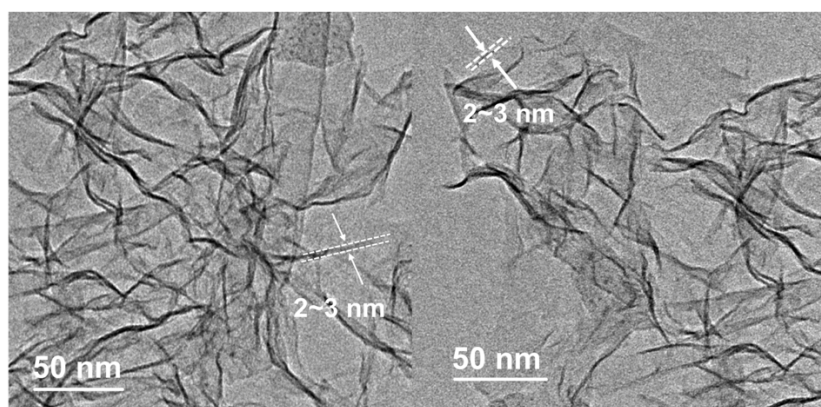


Figure 3.8 TEM images of 2D δ -MnO₂ nanosheets on 50 nm scale, which show the 2-3 nm thickness of δ -MnO₂ nanosheets.

The Au-MnO₂ nanocomposites were prepared *via* a self-assemble method. Gold nanospheres were assembled to the δ -MnO₂ nanosheets through the electrostatic interaction. Firstly, 10 mg (1 mL) of δ -MnO₂ were re-dispersed into 10 mL ethanol under vigorous stirring. Then, 4, 6, 8 and 10 ml of as-prepared

CTAB-capped gold nanospheres colloid solution was added dropwise. After stirring for 3 h and sitting for 1 h, the resulting sample Au- δ -MnO₂ nanocomposites were collected as sample 1, 2, 3 and 4, respectively. The concentration of gold loading is 2.3, 4.2, 6.5 and 8.3 wt % based on the calculation, where the sample 0 was the pure δ -MnO₂ without gold loading. As shown in Figure 3.9, it is a typical TEM image of Au-MnO₂ nanocomposite with 8.3 wt % gold loading. In addition, these samples were denoted as L1-L4 under laser radiation and A1-A4 after the laser radiation in Chapter 6.

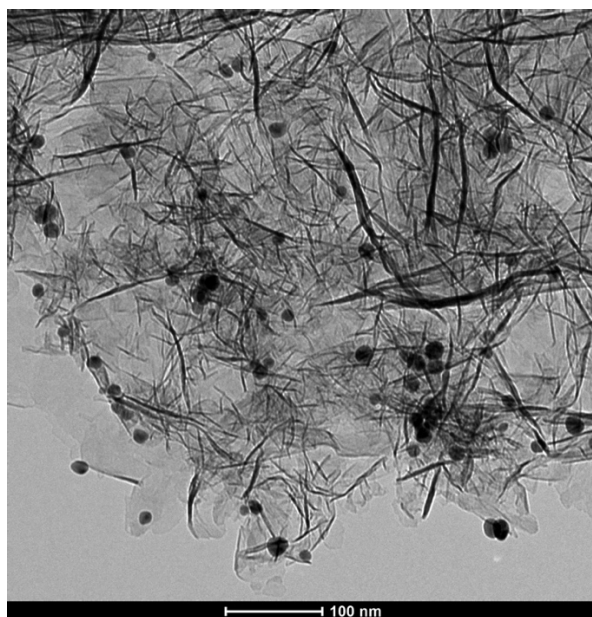


Figure 3.9 Typical TEM image of Au-MnO₂ nanocomposites (8.3 wt % gold loading) on 100 nm scale.

4. Dye-doped Polystyrene-coated GNRs towards SPASER

4.1.Introduction

In this section, we have investigated the synthesis of dye-doped GNRs core/shell structures. Rh 800 was chosen because of its absorption and emission near 700 nm. Silica coating of gold nanoparticles can be obtained with a good degree of control using the Stöber method.^[174] However, the extreme alkaline or acidic growth environment required by this method can limit the choice of dyes; Rh 800, for example, suffers a dramatic decrease in fluorescence intensity at pH>10. Here in this chapter, a new type of fluorescent core/shell nanoparticles were proposed through emulsion polymerization. A modified PS coating method is applied to grow GNR core-PS shell particles doped with Rh 800 at neutral pH.^[178] The thickness of the PS shell can be controlled by varying the synthesis conditions. Static optical spectroscopy studies revealed stable dye doped core/shell nanoparticles in water solution. Dynamic fluorescence spectroscopic measurements revealed strong energy coupling between gold cores and the surrounding Rh 800, indicating energy loss compensation of surface plasmon resonance.

4.2.Methods

To dope dye into the coating, 4 µl of styrene monomer and 0.1 mg of Rh 800 were added to 10 ml of the GNRs solution (OD = 1). The SEM and TEM images of the short GNRs (L mode at 710 nm, AR=2.5) and long GNRs (L mode at 783

nm, AR=3.5) used in this part are shown in Chapter 3 (Figure 3.3). The short GNRs show an average length of 36.2 nm and the long GNRs shown an average length of 50.7 nm. The solution was stirred for 20 min and 16 μ l of a 0.1 M APS was added. The polymerization was allowed to take place at room temperature. The solution was stirred for 20 min then sat for 2 h. The Rh 800-doped PS-GNRs were centrifuged and washed twice (12000 rpm) and re-suspended in distilled water for characterization. The weak electrostatic interaction between polystyrene and Rh 800 assists in maintaining the dye in the coating layer.

4.3. Results and Discussion

4.3.1. PS-coated GNRs

Figure 4.1A shows extinction spectra of GNRs with PS shells grown in 2 hours, 1 day, 2 days and 1 week with a monomer concentration of 12 μ l. The effect of coating on the optical response of GNRs is apparent in comparison to that of original GNRs. As mentioned in Chapter 1, the factor weighting ϵ_m is 2 for spherical particles and $(1 - P_j)/P_j$ for prolate spheroids. Based on the Equation 1.14-1.17, the $(1 - P_j)/P_j$ could be much larger than 2 as the increase of aspect ratio. This would lead to the generation of the longitudinal plasmon peak as well as the increased sensitivity to the dielectric environment. As shown in Figure 4.1, the wavelength of the T mode (short wavelength peak as labelled in Figure 4.1A) remains almost unaltered, but the L mode (long wavelength peak as labelled in Figure 4.1A) shifts to shorter wavelengths due to a decrease in the local

permittivity around the gold core introduced by the PS shell. The increased blue shifts at longer growth time suggest the formation of thicker coating layers. Figure 4.1B compares the blue shift of 5 samples of different monomer concentration (4, 6, 8, 10, and 12 μl) after growth for 2 hours, 1 day, 2 days, and 1 week. No difference was found among the five samples after 2 hours' growth. However, the difference becomes obvious after 1 day's growth, where samples of higher monomer concentration have larger blue shifts. Plotting the blue shift versus time for all concentrations (Figure 4.1C) shows varying growth rates and a dependence of growth rate on monomer concentration. In the case of 4 μl , growth completed after 2 hours; while in the case of 12 μl , a constant growth rate maintained for 2 days followed by a slow growing process until one week had elapsed. This suggests that the thickness of PS shell can be controlled by varying monomer concentration and growth time.

The growth of PS layer on GNRs is through an emulsion polymerization process. It is likely that hydrophobic styrene monomer diffuses into the CTAB surfactant bilayer on the gold surface and forms a CTAB/styrene mixture structure on GNR. Arrival of the free APS molecules triggers the polymerization of monomers inside this structure and initiates the growth of PS shell. At the same time, monomer droplets in the solution supply monomers which diffuse through the aqueous phase to facilitate the further polymerization and growth of the PS layer^[188].

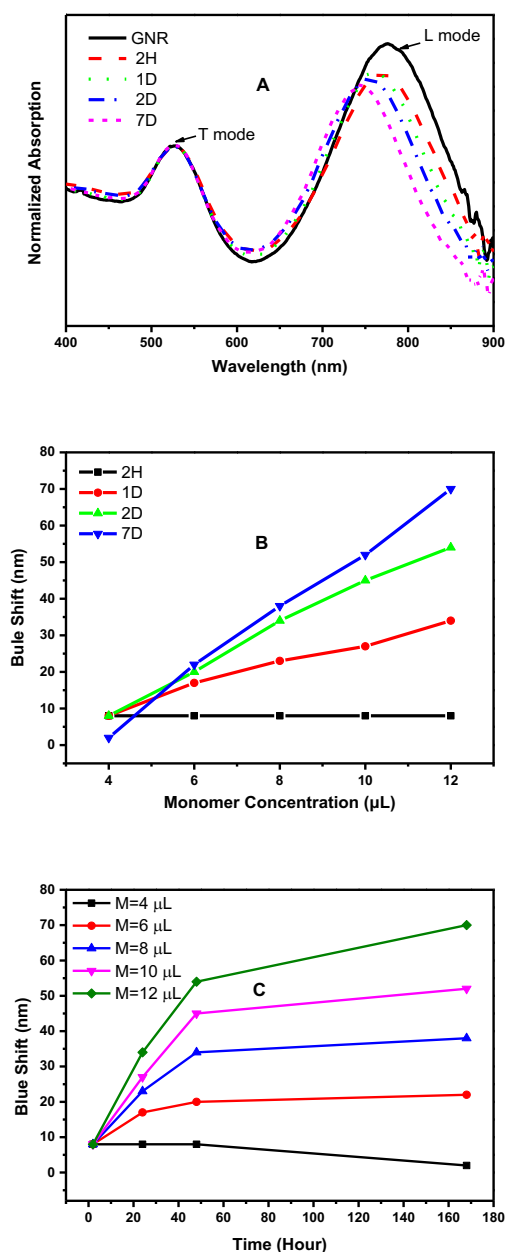


Figure 4.1 (A) Normalized UV-vis extinction spectra of PS-coated GNRs with monomer concentration of 12 μl after growth for 2 hours, 1 day, 2 days, 1 week, and original GNRs (all normalized against T modes); (B) and (C) the blue shift of L modes as a function of monomer concentration and time during PS-coated GNRs growth, respectively.

4.3.2. Rh 800 Doped PS-coated GNRs

Figure 4.2 shows the normalized UV-vis extinction spectra of original GNRs, PS-coated GNRs, Rh 800-doped PS GNRs, and Rh 800 doped PS spheres as a control sample. A 10 nm blue shift was found from PS-coated GNRs, consistent with what found in Figure 4.1. The extinction spectrum of Rh 800-doped PS GNRs shows an absorption peak at 690 nm sitting on a broad absorption band (L mode of GNRs). The 690 nm peak resembles the main absorption of Rh 800, indicating a successful dye doping.

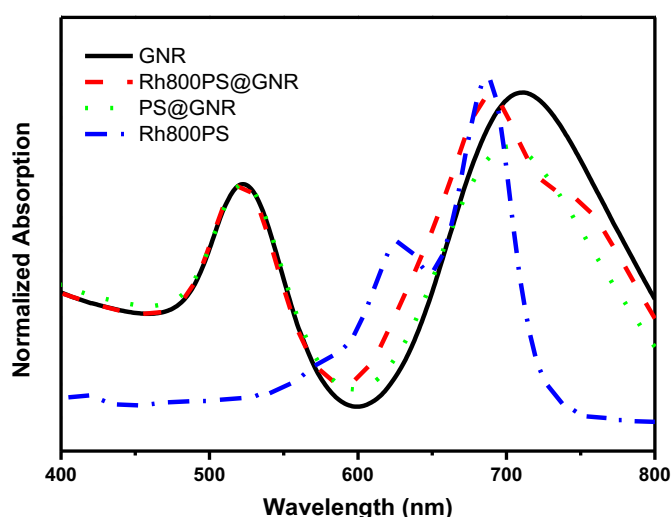


Figure 4.2 Normalized UV-vis extinction spectra of original GNRs (black), PS-coated GNRs (green), Rh 800-doped PS GNRs (red), (all normalized against T modes) and Rh 800-doped PS sphere (blue).

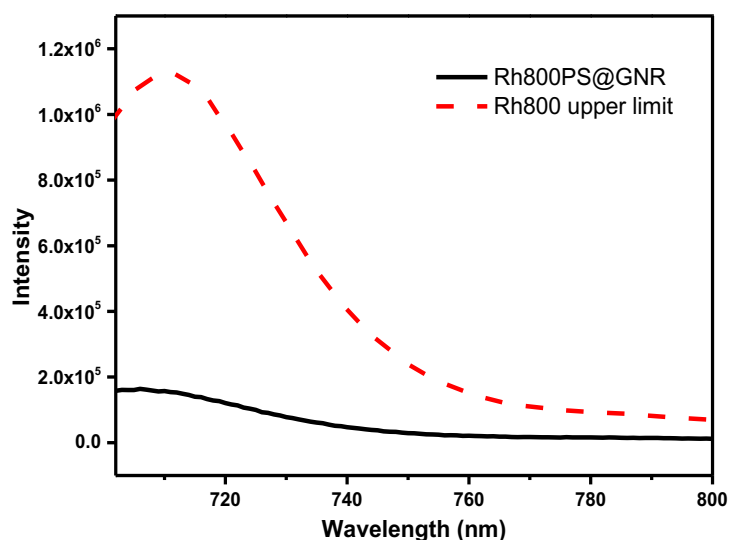


Figure 4.3 Emission spectra of Rh 800-doped PS GNRs (black) and Rh 800 of calculated upper-limit concentration in water solution (red).

Figure 4.3 shows the emission spectra of Rh 800-doped PS GNRs in comparison with that from a Rh 800 solution (3.17×10^{-6} M in 10 ml water solution). This molar concentration of the dye molecules was estimated by the known initial dye concentration in the reaction taking away the free dye molecules remaining in the solution after the reaction (concentration of dye in supernatant after centrifugation). This calculation provides the upper limit concentration of Rh 800 doped in PS shells. It is clear that the fluorescence intensity of dye doped PS-GNRs is about an order of magnitude lower than that from free dye in solution. Furthermore, dynamic fluorescence spectroscopic studies compare the fluorescence decay process of Rh 800 in PS-GNR particles and Rh 800 in PS spheres, as shown in Figure 4.4A and B. The decay curve of Rh 800 in PS spheres can be fitted with a single exponential function, generating

a lifetime of 0.71 ns. Two exponential fitting of the decay curve of Rh 800 in PS-GNRs revealed a first discrete lifetime component of 0.71 ns (85.8%) and second discrete lifetime component of 0.1 ns (14.2%). While the first lifetime is consistent with that of Rh 800 in PS spheres, the second lifetime is much shortened. Furthermore, the fluorescence decay curve was also fitted by the maximum entropy method in order to explore the likely distribution of decay components, as shown in Figure 4.4A. In contrast to a single lifetime distribution centred at 0.72 ns for Rh 800 in PS sphere as shown in Figure 4.4C, two lifetime distributions centred at 0.10 ns (10.8%) and 0.70 ns (89.2%) for Rh 800 in PS-GNRs are revealed in Figure 4.4D, confirming the lifetime shortening indicated by the discrete two exponential analysis. Both decreased fluorescence intensity and lifetime suggest an energy coupling between dye and GNRs.

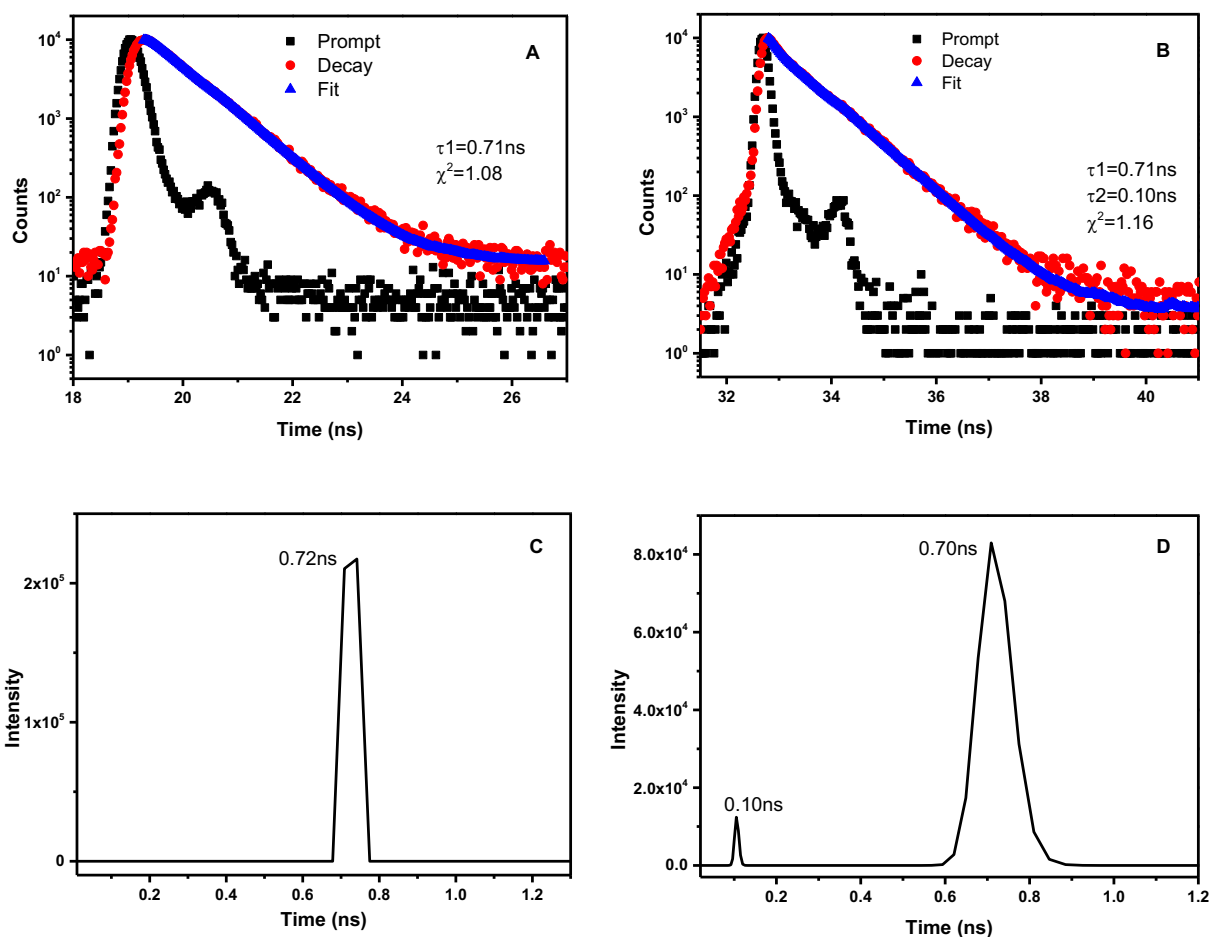


Figure 4.4 Fluorescence decay curves of Rh 800-doped PS sphere (A) and Rh 800-doped PS GNRs (B); Lifetime distribution of Rh 800-doped PS sphere (C) and Rh 800-doped PS GNRs (D) by maximum entropy method.

4.3.3. Influence of Surface Plasmon on Energy Transfer

Energy transfer from dye to gold nanoparticles has been described using a surface energy transfer (SET) model, where the distance dependence of the transfer rate scales at 4th power^[92,189]. Previous studies have found that this energy transfer is enhanced when a surface plasmon mode overlaps with the excitation wavelength where the strong local electromagnetic field arising from surface plasmon resonance enhances the absorption of dyes^[98,101]. In order to study the surface plasmon effect on the energy transfer between Rh 800 and GNRs, longer GNRs with an L mode at 783 nm were also used. The extinction spectrum of Rh 800 doped PS-GNRs-L, Figure 4.5, shows a shoulder on the short wavelength side of the surface plasmon mode which matches the main absorption peak of Rh 800 in a PS environment.

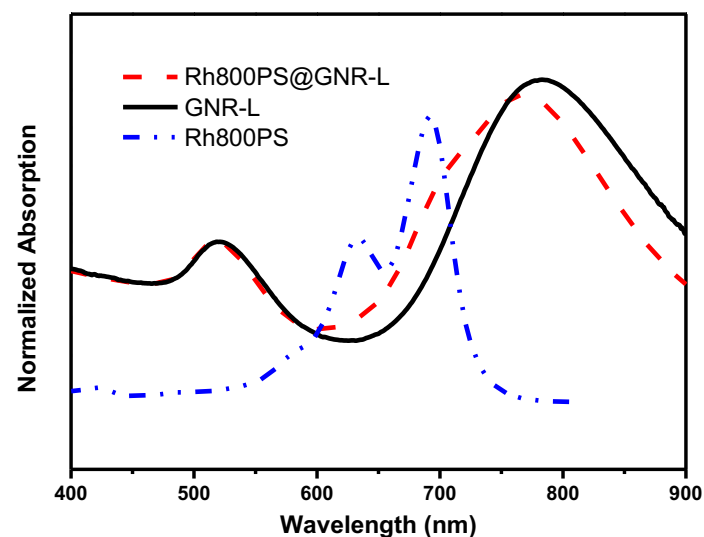


Figure 4.5 Normalized UV-vis extinction spectra of original GNRs (black), Rh 800-doped PS GNRs-L (red), (all normalized against T modes) and Rh 800 doped PS sphere (blue)

The equivalent SET distance d_0 can be calculated from $d_0 = \left(\frac{0.225c^3\Phi_{Rh800}}{\omega_{R800}^2\omega_F K_F}\right)^{1/4}$, where c is the speed of light, ω_{Rh800} the frequency of the donor electronic transition and the ω_F Fermi frequency, and K_F Fermi vector of the metal.^[92,96] Using $\Phi_{Rh800} = 0.01$, $\omega_{Rh800} = 2.7 \times 10^{15} \text{ s}^{-1}$, $\omega_F = 1.2 \times 10^8 \text{ cm}^{-1}$, and $K_F = 8.4 \times 10^{15} \text{ s}^{-1}$, d_0 is calculated as 53.5 \AA .^[92,98,189]

Figure 4.6A shows decreased fluorescence intensity from Rh 800-doped PS-GNRs-L by about an order of magnitude, compared to the Rh 800 reference sample ($5.39 \times 10^{-6} \text{ M}$ in 10 ml water solution). A shorter lifetime component of 0.28 ns (4.2%) was observed along with a lifetime of 0.73 ns (95.8%) for the Rh 800-doped PS-GNRs-L particles, as shown in Figure 4.6B. Figure 4.6C shows the lifetime distribution of Rh 800-doped PS GNR-L fitted by the maximum entropy method, and it indicates the two components of 0.13 ns (2.2%) and 0.71 ns (97.8%) lifetime for Rh 800 in PS GNRs-L. The existence of a shorter lifetime component together with decreased fluorescence intensity indicates an energy transfer from dye to GNR. Compared to GNRs with a longitudinal surface plasmon of 710 nm, the red shift of SP from long GNRs reduced the spectral overlap between the absorption of dye and SP, as well as the excitation of SP, resulting in a weakened energy transfer process.

4.4. Conclusions

In summary, we have successfully synthesized a new type of fluorescence GNR core-PS shell nanoparticles *via* emulsion polymerization at neutral pH. The thickness of the PS shell can be controlled by varying monomer concentration and growth time. Decrease in the fluorescence intensity and lifetime of Rh 800 were observed in comparison to that from dye doped PS spheres, indicating an energy transfer from Rh 800 to GNRs. Moreover, this energy transfer is enhanced when the SP overlaps with the absorption and emission of Rh 800. This energy transfer compensates for the energy loss of surface plasmon and thus brings further insight towards creating a nanorod-based wavelength tuneable SPASER.

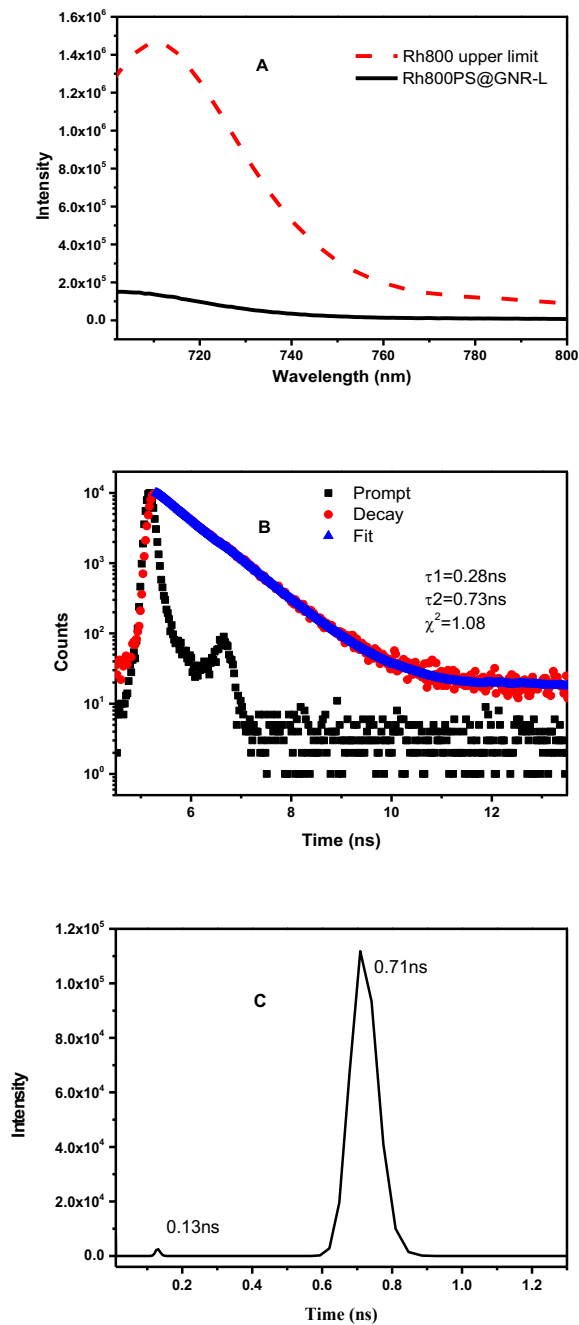


Figure 4.6 (A) Emission spectra of Rh 800-doped PS GNRs-L (black) and Rh 800 of calculated upper-limit concentration in water solution (red); (B) fluorescence decay curve and (C) lifetime distribution of Rh 800-doped PS GNR-L, respectively.

5. Revealing the Plasmon Enhanced Fluorescence by Mega 520/Silica Gold Nanorods

5.1. Introduction

Gold nanorods have attracted considerable attentions during the past decade due to their extraordinary capability to manipulate light absorption and emission.^[1,3,10,168,190] The collective and coherent charge density oscillations on their surface give rise to two plasmonic resonance bands defined by aspect ratio and can be tuned from visible to near-infrared.^[19,20,153,191] Light could be strongly absorbed and scattered at the resonant wavelength. The electromagnetic fields near the nanoparticles are greatly enhanced due to the charge confinement, which has already been widely applied from two-photon imaging, nanolaser, Raman resonances, photothermal heating to fluorescence enhancement.^[21,110,143,155,192–194]

Fluorescence detection is a key technology for biosensing and bioimaging science.^[94] Since the continuing need for increased sensitivity, there has been a growing interest on metal enhanced fluorescence. Fluorescence enhancement was first introduced by attaching fluorophores to the vicinity of metal films; and later, noble metal nanoparticles were applied due to their unique surface plasmon resonance effect.^[2,76,108,195] As aforementioned in the Chapter 2, the fluorescence intensity can be quantified by $I = \gamma_{ex} \cdot Q \cdot f_{eq}$, where γ_{ex} is the fluorescence excitation rate, Q is the emission quantum yield of the fluorophore and f_{eq} is the light collection constant of the measurement system.^[80,84,106] Thus, the

enhancement of fluorescence emission intensity is usually realized in two ways: enhancement of the excitation rate as the result of the concentrated local field and/or the quantum yield due to the modification of radiative decay rate of the fluorophore.^[7,108] However, in some instances quenching could be observed as well as fluorescence enhancement, for the excited fluorophore can relax rapidly through non-radiative energy transfer into the surface plasmon resonance.^[84,110,189] In addition, both quenching and enhancement are highly distance-dependent. Thus, from almost 100 % quenching to more than 1000-fold enhancement in fluorescence emission intensity have been observed by scientists in their recent reports.^[73,84,112,113,161,196]

So far, many experimental and theoretical works in plasmon-enhanced fluorescence have been done, however, the exact mechanism is still not quite clear, especially in what dominates plasmon-enhanced fluorescence emission. To this end, we present the study of a gold nanorods/silica spacer/large Stokes shift dye core-shell system to further investigate this issue. In this system, two types of gold nanorods were applied with aspect ratio 2.5 and 3.5, respectively. Then 25 nm, 35 nm and 45 nm silica spacer was coated on the gold nanorods *via* a modified Stöber method.^[176,177] The large Stokes shift dye, Mega 520, was finally attached to the surface of the mesoporous silica, which could be excited at 520 nm and emit at 672 nm. At the same time, mesoporous silica nanospheres (MSNs) were used as the control sample and went through the same dye loading procedure. Static optical spectroscopy studies revealed stable dye-attached

core/shell nanoparticles in solution. Dynamic fluorescence spectroscopic measurements were carried out to reveal the contributions of quantum yield enhancement and excitation rate enhancement.

5.2.Methods

5.2.1. Preparation of the Mega 520 doped Silica-coated GNRs

After initial gold preparation, the as-prepared samples were centrifuged a second time at 8000 rpm for 20 min to minimize the CTAB concentration (less than 0.1 mM). Then, 0.1 M CTAB was added to 3 tubes to adjust the CTAB concentration to 0.8, 1.0 and 1.2 mM, respectively. After overnight mixing to allow the equilibration, 0.1 M NaOH was added and stirred for 30 min. Finally, 90 μ L of 20 % TEOS in methanol was slowly injected and mixed for another 20 h at room temperature. The as-prepared silica-coated gold nanorods were purified *via* centrifugation at 8000 rpm for 20 min and dispersed in 5 mL of ethanol.

The Mega 520 dye molecules were doped into the mesoporous silica shell through a facile physical process. Typical, 30 μ L of 0.01 M of dye molecules were added to 10 mL MSNs ethanol solution. Then, 1 mL of 10 mg/mL poly(allylamine hydrochloride) (PAH, in 10 mM NaCl, $M_{W(PAH)} = 15000$ g/mol) solution were slowly added to the mixture. After gentle stirring for about 24 h, the colloid solution was centrifuged twice at 8000 rpm to remove the access dye molecules and disperse in 3 mL methanol for further optical measurements.

5.2.2. Preparation of the Mega 520 doped Silica Nanoparticles

Dye-doped mesoporous silica nanoparticles (MSNs) were prepared following the same procedure used for silica growth and dye loading. Firstly, 0.1 M CTAB was added to a tube of 10 mL double distilled water to adjust the CTAB concentration to 1 mM. Then, 0.1 M NaOH was added and stirred for 1 h. Later, 90 μ L of 20 % TEOS in methanol was slowly injected and mixed for another 20 h at room temperature. The as-prepared MSNs were purified *via* centrifugation at 8000 rpm for 20 min and dispersed in 5 mL of ethanol. Finally, 30 μ L of 0.01 M of dye molecules were added to 10 mL MSNs ethanol solution followed by 1 mL of 10 mg/mL PAH. After gentle stirring for about 24 h, the colloid solution was centrifuged twice at 8000 rpm to remove the excess dye molecules and disperse in 3 mL methanol for further optical measurements.

5.3. Results and Discussion

Mega 520 dye was chosen for this study for its large Stokes shift of 150 nm and the potential of background-free bioimaging applications. As shown in Figure 5.1, the maximum absorption and emission peak of Mega 520 are 520 nm and 672 nm, respectively. Meanwhile, gold nanorods of two aspect ratio, AR 2.5 (short) and AR 3.5 (long), were prepared using the well-known seed-mediated procedure (see in Chapter 3). Silica coating was carried out through a modified Stöber method.^[172,174,197] Through carefully control of the reaction parameters, such as reaction time and CTAB concentration, one can achieve highly reproducible and robust silica coating of various thickness. Typically, after

centrifugation, GNRs were transferred to various concentrations of CTAB growth solution. As the increase of CTAB concentration, silica coating thickness would drop from 40 nm to 10 nm.^[177] Previous studies have shown that the growth of mesoporous silica on metal nanoparticle surface is attributed to a multi-stage mechanism: silica oligomerization, formation of silica-CTAB particles and aggregation of these silica-CTAB particles.^[175,176] This means that the increase of CTAB concentration would lead to the generation of free MSNs, which reduces the amount of TEOS that can form the silica shell.

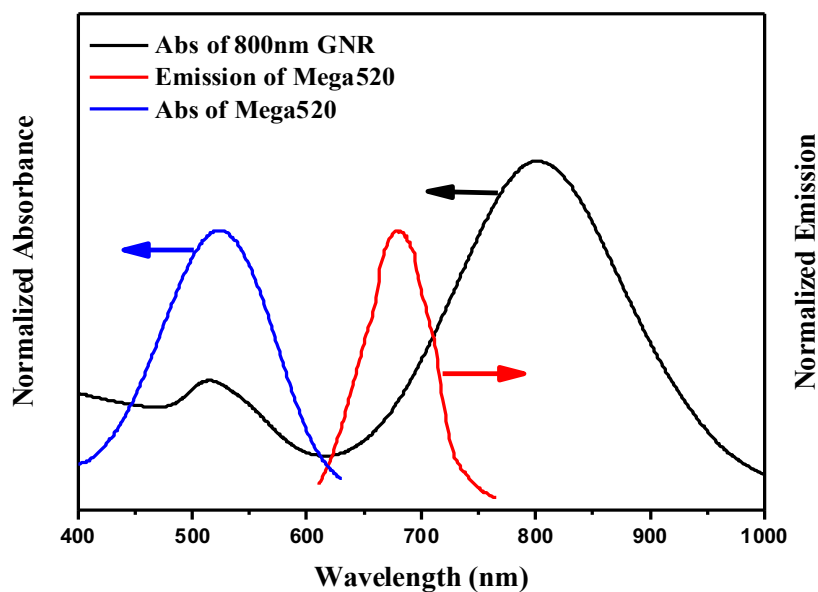


Figure 5.1 The absorption, emission spectra of Mega 520 dye and a typical absorption spectrum of gold nanorods.

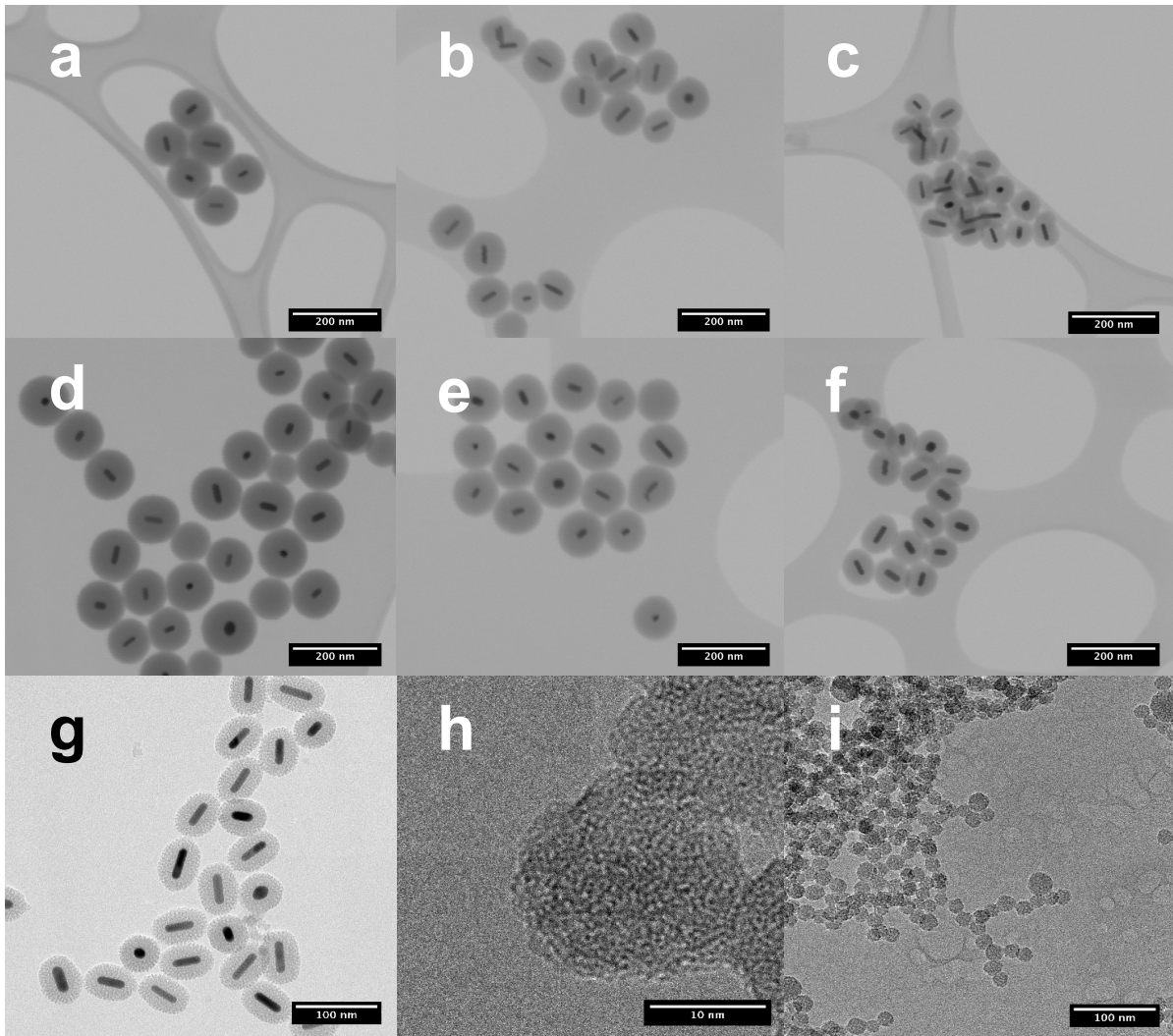


Figure 5.2 Bright field STEM images of the silica-coated long GNRs (aspect ratio = 3.5) (a-c) and short GNRs (aspect ratio = 2.5) (d-f). High resolution TEM image of a typical silica-coated GNRs (g) and silica spheres on (h) 10 and (i) 100 nm scale.

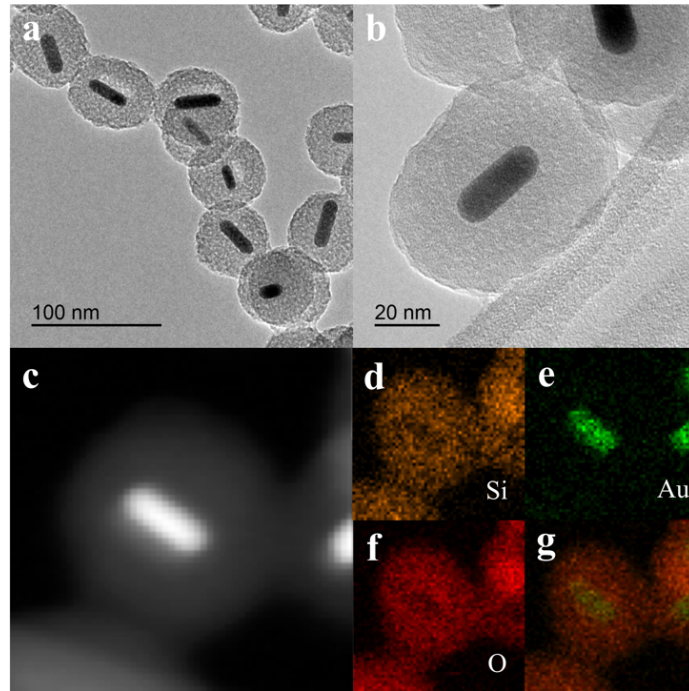


Figure 5.3 (a)TEM and (b) high resolution TEM images of 35 nm silica-coated short GNRs. (c) Dark field STEM image and 2D STEM-EDX elemental mapping images of (d) Si, (e)Au and (f) O, and (g) silica-coated GNRs (overlay).

Under this silica synthesis mechanism, by tuning the concentration of CTAB from 0.4, 0.9 to 1.2 mM, 45, 35 and 25 nm thick silica shell were coated to the gold nanorod (sample L4, L9 and L12 for long GNRs; and S4, S9 and S12 for short GNRs), as shown in scanning transmission electron microscopy (STEM) images in Figure 5.2a-f. Figure 5.2 g shows the transmission electron microscopy (TEM) image of long gold nanorods with a 25 nm silica shell (sample L12); and Figure 5.2 h and i are the TEM images of control sample MSNs on 10 and 100 nm scale. Figure 5.3 shows the TEM and STEM-EDX elemental mapping images of short gold nanorods with a 35 nm silica shell (sample S9), which indicates the

successful coating of silica. The shell thickness results derived from STEM images are shown in Figure 5.4, where 25, 35 and 45 nm are the thicknesses along short axis (maximum thickness) of gold nanorods.

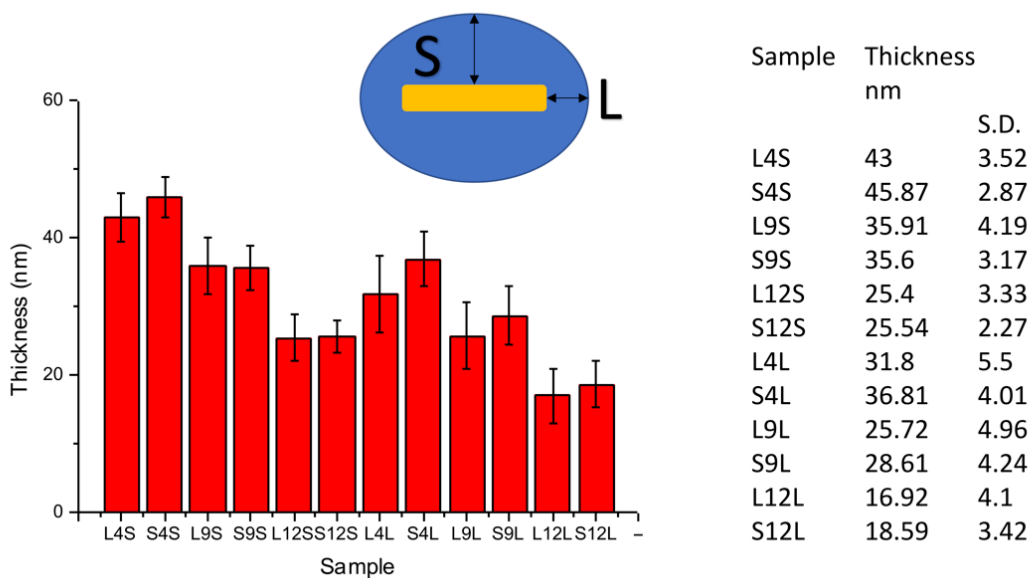


Figure 5.4 The average thickness of silica coating on long and short GNRs of L4, L9, L12, S4, S9 and S12 samples.

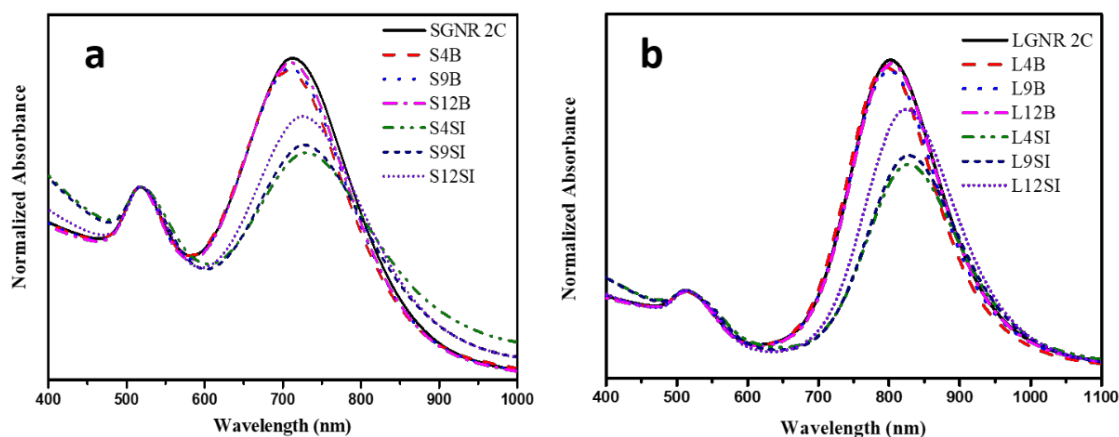


Figure 5.5 The absorption spectra before and after silica coating on short (a, 700 nm) and longer (b, 800 nm) GNRs.

Figure 5.4 shows average thickness of silica coating along long and short axis of gold nanorods derived from STEM images over 100 particles. Both the thickness along short and long axes of GNRs were calculated with standard deviation provided. It shows that the thickness of silica coating decreases from 45 to 25 nm as the CTAB concentration increases from 0.4 to 1.2 mM. Previous study shows that the amount of free CTAB in solution is critical on silica shell growth.^[177] As the increase of CTAB concentration, there are more free CTAB molecules than that on the surface of gold nanorods, which would lead to the generation of free MSNs. This will reduce the amount of TEOS that can form the silica shell on gold surface, which leads to the thickness decrease of the silica shell. Moreover, Figure 5.4 also exhibits that silica coating are thicker along short axis than that along long axis and the influence of aspect ratio is minimal. Figure 5.5a shows the UV-vis absorbance of short GNRs (AR 2.5) after centrifugation,

GNRs in CTAB solution (4, 9 and 12 mM) and as-prepared silica-coated GNRs. Comparing to the bare gold nanorods after two times of centrifugation, the CTAB-capped GNRs S4, S9 and S12 do not show obvious difference. The effect of the silica coating on the optical response of GNRs is apparent in comparison to that of CTAB-capped GNRs. While the wavelength of the transverse mode remains unaltered, the longitudinal plasmon mode shifts to longer wavelengths due to the increase in the local permittivity around gold core introduced by the silica shell. The slightly increase in the red-shift of the longitudinal plasmon peak from S12 to S4 suggests that the formation of coating layers of increasing thickness, which are consistent with STEM images (Figure 5.2a-c). In addition, the clear ratio of transverse and longitudinal plasmon spectra also indicates no obvious aggregations of GNRs or silica-GNRs. Figure 5.5b shows that the long GNRs (AR 3.5) also have the same trend where thicker silica shell formed at a lower CTAB concentration that results in a larger red shift. The obvious red-shifts of longitudinal plasmon peak are good indicators of successful silica-coating on the gold core, which are again in line with the results revealed from STEM images (Figure 5.2d-f).

The dye doped silica-coated GNRs were prepared through the facile electrostatic process. Previous researches show that dye molecules can be successfully assembled to gold nanorods through layer by layer polymer wrapping with long term stability.^[72,198,199] Zeta-potential measurements, as

shown in Figure 5.6, also confirm the success of this facile electrostatic process. Since the silica shell and Mega 520 are both surface negative charged, a positive charged PAH layer is applied to fix dye molecules on the surface of silica shell. In the existence of mesoporous structure, it is highly possible to form a PAH-dye-silica-GNRs structure, where the free dye molecules inside the pores can be wrapped in PAH layer. In addition, a dye-PAH-dye-silica-GNRs structure may also exist due to the electrostatic interaction. However, the two time of purifications may largely reduce the formation of dye-PAH-dye-silica-GNRs structure. Thus, the affection from dye-PAH-dye-silica-GNRs structure is negligible. Figure 5.7a shows the UV-vis spectra of Mega 520 silica-GNRs after the dye loading. It is clearly shown that the transverse and longitudinal surface plasmon peaks are almost unaltered, which indicates that there is no aggregation during the 24 h of dye loading. In addition, the dye absorption at 520 nm is not obvious, which may be caused by the overlapping of transverse plasmon peak and dye absorption. After careful evaluation, the dye/silica-coated GNRs ratio is up to 300. This ratio was estimated by the known initial dye concentration in the reaction taking away the free dye molecules remaining in the solution after the reaction (concentration of dye in supernatant after centrifugation). Figure 5.7b exhibits the steady state fluorescence intensity spectra of as-prepared samples excited at 532 nm. It is clearly shown that the fluorescence intensity increases as the thickness of silica shell decrease. The dye/silica-coated short GNRs, whose longitudinal plasmon (at 700 nm, AR 2.5) largely overlaps with the wavelength

of dye emission, have lower emission intensities comparing to the Mega 520 silica control sample. On the other hand, the dye/silica-coated long GNRs, whose longitudinal plasmon (830 nm, AR 3.5) mismatches the wavelength of dye emission, have overall higher fluorescence intensities. Based on the data in Figure 5.7b, we plot the fluorescence intensity enhancement, as shown in Figure 5.8. The fluorescence intensity of L4, L9 and L12 were enhanced by 1.4, 2.0 and 2.1 times.

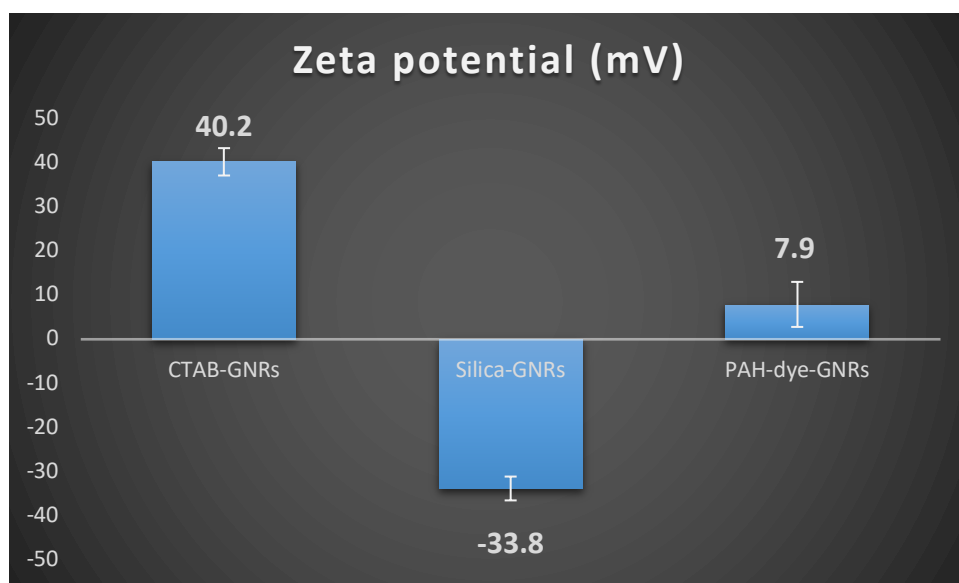


Figure 5.6 Zeta-potential of long CTAB-capped GNRs, 35 nm silica-coated GNRs and PAH-dye wrapped silica-coated GNRs.

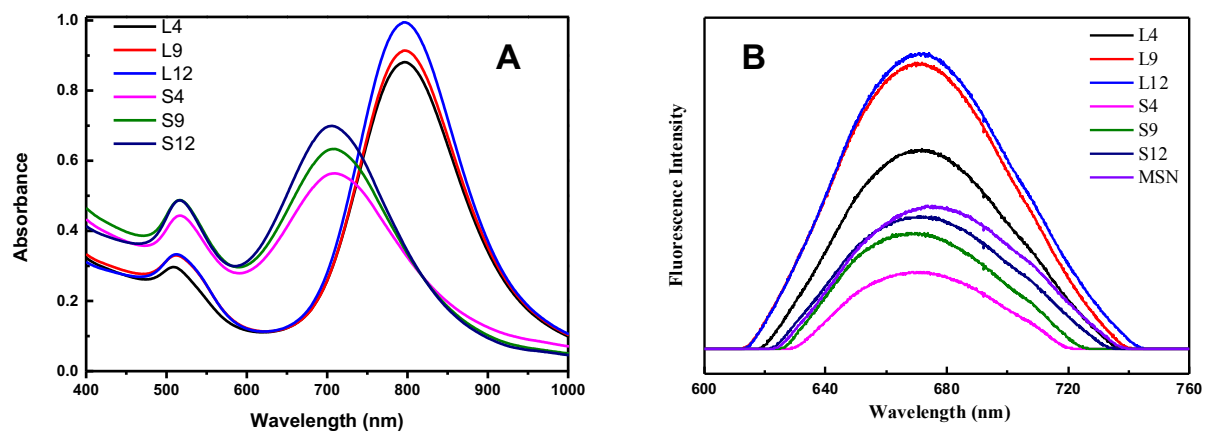


Figure 5.7 (a) The absorption spectra of various silica coating GNRs after dye loading and (b) emission spectra of all samples.

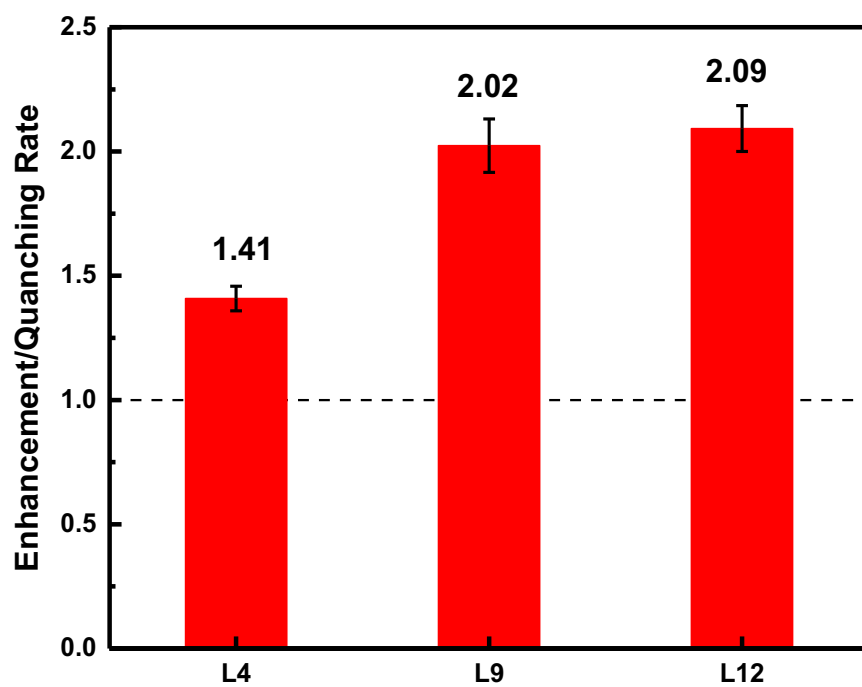


Figure 5.8 Enhancement rate (sample fluorescence intensity/control intensity) of the as-prepared sample L4, L9 and L12 at peak wavelength.

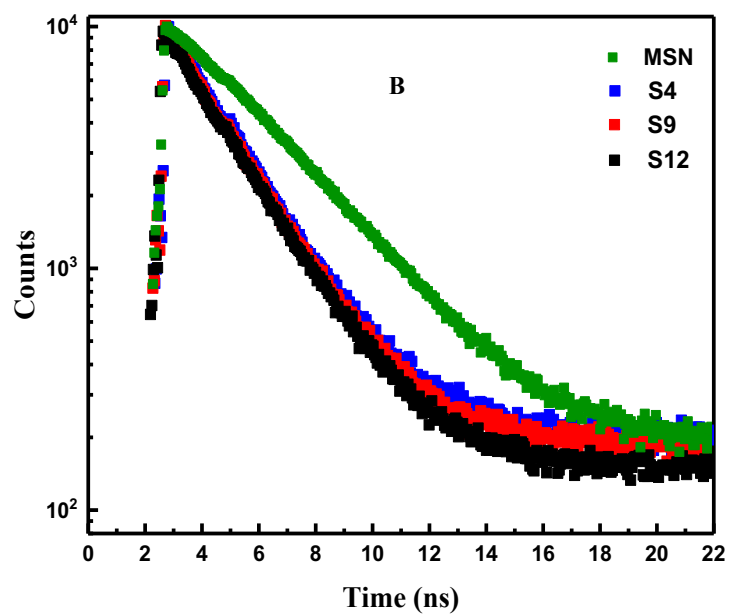
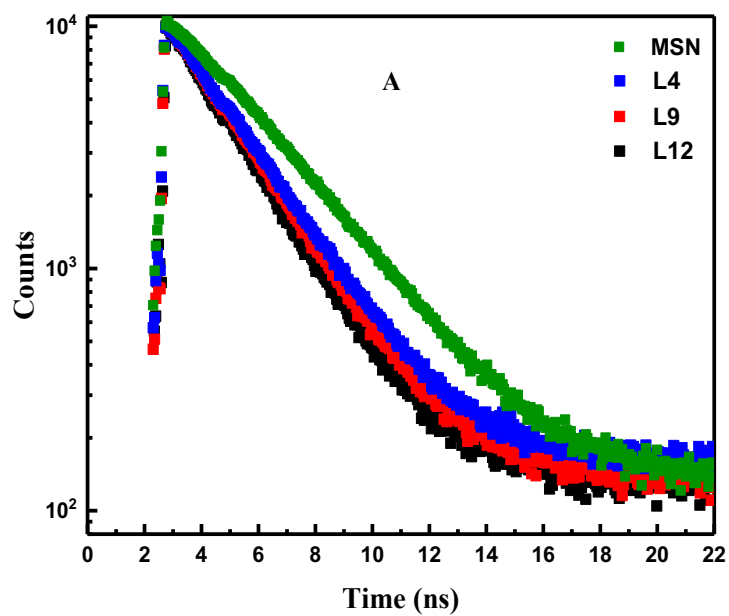


Figure 5.9 Steady state fluorescence decay curve of (a)MSN, L4, L9 and L12; and (b) MSN, S4, S9 and S12 samples.

Table 5.1 Fluorescence lifetime results of as-prepared samples.

| Sample | t₁ | A₁ | t₂ | A₂ | χ² |
|----------------|----------------------|----------------------|----------------------|----------------------|----------------------|
| MSN 520 | 1.67 ns | 100 % | N/A | N/A | 1.01 |
| S4 | 1.62 ns | 2.88% | 1.43 ns | 97.12 % | 1.09 |
| S9 | 1.61 ns | 2.12% | 1.44 ns | 97.88 % | 0.98 |
| S12 | 1.62 ns | 2.73% | 1.41 ns | 96.27 % | 1.09 |
| L4 | 1.73 ns | 2.11 % | 1.56 ns | 97.89 % | 1.03 |
| L9 | 1.70 ns | 2.71 % | 1.51 ns | 97.29 % | 1.11 |
| L12 | 1.66 ns | 2.16 % | 1.49 ns | 97.84 % | 1.07 |

Figure 5.9 and Table 5.1 exhibits the fluorescence intensity decay curves from time-resolved fluorescence spectroscopy measurements and lifetime analysis results of the as-prepared Mega 520/silica-coated GNRs samples. In contrast to a single lifetime distribution centred at 1.67 ns for Mega 520 in MSNs (control sample), two lifetime components were revealed for Mega 520 silica-coated GNRs. In addition to the first lifetime in the range of 1.6 to 1.7ns, similar to the typical lifetime of Mega 520 in MSNs, a major second (“faster”) lifetime component (slightly shortened lifetime component, from 1.41 to 1.56 ns in various samples) was found. Since the average dye-gold distance is larger than 20 nm, the weak interaction is revealed by the approximately 15 % decrease in fluorescence lifetime. The first component of regular lifetime is less than 3 %, which may be related to a small amount of PAH-dye-silica nanoparticles in each system. For Mega 520 silica-coated GNRs (AR 3.5), both first and second components of lifetime are decreased as the decrease of silica thickness from 45 to 25 nm. In addition, more complex Mega 520 silica-coated GNRs (AR 2.5)

systems do not show any obvious trend from fluorescence lifetime results. The decrease of the fluorescence intensity for Mega 520 silica-coated GNRs (AR 2.5) may be caused by the overlap of the longitudinal SP and emission of Mega 520 at around 670 nm.

As discussed before, the observation of fluorescence intensity can be described by $I = \gamma_{ex} \cdot Q \cdot f_{eq}$, where γ_{ex} is the excitation rate of the fluorophore, Q is the emission quantum yield of the fluorophore and f_{eq} is the light collection efficiency of the measurement system. The components of enhancement on quantum yield and excitation rate may be revealed. Without metal nanoparticles, the quantum yield and fluorescence lifetime can be expressed as $Q = \Gamma / (\Gamma + k_{nr})$ and $\tau = 1 / (\Gamma + k_{nr})$. When the gold nanoparticles involved, the quantum yield and lifetime would be modified to $Q_M = \frac{\Gamma + \Gamma_m}{\Gamma + \Gamma_m + k_{nr}}$ and $\tau_M = \frac{1}{\Gamma + \Gamma_m + k_{nr}}$, which was discussed in Chapter 2. If we assume that the quantum yield of Mega 520 is in the range from 0.05 to 0.8; then the Γ , k_{nr} , Γ_m and Q_M can be calculated for each quantum yield based on the lifetime results at Table 5.1. Thus, the components of enhancement by quantum yield (Eqy) and excitation rate (Eec) can be further revealed based on the data in Figure 5.8. The plots of Eqy and Eec versus each quantum yield for L4, L9 and L12 are on shown in Figure 5.10. It is clearly shown that enhancement due to quantum yield modification is more significant than that arising from an increased excitation rate for fluorophore with low quantum yield of 0.05, while the latter becomes more important at a quantum

yield larger than 0.3. Taking quantum yield of 0.3 is an example, the exact Eqy and Eec for L4, L9 and L12 can be revealed, as shown in Table 5.2.

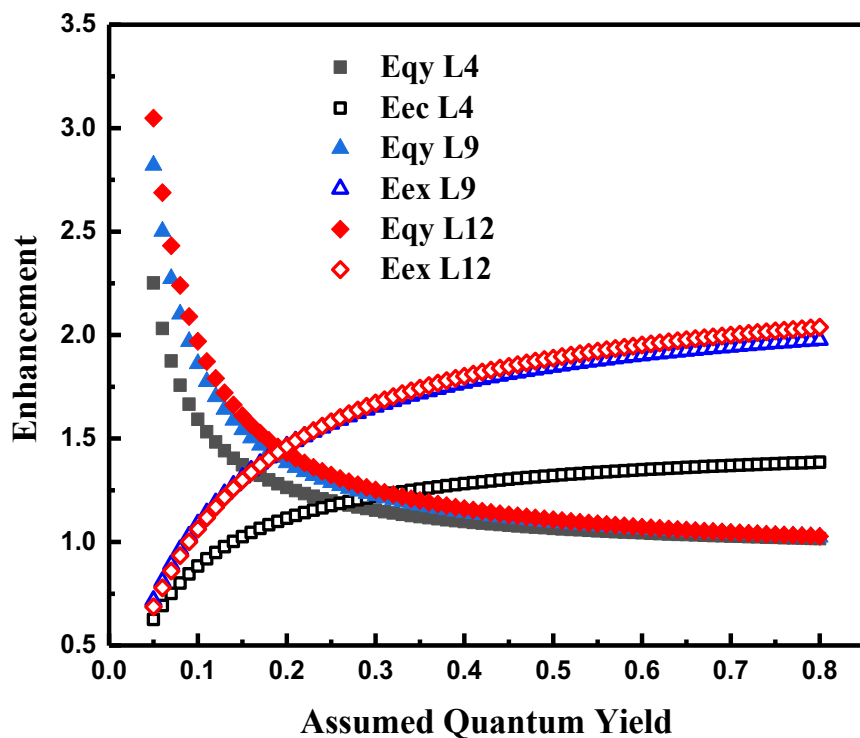


Figure 5.10 The calculated enhancement from quantum yield and excitation versus assumed quantum yield of Mega 520 from sample L4, L9 and L12.

Table 5.2 Enhancement components of L4, L9 and L12.

| Samples | Ef | Eqy | Eex |
|----------------|----------------|----------------|----------------|
| L4 | 1.40826 | 1.15369 | 1.22065 |
| L9 | 2.02363 | 1.22355 | 1.65389 |
| L12 | 2.09227 | 1.25149 | 1.67181 |

However, the situation is more complex for short gold nanorods system since there is a spectrum-overlap at the emission of Mega 520 and L mode plasmon absorption peak. Based on the data in Figure 5.7b, we plot the fluorescence intensity quenching, as shown in Figure 5.11. The fluorescence intensity of S4, S9 and S12 were quenched to 54 %, 0.75 % and 0.93 %. However, the fluorescence intensity is increased as the decrease of shell thickness. This complexity on quantum yield and fluorescence lifetime can also be revealed by the further decrease in fluorescence lifetime of the second component. Since the dye-gold distance is controlled by the silica spacer and the geometry is very similar for the samples with same silica thickness (as shown in Figure 5.4), we can assume that E_{ec} is unaltered for the samples with same silica thickness. This means that S4, S9 and S12 would take up the E_{ec} of L4, L9 and L12, respectively. Thus, the components of enhancement by quantum yield E_{qy} can be further calculated based on the E_{ec} data in Figure 5.8. The plots of E_{qy} and E_{ec} versus each quantum yield for S4, S9 and S12 are on shown in Figure 5.12. Taking quantum yield of 0.3 is an example, the exact E_{qy} and E_{ec} for S4, S9 and S12 can be revealed, as shown in Table 5.3.

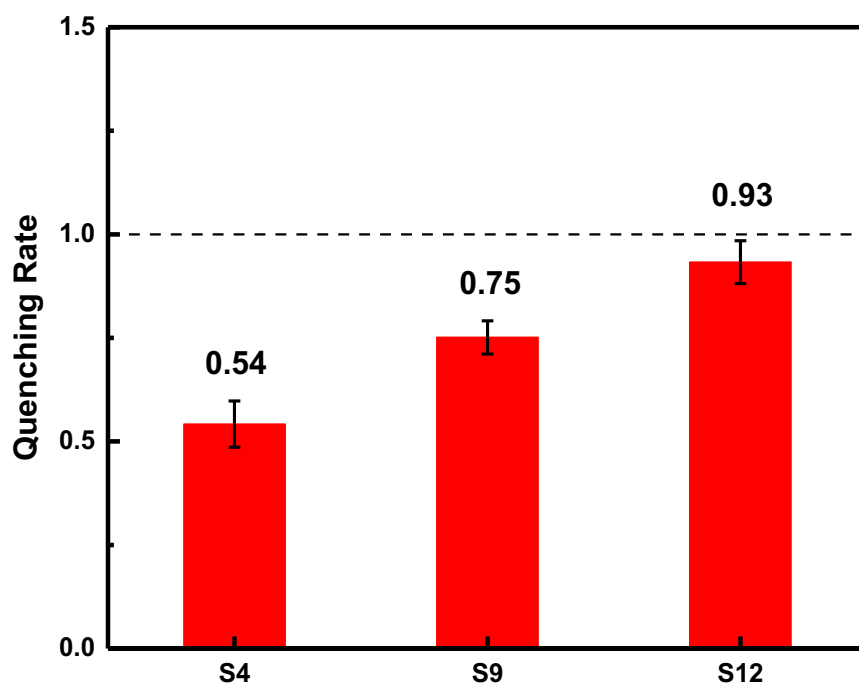


Figure 5.11 Quenching rate (sample fluorescence intensity/control intensity) of the as-prepared sample S4, S9 and S12 at peak wavelength.

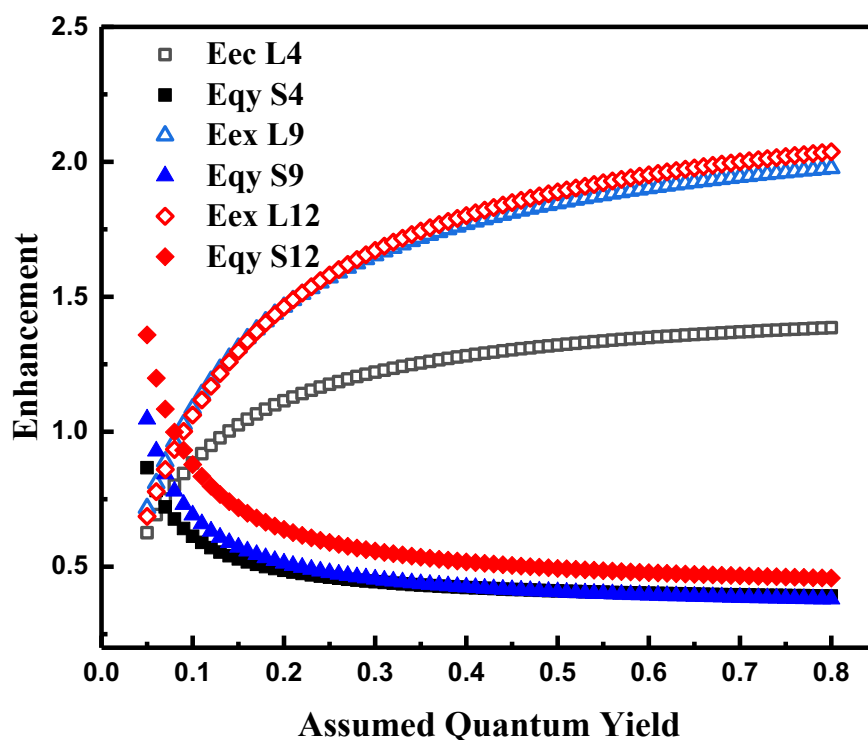


Figure 5.12 The calculated enhancement from quantum yield and excitation versus assumed quantum yield of Mega 520 from sample S4, S9 and S12, based on the results at Figure 4.11.

Table 5.3 Enhancement components of S4, S9 and S12.

| Samples | Ef | Eeq | Eex |
|---------|---------|---------|---------|
| S4 | 0.54192 | 0.44396 | 1.22065 |
| S9 | 0.75108 | 0.45413 | 1.65329 |
| S12 | 0.93287 | 0.55799 | 1.67181 |

5.4. Conclusions

In summary, we present the study of a gold nanorods/silica spacer/large Stokes shift dye core-shell system to further study energy transfer and plasmon enhanced fluorescence. In this system, two types of gold nanorods were applied with aspect ratio 2.5 and 3.5, respectively. Then, two types of Mega 520 doped silica-coated GNRs with various silica thickness (25, 35 and 45 nm) were successfully prepared through a modified Stöber method, revealed by the high resolution TEM, STEM and element mapping images. The steady stated fluorescence measurements reveal that the fluorescence intensity for L4, L9 and L12 is increased as thickness of silica shell decrease, where the intensity of L4, L9 and L12 is enhanced by 1.4, 2.0 and 2.1 times. However, the large overlap of dye emission and longitudinal plasmon (S4, S9 and S12) leads to a decreased fluorescence intensity comparing to the Mega 520 silica control sample. Time-resolved fluorescence spectroscopy measurements show that in contrast to a single lifetime distribution centred at 1.67 ns for Mega 520 in MSNs, a major second lifetime component (slightly shortened lifetime component, from 1.41 to 1.56 ns in various samples) also exists. Since the average dye-gold distance is larger than 20 nm, the weak interaction is revealed by the approximately 15 % decrease in fluorescence lifetime. The decrease of the fluorescence intensity for Mega 520 silica-coated GNRs (AR 2.5) may be caused by the large overlap of the longitudinal SP and Mega 520

emission at around 670 nm. Finally, the contributions of quantum yield enhancement and excitation rate enhancement were revealed.

6. Plasmon-promoted electrochemical oxygen evolution catalysis

6.1. Introduction

Advanced materials in efficient harvesting, storage and utilization of renewable energy are of great importance in current energy research.^[193,200–204] The splitting of water, either electrically or photo-driven, has been widely studied for energy conversion into fuels and chemicals; in particular, the oxygen evolution reaction (OER) plays a vital role by giving protons and electrons to these processes.^[205–211] However, the intrinsic process of OER is sluggish and suffers from severe efficiency loss as well as large overpotentials.^[48,201,212–214] Therefore, finding proper OER catalysts is critical in accelerating the reaction, reducing the overpotential and improving the overall efficiency. In the past few years, transition metal based materials (such as cobalt oxides and nickel oxides) have been applied as OER catalysts under alkaline and neutral conditions for the benefits of cost effectiveness, good stability and low pollution.^[52,214–217] It is believed that the transition metal ions in materials undergo progressive oxidation to higher valence states prior to the OER, during the electrochemical process.^[52,58–60] This indicates that the highly oxidative metal ions may be the active sites of OER catalysts. And the corresponding investigations confirm that the OER catalytic performance may depend on the outer electron states of the transition metal species.^[61–63]

Localized surface plasmon resonance (LSPR) is the coherent charge density oscillations confined to noble metal (such as gold and silver) nanostructures, which is excited by the electromagnetic irradiation (light).^[1,110,190,218,219] This light phenomenon attracts a great deal of attention, because it is capable of efficient absorbing photons and converting light energy to hot electrons (also referred to “energetic electrons”) and enhanced local electric field.^[13,220–225] During the LSPR process, hot electrons will be excited and transferred, which can lead to the hole generation on the surface of plasmonic materials to capture external electrons, simultaneously.^[13] Meanwhile, the local electric field of the plasmonic nanostructures could be greatly enhanced, which leads to many unique features such as plasmon enhanced fluorescence and SPASERS.^[143,177] Such a LSPR effect enables the efficient energy harvest and conversion for photovoltaics, photo/electrochemical catalysis.^[7,220,226–228] For instance, Wu and co-workers proposed a Au@SiO₂@Cu₂O sandwich nanostructure to enhance the solar-light harvesting and the energy-conversion efficiency, which greatly enhanced the visible-light photocatalytic activity as compared to the semiconductor alone.^[229] Snaith et al. investigated incorporation of core-shell Au-SiO₂ nanoparticles into dye-sensitized solar cells and demonstrated plasmon-enhanced light absorption, photocurrent, and efficiency for both iodide/triiodide electrolyte based and solid-state dye-sensitized solar cells.^[193] Inspired by the above phenomena, hybridizing the transition metal catalyst with plasmonic metal nanoparticles would cause electron-confined transition metal species, and eventually promote the OER

catalytic performance. Thus, the investigation of transition metal species with plasmonic nanoparticle hybrids is highly necessary. In late 2016, Ye' group, for the first time, proposed a Ni(OH)₂-gold catalyst for OER and showed good catalytic performance under 1 W of 532 nm laser.^[230] However, the study of plasmon-assisted electrocatalytic OER behaviours is still in its early stage, and few reports have come into view on the coupling effects and the working mechanism of high-performance OER catalysis.^[223,226,231–234] Almost all the works are focusing on the relationship of structure and performance without light promotion, especially on the preparation of catalysts with single-atom dispersions.^[159,235–238]

In this study, the gold decorated two-dimensional (2D) δ -MnO₂ nanosheet composites were successfully prepared with various percentage of gold loading. The composite showed excellent OER catalytic performance under and after green laser excitation. In this composite, δ -MnO₂ nanosheets were chosen as the primary OER catalysts for the multiple chemical states, the unique 2D structures and good electrochemical performance. Gold nanospheres (GNSs, 12.9 nm in diameter) were decorated on the 2D MnO₂ nanosheets as the nanoantennas and plasmonic exciters. Importantly, low power of 100 and 200 mW coherent 532 nm lasers were used to perform the experiments other than 1 W laser on previous research. The electrochemical results showed that the OER catalytic performance could be severely enhanced by activating the LSPR from GNSs under the 532 nm

laser irradiation. Interesting, after the laser treatment under dark environment, the composite showed a maintained OER catalytic performance with an overpotential of 0.32 V. Our study indicates that plasmon-induced hot-electron excitation could largely promote the confinement of the outer electrons within transition metal species. The plasmonic “hot holes” nearby may work as the effective electron trapper to form the active Mn^{n+} species which could provide active sites to extract electrons from OH^- and finally allow for high-efficiency electrochemical water oxidation at lower onset potential. These findings may provide insights on activation of plasmon-induced electrocatalysis under low power laser irradiation/treatment and the design of novel composite electrocatalysts.

6.2. Methods

SEM was conducted by a Zeiss-Supra55 microscope. HRTEM, SAED and EDX mapping images were recorded on a Tecnai G2 F30 S-TWIN microscope at an acceleration voltage of 300 kV. XRD patterns were examined on a Bruker D8 Advanced X-ray Diffractometer (Cu-K α radiation: $\lambda = 0.15406$ nm). A UV–visible spectrophotometer (Cary 5000, Varian Corp.) was used to measure the absorption spectra of the “as-prepared” samples. The chemical states were measured using an Axis Ultra X-XPS (Kratos Analytical Ltd., UK) equipped with a standard monochromatic Al-K α source ($h\nu = 1486.6$ eV). The surface potentials of the samples dispersed in a water/ethanol (1/1 volume ratio) solution were determined using the Zetasizer Nano ZS-90 system (DLS, Malvern Instruments,

England). EPR spectra were recorded on a Bruker A300 electron paramagnetic resonance spectrometer at room temperature.

All the electrochemical measurements were carried out in a three-electrode system *via* a CHI-760E instrument at room temperature. An Hg/HgO (filled with 1 M NaOH aqueous solution) and Pt wire were used as reference and counter electrode, respectively. The working electrode were made by drop-casting 5 μ L of sample dispersion (4 mg of catalyst dispersed in 1 mL of 2:1 v/v water/methanol mixed solution containing 60 μ L of 5 wt % Nafion) on a glassy carbon (GC, 3 mm diameter) electrode. Linear sweep voltammetry curves were measured at a sweep rate of 5 mV/s. The measured potentials of all the data were converted to the reversible hydrogen electrode (RHE) scale according to the Nernst equation ($E_{\text{RHE}} = E_{\text{Hg/HgO}} + 0.059 \times \text{pH} + 0.098$) scale, and the overpotential (η) at $j = 10 \text{ mA/cm}^2$ was determined using the following equation: $\eta = E_{\text{RHE}} - 1.23 \text{ V}$.

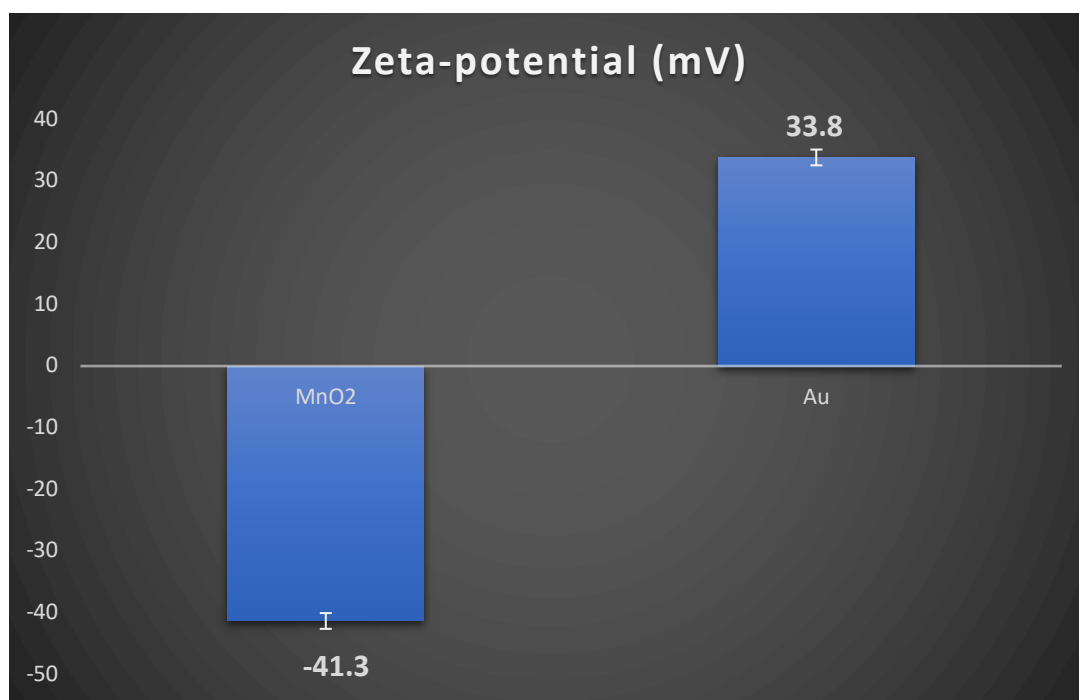


Figure 6.1 Zeta-potentials of MnO₂ nanosheets and gold nanoparticles well dispersed in water/ethanol (2:3 volume ratio) mixture.

6.3. Results and Discussion

GNSs with an average diameter of 12.9 nm were first prepared by reduction of HAuCl₄ with NaBH₄.^[110,167] Then, ultrathin δ -MnO₂ nanosheets were synthesized *via* a modified distillation reflux method.^[181] Based on the opposite surface charge of the MnO₂ nanosheets (ζ -potential = - 41.3 mV) and the GNSs (ζ -potential = 33.8 mV) on show in Figure 6.1, they could be physically assembled through the electrostatic interaction in the solution, which finally result in the formation of Au-MnO₂ nanocomposites. Figure 6.2a-c are the scanning electron microscopy (SEM) and transmission electron microscopy (TEM) images of the Au-MnO₂ nanosheet, respectively. It is clear that the GNSs were well dispersed

on the surface on MnO₂ nanosheets. The high-resolution TEM (HRTEM) image displayed in Figure 6.2d shows the lattice fringe between GNS and MnO₂ nanosheet and confirms the close interfacial contact which would support the “hot electron” transfer.^[239] The inset, in Figure 6.2e, shows the selected area electron diffraction (SAED) image of the GNS on MnO₂ nanosheet in Figure 5.2d, in which the diffraction rings correspond to the (111), (200) and (222) plane reflections of the face-centred cubic (fcc) gold nanosphere. Figure 6.2f shows the dark-field scanning transmission electron microscopy (STEM) image of a giant piece of Au-MnO₂ nanocomposite. The corresponding STEM-EDX elemental mapping are on shown in Figure 6.2g-j, from which the uniform distribution of GNSs over MnO₂ nanosheets is further confirmed.

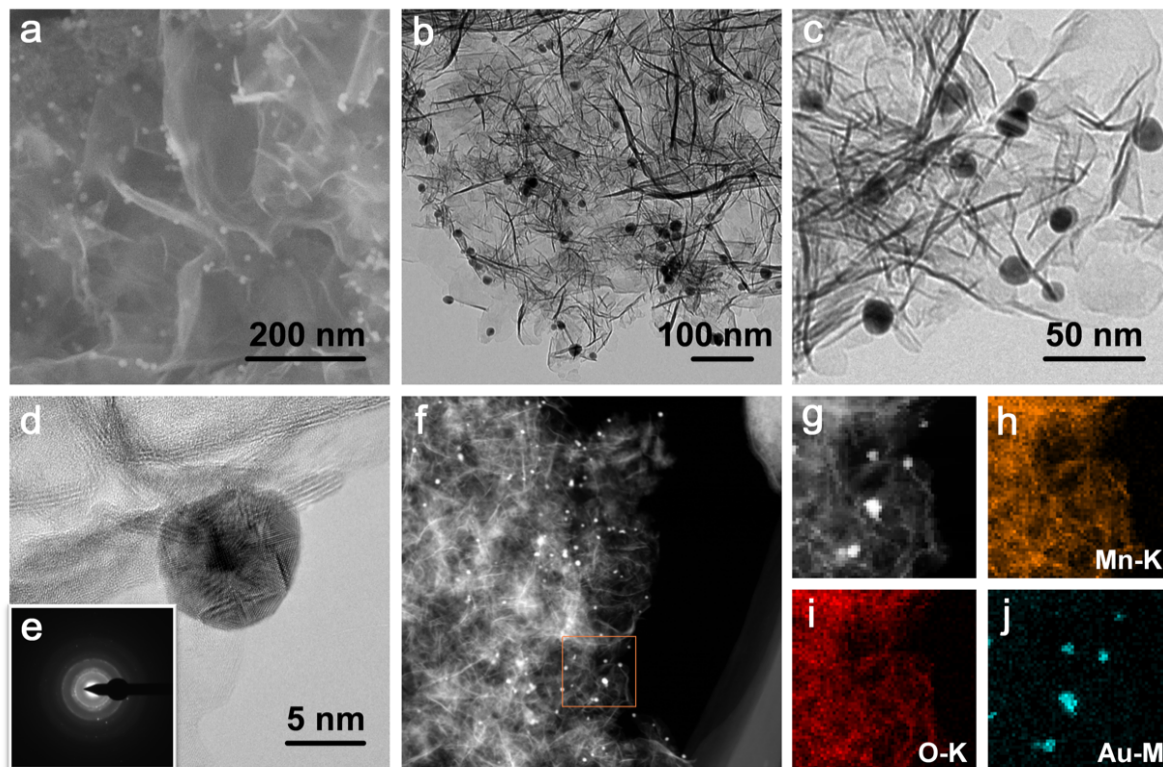


Figure 6.2 (a) SEM, (b, c) TEM and (d) high resolution TEM images of the Au-MnO₂ nanocomposites; the inset (e) shows the corresponding SAED pattern. (f) STEM image of the Au-MnO₂ nanocomposites; (g-j) STEM image and 2D element mapping images of Mn, O and Au in the area shown in (f), respectively.

Figure 6.3a shows the corresponding X-ray diffraction (XRD) pattern of Au-MnO₂ nanocomposites and bare MnO₂ nanosheets. Consistent with the SEM and TEM images, both the δ -MnO₂ (JCPDS 42-1317) and cubic gold (JCPDC 01-089-3697) are recognized. The peaks at 2-thetas of 12.2°, 24.5°, 37.1° and 66.2° reflects the (001), (002), (200) and (310) plane of δ -MnO₂ nanosheets, respectively; and the 37.5°, 44.9° and 77.9° reflects the (111), (200) and (220) plane of the fcc gold, which are also matched with the SAED pattern in Figure

6.2e.^[181] Importantly, the unusual intensity at 37.1° comparing to the standard may be caused by coating sample on a glass substrate for XRD measurement, which leads to the over exposure of (200) plane of δ -MnO₂ nanosheets. The absorption properties of GNSs, δ -MnO₂ nanosheets and Au-MnO₂ nanocomposites were investigated *via* a UV-vis spectrometer. After assembled the GNSs on δ -MnO₂ nanosheets, the extinction spectra of Au-MnO₂ nanocomposites exhibits an SP absorption peak at 525 nm, as shown in Figure 6.3b. In addition, with the increase of gold loading the plasmon absorption peak is getting stronger. Meanwhile, the peak wavelength of Au-MnO₂ nanocomposites is slightly red-shifted comparing to the pure GNSs (inset of Figure 6.3b), which indicates the electronic interaction between gold and MnO₂, and proves the successful assembly of Au-MnO₂ nanocomposites, eventually.^[223]

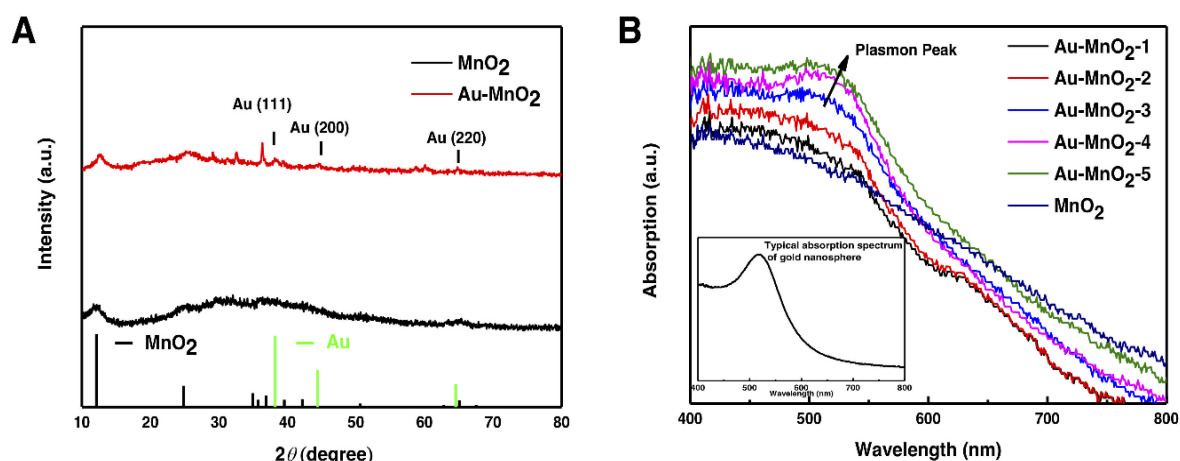


Figure 6.3 (a) XRD patterns of the MnO_2 nanosheets and Au-MnO_2 nanocomposites; (b) absorption spectra of MnO_2 nanosheets and Au-MnO_2 nanocomposites with various Au loading concentrations. The inset shows a typical surface plasmon peak of GNSs.

The standard and plasmon-promoted electrocatalytic performance of Au-MnO_2 nanocomposites towards oxygen evolution reaction were studied in O_2 -saturated 0.1 M KOH electrolyte at room temperature *via* a typical three-electrode system. Meanwhile, GNSs and $\delta\text{-MnO}_2$ nanosheets were also tested as references under identical conditions. 532 nm laser source was applied corresponding to maximum LSPR peak of GNSs. Figure 6.4a shows the OER polarization (linear sweep voltammetry, LSV) curves of $\delta\text{-MnO}_2$ nanosheets and Au-MnO_2 nanocomposites, with and without laser irradiation (100 and 200 mW of 532 nm green laser), at a scan rate of 5 mV/s. Without gold, the $\delta\text{-MnO}_2$ nanosheets exhibit much weaker OER electrocatalytic performance under dark and 100 mW

laser irradiation. Although the Au-MnO₂ nanocomposites do not show an obviously enhanced catalytic performance compared to δ -MnO₂ nanosheets in a dark environment, they show a much smaller overpotential at 0.38 and 0.32 V (vs reversible hydrogen electrode, RHE) once the surface plasmon resonance is excited by the 100 and 200 mW of 532 nm laser, respectively. In addition, Figure 6.4e shows the negligible OER catalytic performance of GNSs in the dark environment and under 532 nm laser irradiation. Meanwhile, to identify the wavelength dependence properties, a 200 mW of 650 nm laser was used to carry out the same experiment. As shown in Figure 6.5, Au-MnO₂ nanocomposite catalysts show a negligible current enhancement under the 650 nm laser irradiation, where this slightly change in current density may be caused by the broad band of plasmon peak and photothermal effect that could increase the reaction dynamics.^[25] These results clearly show that such an active photo-enhancement effect is mainly caused by the gold LSPR excitation.

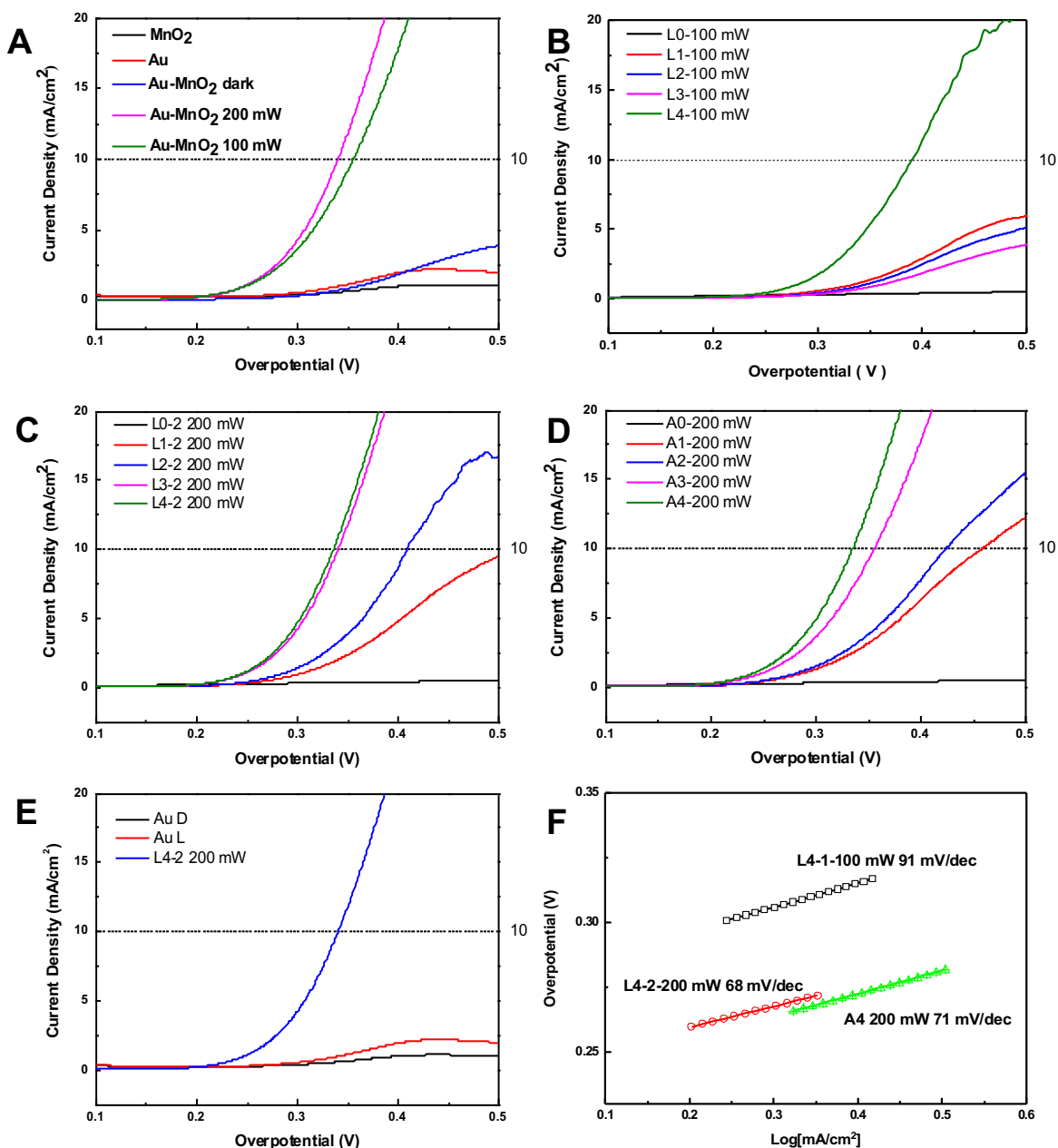


Figure 6.4 Electrochemical performance of the Au-MnO₂ nanocomposites in 0.1 M KOH electrolyte with and without 532 nm laser irradiation. (a-e) OER polarization curves at the scan rate of 5 mV/s of different samples under various conditions (dark, 100, 200 and after 200 mW laser treatment); (f) Tafel plots of the Au-MnO₂ catalysts under 100, 200 and after 200 mW laser treatment.

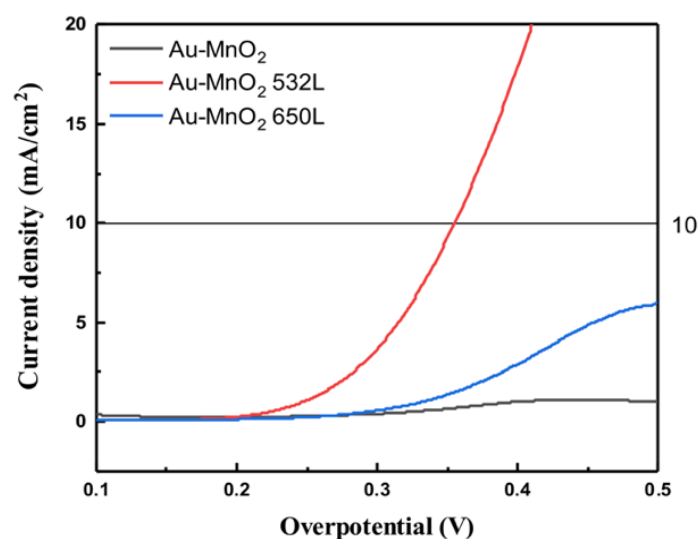


Figure 6.5 OER polarization curves at the scan rate of the 5 mV/s of Au-MnO₂ nanocomposite catalysts in 0.1 M KOH electrolyte under dark, 532 nm and 650 nm laser irradiation.

To further investigate this photo-enhancement effect, various amounts of gold loading were carried out. The loading concentration of gold is from 0 to 8.3 wt % and the obtained samples were denoted as L0-L4 and A0-A4, which were performed for the catalytic experiments under and after laser irradiation, respectively. It can be seen in Figure 6.4b that the electrocatalytic performance of the as-prepared samples under 100 mW laser irradiation is getting improved in order as the increase of GNSs loading, where the L4 (maximum gold loading) shows an OER overpotential at 0.38 V. Additionally, Figure 6.4c exhibits the LSV curves of the as-prepared samples under more intense 200 mW laser irradiation. Showing the similar performance trend as Figure 6.4b, the OER overpotential of L4 is further reduced to 0.32 V. This performance is much better

than that of Au-MnO₂ nanocomposites under the dark environment and comparable with IrO₂ and RuO₂ catalysts, which indicates that the efficient electrocatalytic OER reaction could be realized under light irradiation by grafting plasmonic antennas on conventional transition metal oxides. Interestingly, the samples maintained the OER catalytic performance after 5-min treatment of 200 mw laser irradiation. As shown in Figure 6.4d, the OER performance of 200 mW laser treated samples (A0-A4) show a similar trend of light promoted samples (L0-L4) and the overpotential of A4 is maintained at around 0.32 V, which is under the same level of L4 under 200 mW laser irradiation. Tafel slope analyses were also performed to analyse the kinetics of OER in this work, as shown in Figure 6.4f. With laser power increased from 100 to 200 mW, the Tafel slope is decreased from 91 to 68 mV/dec, which clearly indicates that the kinetics of oxygen evolution reaction are facilitated by LSPR excitation.^[230] Meanwhile, the Tafel slope of A4 is 71 mV/dec, close to that of L4 under 200 mW laser irradiation, proving the maintained OER performance after 5-min treatment of 200 mw laser irradiation.

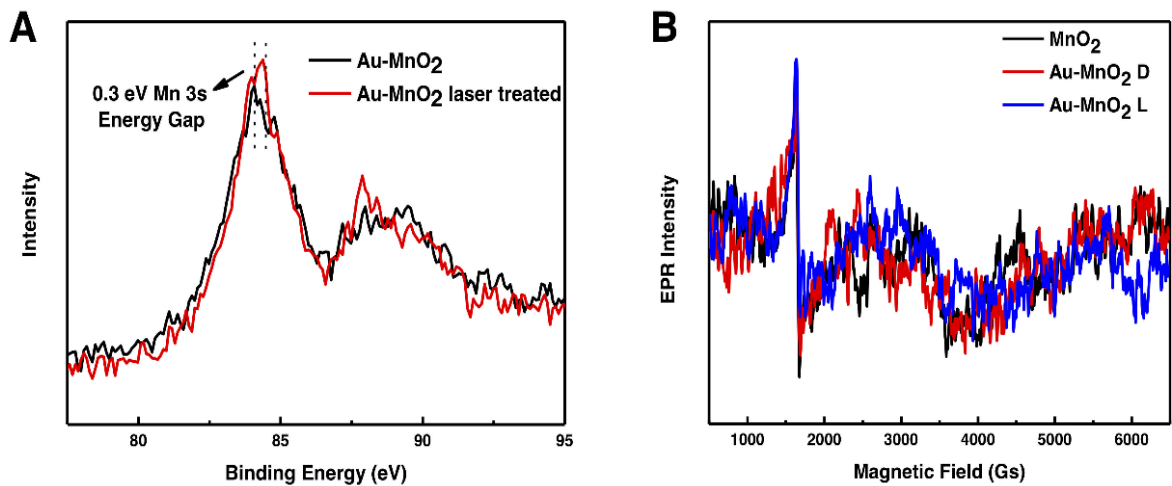


Figure 6.6 (a) High resolution Mn 3s XPS spectra of the Au-MnO₂ nanocomposites with and without 532 nm laser irradiation process. (b) Electron paramagnetic resonance (EPR) spectra of Au-MnO₂ nanocomposite in solution.

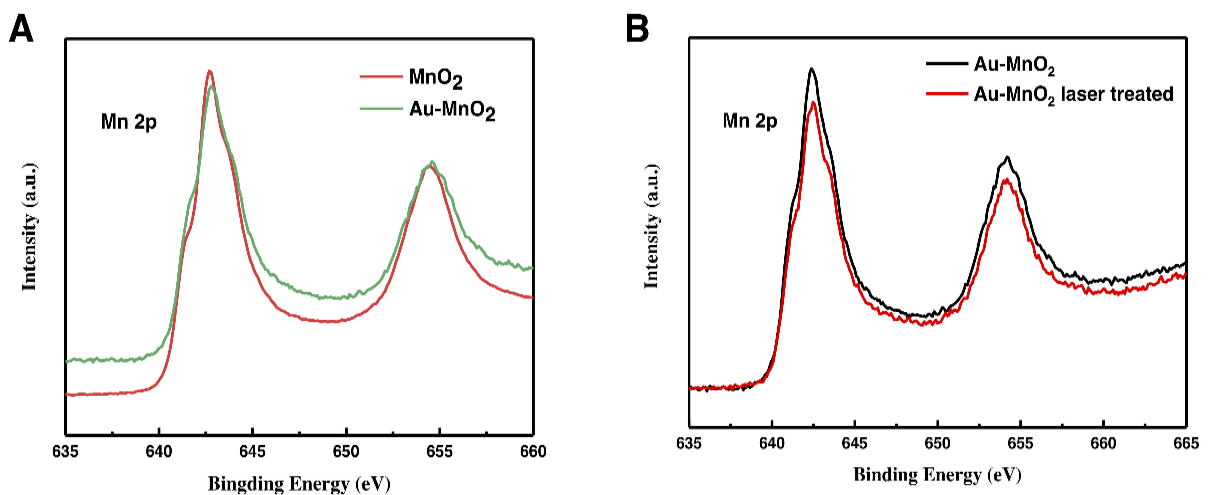


Figure 6.7 (a) High resolution Mn 2p XPS spectra of MnO₂ and Au-MnO₂. (b) High resolution Mn 2p XPS spectra of the Au-MnO₂ nanocomposites with/without 532 nm laser irradiation.

Figure 6.6a exhibits the X-ray photoelectron spectroscopy (XPS) spectra of Au-MnO₂ catalysts before and after laser irradiation, where an obvious energy gap exists. The electron binding energy of Mn 3s in Au-MnO₂ catalysts increases by 0.3 eV after 5-min exposure of 200 mW 532 nm laser irradiation, which is caused by the strong electronegativity of Au.^[230] Meanwhile, the electron binding energy spectra of Mn 2p were almost unaltered as shown in Figure 6.7. To further examine this plasmonic effects, electron paramagnetic resonance (EPR) spectra of Au-MnO₂ nanocomposites were measured with and without laser irradiation (200 mW, 532 nm). As reference, pure MnO₂ nanosheets were also tested. As shown in Figure 6.6b, loading of GNSs does not lead to any detectable difference of the EPR signals, whereas the induce of 532 nm laser to Au-MnO₂ nanocomposites causes an obvious signal alteration at 1582 Gs in comparison to the dark environment. These results clearly indicate the formation of active Mnⁿ⁺, in which the outer electrons are somehow confined by LSPR; and demonstrate that the generation of “hot holes” on gold surface by LSPR excitation is capable to confine the outer electrons of Mn cations and promotes the electron transfer from δ -MnO₂ to gold.

To elucidate the OER charge transfer process, electrochemical impedance spectroscopy (EIS) Nyquist plots of Au-MnO₂ hybrids measured with and without 532 nm laser irradiation was performed at 1.65 V (vs RHE), as shown in Figure 6.8a. All impedance spectra are fitted using an equivalent RC circuit

model, which consists of a resistor (R_s) and a charge transfer resistance (R_{ct}).^[240] R_s and R_{ct} represent the resistivity of the electrolyte between the working and reference electrodes and the charge transfer resistivity of Au-MnO₂ hybrids, respectively. The R_{ct} of Au-MnO₂ hybrids is 180 Ω under 200 mW 532 nm laser irradiation, which is much lower than that of the same sample under dark environment (275 Ω). This result also indicates that the plasmon excited “hot holes” would cause a higher charge transfer efficiency in the electrode and the catalysts under 532 nm laser irradiation is more kinetically favourable.

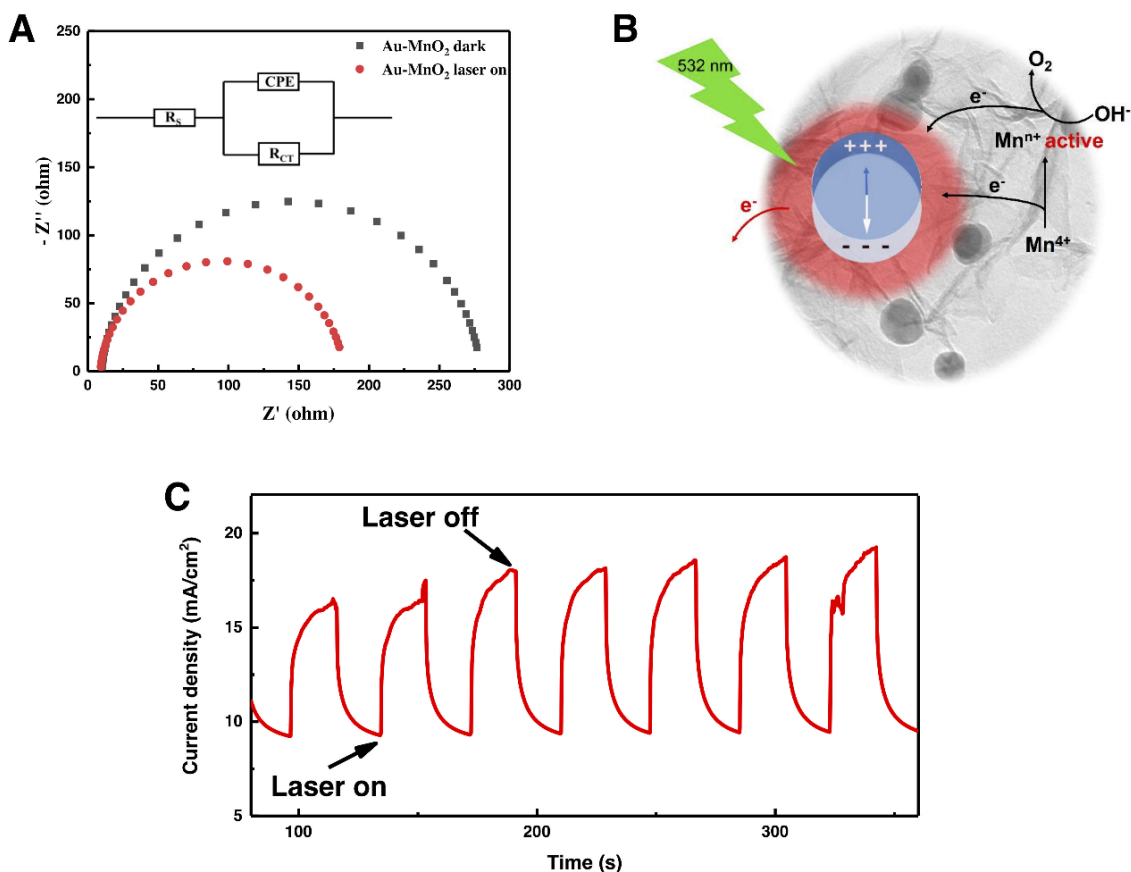


Figure 6.8 Electrochemical impedance spectroscopy (EIS) Nyquist plots of Au-MnO₂ hybrids measured with and without 532 nm laser irradiation. (b) Schematic electron transfer path that possibly occurs in the Au-MnO₂ nanocomposites under 532 nm laser irradiation. (c) Chronoamperometric I-t curve of Au-MnO₂ nanocomposite catalysts with 532 nm laser on and off.

Based on the aforementioned results, we propose the following possible mechanism to be responsible for the generation of active Mnⁿ⁺ species and subsequent improvement on OER catalysis over the Au-MnO₂ hybrid catalysts under 532 nm laser irradiation, as shown in Figure 6.8b. Under the 532 nm laser irradiation, plasmonic “hot holes” on the gold surface are generated as the

effective electron trapper to confine the outer electron of Mn^{4+} since the plasmonic “hot electrons” are transferred to the electrode with the assistance of an external voltage.^[225,241] Then, the formation of electron-confined active Mn^{n+} species would provide active sites to extract electrons from OH^- , facilitate the formation and the subsequent deprotonation of the key OOH intermediates and finally give rise to the O_2 evolution.^[52,59,60] And the strong local field and “hot holes” generated may also help the fast absorbance of OH^- to the active sites of the catalyst. In addition, Figure 6.8c exhibits the I-t curve of Au-MnO₂ nanocomposite catalysts with periodic laser (532 nm) on and off. It is obvious that removing laser irradiation would lead to an abrupt and remarkable suppression of O_2 evolution.

Surface plasmons can maintain for about 10 fs, at which time the electrons dephase. At 100 fs, electron-electron scattering occurs, producing hot electrons that couple to phonons after about 1 ps.^[13,220] The plasmon generated hot carries would rearrange in nanosecond level without irradiation. Obviously, the maintained OER catalytic performance (0.32 V overpotential) after laser treatment (A0-4 samples), as shown in Figure 6.4d, cannot be explained by the mechanism that we proposed. The maintained performance may be caused by the photothermal effects. Unlike the samples measured under laser irradiation in the liquid electrolyte, the direct laser treatment may lead to a large amount of heat that are not easily dissipated and confined to this $\sim 0.07 \text{ cm}^2$ area (electrode

surface area). Firstly, this large amount of heat may cause change on microstructure of the drop-cast sample film on glassy carbon electrode, where more active sites buried in the bulk film may be exposed. When measured in the three-electrode cell, more active sites may contact with the electrolyte, and eventually enhance the OER performance.^[47] Secondly, this photothermal effect may lead to a phase change of MnO₂, wherein exists a better catalytic performance.^[242,243] Finally, the localized heat may lead to the oxidation of Mn⁴⁺ to a higher state, which may also significantly enhance the OER performance.^[52,230]

6.4. Conclusions

In this work, we have successfully prepared gold decorated two-dimensional (2D) δ -MnO₂ nanosheets composites with various percentage of gold loading *via* a simple electrostatic method. The composites showed excellent OER catalytic performance under low power of 200 mW green laser irradiation. The electrochemical results showed that the OER catalytic performance could be severely enhanced by activating the LSPR from GNSs under 532 nm laser irradiation. By tuning the laser intensity from 100 to 200 mW, the overpotential was decreased from 0.38 to 0.32 V, which was comparable to IrO₂ and RuO₂ catalysts. Through the XPS and EPR results, our study indicates that plasmon-induced hot-electron excitation would work as the effective electron trapper to confine the outer electron of Mn⁴⁺ and lead to the formation of electron-confined

active Mn^{n+} species. The active Mn^{n+} species would provide active sites to extract electrons from OH^- , facilitate the formation and the subsequent deprotonation of the key OOH intermediates and finally allow for high efficiency oxygen evolution at lower onset potential. It is believed that our findings may provide insights on the activation of plasmon-promoted electrocatalysis under low power laser irradiation and the design of novel composite electrocatalysts.

7. Summary and Outlook

The works carried out in the thesis have helped to improve the understanding of energy transfer process based on plasmonic metal-dye system. Meanwhile, we have also extended the application of surface plasmon resonance effects to electrochemical catalysis to effectively improve the catalytic performance. As the major work in this project was the synthesis of new nanoparticle and nanosheet systems, various synthetic methods involved in this project were stated in Chapter 3, including synthesis of colloid gold nanoparticles and their surface modifications with silica and polymers as well as 2D MnO₂ nanosheets fabrication. In addition, the function of reaction reagents was also introduced as well as the development background of each synthetic method. Notably in this thesis, the factor weighting ϵ_m is 2 for spherical particles and $(1 - P_j)/P_j$ for prolate spheroids. Based on the Equation 1.14-1.17, the $(1 - P_j)/P_j$ could be much larger than 2 as the increase of aspect ratio. This would lead to the generation of longitudinal surface plasmon peak with increased sensitivity to the dielectric environment. Due to a decrease in the local permittivity introduced by the PS shell, the L mode shifts to shorter wavelengths (in Chapter 4); whereas the L mode shifts to longer wavelengths due to the increase in the local permittivity introduced by the silica shell (in Chapter 5).

Since theoretical design of SPASER first induced in 2003, the Chapter 4 studied the possible energy transfer process, from Rh 800 to GNRs, towards

SPASER realization through fluorescence lifetime technology. This energy transfer was enhanced when the surface plasmon overlapped with the absorption and emission of Rh 800. This energy transfer may compensate for the energy loss of surface plasmon and thus brings further insight towards creating a nanorod-based wavelength tuneable SPASER.

As a key technology for biosensing and bioimaging sciences, there has been a growing interest on metal enhanced fluorescence. In Chapter 5, the gold nanorods/silica spacer/large Stokes shift dye core-shell systems were presented to further study this issue. Through the spectroscopic results, the enhanced fluorescence intensities were contributed by both quantum yield enhancement and excitation rate enhancement.

Advanced materials in efficient harvesting, storage and utilization of renewable energy are of great importance in current energy research. In Chapter 6, with the introduction of the plasmonic effects by design of the Au-MnO₂ hybrid catalysts, surface plasmon could largely promote the confinement of the outer electrons of Mn cations by “hot holes” generated on gold surface. These “hot holes” worked as the effective electron trapper to form the active Mnⁿ⁺ species which could provide active sites to extract electrons from OH⁻ and eventually facilitate the electrochemical OER catalysis under low laser power. It is believed that these findings may provide insights on the activation of plasmon-promoted electrocatalysis under low power laser irradiation and the design of novel composite electrocatalysts.

Since the fluorescence enhance process has been investigated through the Mega 520 silica gold nanorods system, it is possible to apply this kind of nanoprobe to cells for background free high-resolution optical imaging, in the future. Meanwhile, a Mega 520 silica mini-GNRs system may be developed for the same application since smaller (less than 15 nm) nanoparticles could be excreted in the urine and stools, which would have potential for human medical detection. Furthermore, the silica-gold nanorods would also work as a platform to load proper dye molecules in the silica shell to further investigate the nanorods based wavelength tuneable SPASER.

In the meantime, plasmon-promoted electrochemical catalysis is another research field for further study. On the one hand, the account for the maintained OER catalytic performance after 200 mW 532 nm laser treatment is still unclear and needs further investigation. And we expect to report these findings shortly by additional XPS and EPR measurements. It is also possible and necessary to investigate the contribution of photothermal effect and charge transfer effect by a 10 - 20 nm silica shell to block the charge transfer. This would be good for understanding the mechanism of plasmon-promoted electrochemical catalysis. Moreover, this feature on OER may be extended to electrochemical CO₂ reduction and/or N₂ reduction reaction by plasmonic local heat and/or charge transfer effects.

Reference

- [1] K. M. Mayer, J. H. Hafner, *Chem. Rev.* **2011**, *111*, 3828.
- [2] A. Bouhelier, R. Bachelot, G. Lerondel, S. Kostcheev, P. Royer, G. P. Wiederrecht, *Phys. Rev. Lett.* **2005**, *95*, 267405.
- [3] D. Bergman, M. Stockman, *Phys. Rev. Lett.* **2003**, *90*, 1.
- [4] P. B. Johnson, R. W. Christy, *Phys. Rev. B* **1972**, *6*, 4370.
- [5] M. J. Kale, P. Christopher, *Science* **2015**, *349*, 587.
- [6] D. Huang, C. P. Byers, L. Wang, A. Hoggard, B. Hoener, S. Dominguez-Medina, S. Chen, W. Chang, C. F. Landes, S. Link, *ACS Nano* **2015**, *9*, 7072.
- [7] T. Ming, H. Chen, R. Jiang, Q. Li, J. Wang, *J. Phys. Chem. Lett.* **2012**, *3*, 191.
- [8] F. Nan, Y.-F. Zhang, X. Li, X.-T. Zhang, H. Li, X. Zhang, R. Jiang, J. Wang, W. Zhang, L. Zhou, J.-H. Wang, Q.-Q. Wang, Z. Zhang, *Nano Lett.* **2015**, *15*, 2705.
- [9] H. Chen, L. Shao, K. C. Woo, J. Wang, H. Q. Lin, *J. Phys. Chem. C* **2012**, *116*, 14088.
- [10] H. Chen, L. Shao, Q. Li, J. Wang, *Chem. Soc. Rev.* **2013**, *42*, 2679.
- [11] H. Chen, L. Shao, K. C. Woo, J. Wang, H.-Q. Lin, *J. Phys. Chem. C* **2012**,

- 116, 14088.
- [12] S. Yu, A. J. Wilson, G. Kumari, X. Zhang, P. K. Jain, *ACS Energy Lett.* **2017**, *2*, 2058.
- [13] K. A. Willets, R. P. Van Duyne, *Annu. Rev. Phys. Chem.* **2007**, *58*, 267.
- [14] S. E. Lohse, J. R. Eller, S. T. Sivapalan, M. R. Plews, C. J. Murphy, *ACS Nano* **2013**, *7*, 4135.
- [15] C. J. Orendorff, C. J. Murphy, *J. Phys. Chem. B* **2006**, *110*, 3990.
- [16] M. Liu, P. Guyot-Sionnest, *J. Phys. Chem. B* **2005**, *109*, 22192.
- [17] S. Link, M. A. El-Sayed, *J. Phys. Chem. B* **1999**, *103*, 8410.
- [18] N. Omura, *Anal. Sci.* **2009**, *25*, 255.
- [19] J. Perez-juste, I. Pastoriza-Santos, L. M. Liz-marzan, P. Mulvaney, *Coord. Chem. Rev.* **2005**, *249*, 1870.
- [20] B. Nikoobakht, M. A. El-Sayed, *Chem. Mater.* **2003**, *15*, 1957.
- [21] S. Patibandla, Y. Zhang, A. M. Tohari, P. Gu, J. Reilly, Y. Chen, X. Shu, *J. Appl. Toxicol.* **2018**, *38*, 1153.
- [22] X. Meng, A. V Kildishev, K. Fujita, K. Tanaka, V. M. Shalaev, *Nano Lett.* **2013**, *13*, 4106.
- [23] G. Mie, *Ann. Phys.* **1908**, *330*, 377.

- [24] Y. Zhang, Y. Chen, In *Pasmons: Structure, Properties and Applications*; Nova, 2011.
- [25] W.-S. Chang, B. Willingham, L. S. Slaughter, S. Dominguez-Medina, P. Swanglap, S. Link, *Acc. Chem. Res.* **2012**, *45*, 1936.
- [26] T. Wriedt, *The Mie Theory*; Hergert, W.; Wriedt, T., Eds.; Springer Series in Optical Sciences; Springer: Berlin, Heidelberg, 2012; Vol. 169.
- [27] C. F. Bohren, D. R. Huffman, *Absorption and Scattering of Light by Small Particles*; Wiley, 1998.
- [28] L. J. E. Anderson, K. M. Mayer, R. D. Fraleigh, Y. Yang, S. Lee, J. H. Hafner, *J. Phys. Chem. C* **2010**, *114*, 11127.
- [29] B. Yan, Y. Wang, *J. Phys. Chem. B* **2003**, *107*, 9159.
- [30] J.-F. Li, S.-Y. Ding, Z.-L. Yang, M.-L. Bai, J. R. Anema, X. Wang, A. Wang, D.-Y. Wu, B. Ren, S.-M. Hou, T. Wandlowski, Z.-Q. Tian, *J. Am. Chem. Soc.* **2011**, *133*, 15922.
- [31] S.-Y. Liu, J. Li, F. Zhou, L. Gan, Z.-Y. Li, *Opt. Lett.* **2011**, *36*, 1296.
- [32] E. M. Goldys, M. A. Sobhan, *Adv. Funct. Mater.* **2012**, *22*, 1906.
- [33] Y. Fang, W.-S. Chang, B. Willingham, P. Swanglap, S. Dominguez-Medina, S. Link, *ACS Nano* **2012**, *6*, 7177.
- [34] M. Yorulmaz, S. Khatua, P. Zijlstra, A. Gaiduk, M. Orrit, *Nano Lett.*

- 2012**, *12*, 4385.
- [35] J. Huang, W. Wang, C. J. Murphy, D. G. Cahill, *Proc. Natl. Acad. Sci.* **2014**, *111*, 906.
- [36] A. Mooradian, *Phys. Rev. Lett.* **1969**, *22*, 185.
- [37] Y. Zhang, S. He, W. Guo, Y. Hu, J. Huang, J. R. Mulcahy, W. D. Wei, *Chem. Rev.* **2018**, *118*, 2927.
- [38] E. Dulkeith, T. Niedereichholz, T. Klar, J. Feldmann, G. von Plessen, D. Gittins, K. Mayya, F. Caruso, *Phys. Rev. B* **2004**, *70*, 205424.
- [39] M. Tahir, L. Pan, F. Idrees, X. Zhang, L. Wang, J.-J. Zou, Z. L. Wang, *Nano Energy* **2017**, *37*, 136.
- [40] E. Yoo, H. Zhou, *ACS Nano* **2011**, *5*, 3020.
- [41] M. Prabu, P. Ramakrishnan, H. Nara, T. Momma, T. Osaka, S. Shanmugam, *ACS Appl. Mater. Interfaces* **2014**, *6*, 16545.
- [42] S. Yang, D. J. Siegel, *Chem. Mater.* **2015**, *27*, 3852.
- [43] J.-S. Lee, S. Tai Kim, R. Cao, N. Choi, M. Liu, K. T. Lee, J. Cho, *Adv. Energy Mater.* **2011**, *1*, 34.
- [44] J. Fu, Z. P. Cano, M. G. Park, A. Yu, M. Fowler, Z. Chen, *Adv. Mater.* **2017**, *29*, 1604685.
- [45] F. Cheng, J. Chen, *Chem. Soc. Rev.* **2012**, *41*, 2172.

- [46] Z. Wang, D. Xu, J. Xu, X. Zhang, *Chem. Soc. Rev.* **2014**, *43*, 7746.
- [47] S. Anantharaj, S. R. Ede, K. Karthick, S. Sam Sankar, K. Sangeetha, P. E. Karthik, S. Kundu, *Energy Environ. Sci.* **2018**, *11*, 744.
- [48] F. Song, K. Schenk, X. Hu, *Energy Environ. Sci.* **2016**, *9*, 473.
- [49] X. Liu, W. Liu, M. Ko, M. Park, M. G. Kim, P. Oh, S. Chae, S. Park, A. Casimir, G. Wu, J. Cho, *Adv. Funct. Mater.* **2015**, *25*, 5799.
- [50] H. Jin, J. Wang, D. Su, Z. Wei, Z. Pang, Y. Wang, *J. Am. Chem. Soc.* **2015**, *137*, 2688.
- [51] Z. Wu, S. Yang, Y. Sun, K. Parvez, X. Feng, K. Müllen, *J. Am. Chem. Soc.* **2012**, *134*, 9082.
- [52] H. Osgood, S. V. Devaguptapu, H. Xu, J. Cho, G. Wu, *Nano Today* **2016**, *11*, 601.
- [53] J. O. Bockris, T. Otagawa, *J. Phys. Chem.* **1983**, *87*, 2960.
- [54] J. O. Bockris, *J. Chem. Phys.* **1956**, *24*, 817.
- [55] J. O. Bockris, *J. Electrochem. Soc.* **1984**, *131*, 290.
- [56] S. Anantharaj, S. R. Ede, K. Sakthikumar, K. Karthick, S. Mishra, S. Kundu, *ACS Catal.* **2016**, *6*, 8069.
- [57] S. Anantharaj, P. E. Karthik, S. Kundu, *Catal. Sci. Technol.* **2017**, *7*, 882.
- [58] B. S. Yeo, A. T. Bell, *J. Am. Chem. Soc.* **2011**, *133*, 5587.

- [59] M. S. Burke, M. G. Kast, L. Trotochaud, A. M. Smith, S. W. Boettcher, *J. Am. Chem. Soc.* **2015**, *137*, 3638.
- [60] L. Trotochaud, S. L. Young, J. K. Ranney, S. W. Boettcher, *J. Am. Chem. Soc.* **2014**, *136*, 6744.
- [61] C. Tang, H.-S. Wang, H.-F. Wang, Q. Zhang, G.-L. Tian, J.-Q. Nie, F. Wei, *Adv. Mater.* **2015**, *27*, 4516.
- [62] J. Zhang, J. Liu, L. Xi, Y. Yu, N. Chen, S. Sun, W. Wang, K. M. Lange, B. Zhang, *J. Am. Chem. Soc.* **2018**, *140*, 3876.
- [63] D. Su, S. Dou, G. Wang, *NPG Asia Mater.* **2015**, *7*, e155.
- [64] D. A. Macinnes, L. Adler, *Proc. Natl. Acad. Sci.* **1919**, *5*, 160.
- [65] Y. Cai, A. B. Anderson, *J. Phys. Chem. B* **2004**, *108*, 9829.
- [66] Alley J. Bard; Larry R. Faulkner, *Electrochemical Methods: Fundamentals and Applications*; 2nd ed.; John Wiley & Sons Inc., 2001.
- [67] Z. Guo, C. Li, W. Li, H. Guo, X. Su, P. He, Y. Wang, Y.-Y. Xia, *J. Mater. Chem. A* **2016**, *4*, 6282.
- [68] S. Xie, K. Cammann, *J. Electroanal. Chem.* **1987**, *229*, 249.
- [69] R. Frydendal, Improving performance of catalysts for water electrolysis : The MnOx case, Technical University of Denmark, 2015.
- [70] M. Gumustas, C. T. Sengel-Turk, A. Gumustas, S. A. Ozkan, B. Uslu, In

Multifunctional Systems for Combined Delivery, Biosensing and Diagnostics; Elsevier, 2017.

- [71] A. Baelo, R. Levato, E. Julián, A. Crespo, J. Astola, J. Gavaldà, E. Engel, M. A. Mateos-Timoneda, E. Torrents, *J. Control. Release* **2015**, *209*, 150.
- [72] S. T. Sivapalan, B. M. DeVetter, T. K. Yang, M. V. Schulmerich, R. Bhargava, C. J. Murphy, *J. Phys. Chem. C* **2013**, *117*, 10677.
- [73] N. Gandra, C. Portz, L. Tian, R. Tang, B. Xu, S. Achilefu, S. Singamaneni, *Angew. Chemie - Int. Ed.* **2014**, *53*, 866.
- [74] B. A. Russell, Protein Encapsulated Gold Nanoclusters for Biological Applications, University of Strathclyde, 2017.
- [75] J. R. Lakowicz, *Principles of Fluorescence Spectroscopy*; 3rd ed.; Springer, 2006.
- [76] R. Bardhan, N. K. Grady, J. R. Cole, A. Joshi, N. J. Halas, *ACS Nano* **2009**, *3*, 744.
- [77] D. J. S. Birch, Y. Chen, O. J. Rolinski, In *Biological and Medical Photonics, Spectroscopy and Microscopy*; Wiley, 2015.
- [78] P. Bharadwaj, L. Novotny, *Opt. Express* **2007**, *15*, 14266.
- [79] Y. Zhang, Study on Gold Nanoparticles for Biological Applications, University of Strathclyde, 2013.

- [80] J. R. Albani, *Principles and Applications of Fluorescence Spectroscopy*; Blackwell Publishing, 2007.
- [81] M. Martini, M. Montagna, M. Ou, O. Tillement, S. Roux, P. Perriat, *J. Appl. Phys.* **2009**, *106*, 094304.
- [82] M. Kamata, M. Paku, *J. Chem. Educ.* **2007**, *84*, 674.
- [83] M. Royzen, Z. Dai, J. W. Canary, *J. Am. Chem. Soc.* **2005**, *127*, 1612.
- [84] E. Dulkeith, A. Morteani, T. Niedereichholz, T. Klar, J. Feldmann, S. Levi, F. van Veggel, D. Reinhoudt, M. Möller, D. Gittins, *Phys. Rev. Lett.* **2002**, *89*, 12.
- [85] J. R. Lakowicz, G. Weber, *Biochemistry* **1973**, *12*, 4171.
- [86] C. Fan, S. Wang, J. W. Hong, G. C. Bazan, K. W. Plaxco, A. J. Heeger, *Proc. Natl. Acad. Sci.* **2003**, *100*, 6297.
- [87] J. R. Lakowicz, G. Weber, *Biochemistry* **1973**, *12*, 4161.
- [88] T. Ren, W. Erker, T. Basché, W. Schärfl, *Langmuir* **2010**, *26*, 17981.
- [89] S. A. Hussain, *arXiv Prepr. arXiv0908.1815* **2009**.
- [90] A. Margineanu, J. J. Chan, D. J. Kelly, S. C. Warren, D. Flatters, S. Kumar, M. Katan, C. W. Dunsby, P. M. W. French, *Sci. Rep.* **2016**, *6*, 28186.
- [91] Q.-H. Xu, S. Wang, D. Korystov, A. Mikhailovsky, G. C. Bazan, D.

- Moses, A. J. Heeger, *Proc. Natl. Acad. Sci.* **2005**, *102*, 530.
- [92] C. S. Yun, A. Javier, T. Jennings, M. Fisher, S. Hira, S. Peterson, B. Hopkins, N. O. Reich, G. F. Strouse, *J. Am. Chem. Soc.* **2005**, *127*, 3115.
- [93] R. B. Sekar, A. Periasamy, *J. Cell Biol.* **2003**, *160*, 629.
- [94] G. Wei, J. Yu, J. Wang, P. Gu, D. J. S. Birch, Y. Chen, *J. Biomed. Opt.* **2016**, *21*, 097001.
- [95] Y. Zhang, G. Wei, J. Yu, D. J. S. Birch, Y. Chen, *Faraday Discuss.* **2015**, *178*, 383.
- [96] T. L. Jennings, J. C. Schlatterer, M. P. Singh, N. L. Greenbaum, G. F. Strouse, *Nano Lett.* **2006**, *6*, 1318.
- [97] R. A. Riskowski, R. E. Armstrong, N. L. Greenbaum, G. F. Strouse, *ACS Nano* **2016**, *10*, 1926.
- [98] Y. Zhang, D. J. S. Birch, Y. Chen, *Appl. Phys. Lett.* **2011**, *99*, 103701.
- [99] C. J. Breshike, R. a. Riskowski, G. F. Strouse, *J. Phys. Chem. C* **2013**, *117*, 23942.
- [100] R. E. Armstrong, R. A. Riskowski, G. F. Strouse, *Photochem. Photobiol.* **2015**, *91*, 732.
- [101] C. Racknor, M. R. Singh, Y. Zhang, D. J. S. Birch, Y. Chen, *Methods Appl. Fluoresc.* **2013**, *2*, 015002.

- [102] P. Ghenuche, J. De Torres, S. B. Moparthi, V. Grigoriev, J. Wenger, *Nano Lett.* **2014**, *14*, 4707.
- [103] H. Li, H. Hu, D. Xu, *Anal. Chem.* **2015**, *87*, 3826.
- [104] M. L.-Viger, D. Brouard, D. Boudreau, *J. Phys. Chem. C* **2011**, *115*, 2974.
- [105] J. Zhang, Y. Fu, M. H. Chowdhury, J. R. Lakowicz, *J. Phys. Chem. C* **2007**, *111*, 11784.
- [106] J. Zhang, J. R. Lakowicz, *Opt. Express* **2007**, *15*, 2598.
- [107] R. Chikkaraddy, B. de Nijs, F. Benz, S. J. Barrow, O. A. Scherman, E. Rosta, A. Demetriadou, P. Fox, O. Hess, J. J. Baumberg, *Nature* **2016**, *535*, 127.
- [108] J. R. Lakowicz, *Anal. Biochem.* **2005**, *337*, 171.
- [109] A. I. Dragan, C. D. Geddes, *Phys. Chem. Chem. Phys.* **2011**, *13*, 3831.
- [110] P. Gu, D. J. S. Birch, Y. Chen, *Methods Appl. Fluoresc.* **2014**, *2*, 024004.
- [111] M. Bauch, K. Toma, M. Toma, Q. Zhang, J. Dostalek, *Plasmonics* **2014**, *9*, 781.
- [112] C. D. Geddes, *Metal-Enhanced Fluorescence*; Wiley, 2010.
- [113] R. Bardhan, N. K. Grady, N. J. Halas, *Small* **2008**, *4*, 1716.
- [114] S. Khatua, P. M. R. Paulo, H. Yuan, A. Gupta, P. Zijlstra, M. Orrit, *ACS*

- Nano* **2014**, *8*, 4440.
- [115] M. S. Tame, K. R. McEnery, Ş. K. Özdemir, J. Lee, S. A. Maier, M. S. Kim, *Nat. Phys.* **2013**, *9*, 329.
- [116] Y. Luo, E. D. Ahmadi, K. Shayan, Y. Ma, K. S. Mistry, C. Zhang, J. Hone, J. L. Blackburn, S. Strauf, *Nat. Commun.* **2017**, *8*, 1413.
- [117] J. Li, A. V. Krasavin, L. Webster, P. Segovia, A. V. Zayats, D. Richards, *Sci. Rep.* **2016**, *5*, 1.
- [118] Y. Jeong, Y.-M. Kook, K. Lee, W.-G. Koh, *Biosens. Bioelectron.* **2018**, *111*, 102.
- [119] J.-F. Li, C.-Y. Li, R. F. Aroca, *Chem. Soc. Rev.* **2017**, *46*, 3962.
- [120] A. V. Thorat, T. Ghoshal, L. Chen, J. D. Holmes, M. A. Morris, *J. Colloid Interface Sci.* **2017**, *490*, 294.
- [121] D. Byrne, P. Duggan, C. McDonagh, *Methods Appl. Fluoresc.* **2017**, *5*, 015004.
- [122] H. Sugimoto, S. Yashima, K. Furuta, A. Inoue, M. Fujii, *Appl. Phys. Lett.* **2016**, *108*, 241103.
- [123] K. Ray, J. R. Lakowicz, *J. Phys. Chem. C* **2013**, *117*, 15790.
- [124] J. R. Lakowicz, *Anal. Biochem.* **2001**, *298*, 1.
- [125] T. Liebermann, W. Knoll, *Colloids Surfaces A Physicochem. Eng. Asp.*

2000, *171*, 115.

- [126] Y. Zhang, J. Yu, D. J. S. Birch, Y. Chen, *J. Biomed. Opt.* **2010**, *15*, 20504.
- [127] M. Wang, G. Hartmann, Z. Wu, L. Scarabelli, B. B. Rajeeva, J. W. Jarrett, E. P. Perillo, A. K. Dunn, L. M. Liz-Marzán, G. S. Hwang, Y. Zheng, *Small* **2017**, *13*, 1.
- [128] P. Zijlstra, M. Orrit, *Reports Prog. Phys.* **2011**, *74*, 106401.
- [129] W. Becker, *FLIM Systems for Laser Scanning Microscopes*; 3rd ed.; Becker & Hickl GmbH, 2013.
- [130] R. Esposito, G. Mensitieri, S. De Nicola, *Analyst* **2015**, *140*, 8138.
- [131] J. M. Shaver, L. B. McGown, *Anal. Chem.* **1996**, *68*, 9.
- [132] N. I. Zheludev, S. L. Prosvirnin, N. Papisimakis, V. A. Fedotov, *Nat. Photonics* **2008**, *2*, 351.
- [133] J. Pendry, S. Maier, *Phys. Rev. Lett.* **2011**, *107*, 259703.
- [134] M. I. Stockman, *Nat. Photonics* **2008**, *2*, 327.
- [135] M. I. Stockman, *Phys. Today* **2011**, 39.
- [136] H. Zhang, J. Zhou, W. Zou, M. He, *J. Appl. Phys.* **2012**, *112*, 074309.
- [137] H. Z. Chen, J. Q. Hu, S. Wang, B. Li, X. Y. Wang, Y. L. Wang, L. Dai, R. M. Ma, *Sci. Adv.* **2017**, *3*, 1.

- [138] N. Passarelli, R. A. Bustos-Marún, E. A. Coronado, *J. Phys. Chem. C* **2016**, *120*, 24941.
- [139] E. I. Galanzha, R. Weingold, D. A. Nedosekin, M. Sarimollaoglu, J. Nolan, W. Harrington, A. S. Kuchyanov, R. G. Parkhomenko, F. Watanabe, Z. Nima, A. S. Biris, A. I. Plekhanov, M. I. Stockman, V. P. Zharov, *Nat. Commun.* **2017**, *8*, 1.
- [140] V. J. Sorger, X. Zhang, *Science* **2011**, *333*, 709.
- [141] W.-S. Chang, B. A. Willingham, L. S. Slaughter, B. P. Khanal, L. Vigderman, E. R. Zubarev, S. Link, *Proc. Natl. Acad. Sci.* **2011**, *108*, 19879.
- [142] J. Seidel, S. Grafström, L. Eng, *Phys. Rev. Lett.* **2005**, *94*, 1.
- [143] M. A. Noginov, G. Zhu, A. M. Belgrave, R. Bakker, V. M. Shalaev, E. E. Narimanov, S. Stout, E. Herz, T. Suteewong, U. Wiesner, *Nature* **2009**, *460*, 1110.
- [144] R. A. Flynn, C. S. Kim, I. Vurgaftman, M. Kim, J. R. Meyer, a J. Mäkinen, K. Bussmann, L. Cheng, F.-S. Choa, J. P. Long, *Opt. Express* **2011**, *19*, 8954.
- [145] M. I. Stockman, *J. Opt.* **2010**, *12*, 24004.
- [146] Y. Y. Huo, T. Q. Jia, Y. Zhang, H. Zhao, S. a. Zhang, D. H. Feng, Z. R. Sun, *Appl. Phys. Lett.* **2014**, *104*, 2013.

- [147] K. G. Stamplecoskie, M. Grenier, J. C. Scaiano, *J. Am. Chem. Soc.* **2014**, *136*, 2956.
- [148] A. Yang, T. B. Hoang, M. Dridi, C. Deeb, M. H. Mikkelsen, G. C. Schatz, T. W. Odom, *Nat. Commun.* **2015**, *6*, 6939.
- [149] S. J. Smith, E. M. Purcell, *Phys. Rev.* **1953**, *92*, 1069.
- [150] B. Romeira, A. Fiore, *IEEE J. Quantum Electron.* **2018**, *54*, 1.
- [151] N. R. Jana, L. Gearheart, C. J. Murphy, *Chem. Commun.* **2001**, 617.
- [152] N. R. Jana, L. Gearheart, C. J. Murphy, *J. Phys. Chem. B* **2001**, *105*, 4065.
- [153] N. R. Jana, L. Gearheart, C. J. Murphy, *Adv. Mater.* **2001**, *13*, 1389.
- [154] B. Nikoobakht, M. A. El-Sayed, *Langmuir* **2001**, *17*, 6368.
- [155] Z.-Y. Li, Y. Xia, *Nano Lett.* **2010**, *10*, 243.
- [156] A. Liu, G. Wang, F. Wang, Y. Zhang, *Coord. Chem. Rev.* **2017**, *336*, 28.
- [157] N. G. Bastús, J. Comenge, V. Puentes, *Langmuir* **2011**, *27*, 11098.
- [158] A. J. Mannix, B. Kiraly, M. C. Hersam, N. P. Guisinger, *Nat. Rev. Chem.* **2017**, *1*, 0014.
- [159] F. Yi, H. Ren, K. Dai, X. Wang, Y. Han, K. Wang, K. Li, B. Guan, J. Wang, M. Tang, J. Shan, H. Yang, M. Zheng, Z. You, D. Wei, Z. Liu, *Energy Environ. Sci.* **2018**, *11*, 2016.

- [160] E. Y. Kataev, D. M. Itkis, A. V. Fedorov, B. V. Senkovsky, D. Y. Usachov, N. I. Verbitskiy, A. Grüneis, A. Barinov, D. Y. Tsukanova, A. A. Volykhov, K. V. Mironovich, V. A. Krivchenko, M. G. Rybin, E. D. Obraztsova, C. Laubschat, D. V. Vyalikh, L. V. Yashina, *ACS Nano* **2015**, *9*, 320.
- [161] H. Sugimoto, T. Chen, R. Wang, M. Fujii, B. M. Reinhard, L. Dal Negro, *ACS Photonics* **2015**, *2*, 1298.
- [162] A. De Luca, M. P. Grzelczak, I. Pastoriza-Santos, L. M. Liz-Marzán, M. La Deda, M. Striccoli, G. Strangi, *ACS Nano* **2011**, *5*, 5823.
- [163] J. Turkevich, P. C. Stevenson, J. Hillier, *Discuss. Faraday Soc.* **1951**, *11*, 55.
- [164] G. Frens, *Nat. Phys. Sci.* **1973**, *241*, 20.
- [165] W. Cheng, S. Dong, E. Wang, *Langmuir* **2003**, *19*, 9434.
- [166] N. R. Jana, L. Gearheart, C. J. Murphy, *Langmuir* **2001**, *17*, 6782.
- [167] D. K. Smith, B. A. Korgel, *Langmuir* **2008**, *24*, 644.
- [168] C. J. Murphy, L. B. Thompson, A. M. Alkilany, P. N. Sisco, S. P. Boulos, S. T. Sivapalan, J. A. Yang, D. J. Chernak, J. Huang, *J. Phys. Chem. Lett.* **2010**, *1*, 2867.
- [169] L. Vigderman, B. P. Khanal, E. R. Zubarev, *Adv. Mater.* **2012**, *24*, 4811.

- [170] A. Gole, C. J. Murphy, *Chem. Mater.* **2004**, *16*, 3633.
- [171] S. E. Lohse, C. J. Murphy, *Chem. Mater.* **2013**, *25*, 1250.
- [172] O. G. Tovmachenko, C. Graf, D. J. van den Heuvel, A. van Blaaderen, H. C. Gerritsen, *Adv. Mater.* **2006**, *18*, 91.
- [173] W. Stober, *J. Colloid Interface Sci.* **1968**, *26*, 62.
- [174] I. Pastoriza-Santos, J. Pérez-Juste, L. M. Liz-Marzán, *Chem. Mater.* **2006**, *18*, 2465.
- [175] R. I. Nooney, D. Thirunavukkarasu, Y. Chen, R. Josephs, A. E. Ostafin, *Langmuir* **2003**, *19*, 7628.
- [176] I. Gorelikov, N. Matsuura, *Nano Lett.* **2008**, *8*, 369.
- [177] N. S. Abadeer, M. R. Brennan, W. L. Wilson, C. J. Murphy, *ACS Nano* **2014**, 8392.
- [178] S. O. Obare, N. R. Jana, C. J. Murphy, *Nano Lett.* **2001**, *1*, 601.
- [179] S. Pargen, C. Willems, H. Keul, A. Pich, M. Möller, *Macromolecules* **2012**, *45*, 1230.
- [180] A. Ravve, *Principles of Polymer Chemistry*; Springer New York: New York, NY, 2012.
- [181] X. Fan, D. Yang, L. Ding, J. Du, C. Tao, *ChemPhysChem* **2015**, *16*, 176.
- [182] Y. Meng, W. Song, H. Huang, Z. Ren, S. Chen, S. L. Suib, *J. Am. Chem.*

- Soc.* **2014**, *136*, 11452.
- [183] F. Cheng, Y. Su, J. Liang, Z. Tao, J. Chen, *Chem. Mater.* **2010**, *22*, 898.
- [184] F. F. Marafatto, M. L. Strader, J. Gonzalez-Holguera, A. Schwartzberg, B. Gilbert, J. Peña, *Proc. Natl. Acad. Sci.* **2015**, *112*, 4600.
- [185] Z. Liu, K. Xu, H. Sun, S. Yin, *Small* **2015**, *11*, 2182.
- [186] Y. Huang, Y. Lin, W. Li, *Electrochim. Acta* **2013**, *99*, 161.
- [187] A. K. Sinha, M. Pradhan, T. Pal, *J. Phys. Chem. C* **2013**, *117*, 23976.
- [188] D. Cochin, A. Laschewsky, F. Nallet, *Macromolecules* **1997**, 9297, 2278.
- [189] T. L. Jennings, M. P. Singh, G. F. Strouse, *J. Am. Chem. Soc.* **2006**, *128*, 5462.
- [190] P. K. Jain, M. A. El-Sayed, *Chem. Phys. Lett.* **2010**, *487*, 153.
- [191] C. Burda, X. Chen, R. Narayanan, M. A. El-Sayed, *Chem. Rev.* **2005**, *105*, 1025.
- [192] J. D. Xiao, L. Han, J. Luo, S. H. Yu, H. L. Jiang, *Angew. Chemie - Int. Ed.* **2018**, *57*, 1103.
- [193] M. D. Brown, T. Suteewong, R. S. S. Kumar, V. D'Innocenzo, A. Petrozza, M. M. Lee, U. Wiesner, H. J. Snaith, *Nano Lett.* **2011**, *11*, 438.
- [194] N. S. Abadeer, C. J. Murphy, *J. Phys. Chem. C* **2016**, *120*, 4691.

- [195] P. Anger, P. Bharadwaj, L. Novotny, *Phys. Rev. Lett.* **2006**, *96*, 3.
- [196] M. H. Tahersima, M. D. Birowosuto, Z. Ma, W. C. Coley, M. D. Valentin, S. Naghibi Alvillar, I. H. Lu, Y. Zhou, I. Sarpkaya, A. Martinez, I. Liao, B. N. Davis, J. Martinez, D. Martinez-Ta, A. Guan, A. E. Nguyen, K. Liu, C. Soci, E. Reed, L. Bartels, V. J. Sorger, *ACS Photonics* **2017**, *4*, 1713.
- [197] J.-N. Liu, W.-B. Bu, J.-L. Shi, *Acc. Chem. Res.* **2015**, *48*, 1797.
- [198] J. Huang, K. S. Jackson, C. J. Murphy, *Nano Lett.* **2012**, *12*, 2982.
- [199] A. McLintock, N. Hunt, A. W. Wark, *Chem. Commun.* **2011**, *47*, 3757.
- [200] J. Zhang, Z. Zhao, Z. Xia, L. Dai, *Nat. Nanotechnol.* **2015**, *10*, 444.
- [201] J. Suntivich, K. J. May, H. A. Gasteiger, J. B. Goodenough, Y. Shao-Horn, *Science* **2011**, *334*, 1383.
- [202] P. Gu, M. Zheng, Q. Zhao, X. Xiao, H. Xue, H. Pang, *J. Mater. Chem. A* **2017**, *5*, 7651.
- [203] Z. W. Seh, J. Kibsgaard, C. F. Dickens, I. Chorkendorff, J. K. Nørskov, T. F. Jaramillo, *Science* **2017**, *355*, eaad4998.
- [204] P. Gu, Y. Xu, Y. Zhao, W. Liu, H. Xue, H. Pang, *Adv. Mater. Interfaces* **2017**, *4*, 1700589.
- [205] M. Zeng, Y. Liu, F. Zhao, K. Nie, N. Han, X. Wang, W. Huang, X. Song,

- J. Zhong, Y. Li, *Adv. Funct. Mater.* **2016**, *26*, 4397.
- [206] L. C. Seitz, C. F. Dickens, K. Nishio, Y. Hikita, J. Montoya, A. Doyle, C. Kirk, A. Vojvodic, H. Y. Hwang, J. K. Nørskov, T. F. Jaramillo, *Science* **2016**, *353*, 1011.
- [207] I. Narkeviciute, P. Chakthranont, A. J. M. Mackus, C. Hahn, B. A. Pinaud, S. F. Bent, T. F. Jaramillo, *Nano Lett.* **2016**, *16*, 7565.
- [208] M. Favaro, W. S. Drisdell, M. A. Marcus, J. M. Gregoire, E. J. Crumlin, J. A. Haber, J. Yano, *ACS Catal.* **2017**, *7*, 1248.
- [209] Z. Zhan, Y. Wang, Z. Lin, J. Zhang, F. Huang, *Chem. Commun.* **2011**, *47*, 4517.
- [210] I. Roger, M. A. Shipman, M. D. Symes, *Nat. Rev. Chem.* **2017**, *1*, 0003.
- [211] P. Lianos, *Appl. Catal. B Environ.* **2017**, *210*, 235.
- [212] J. S. Kim, I. Park, E. Jeong, K. Jin, W. M. Seong, G. Yoon, H. Kim, B. Kim, K. T. Nam, K. Kang, *Adv. Mater.* **2017**, *29*, 1606893.
- [213] T. Reier, Z. Pawolek, S. Cherevko, M. Bruns, T. Jones, D. Teschner, S. Selve, A. Bergmann, H. N. Nong, R. Schlögl, K. J. J. Mayrhofer, P. Strasser, *J. Am. Chem. Soc.* **2015**, *137*, 13031.
- [214] A. M. Ullman, C. N. Brodsky, N. Li, S. L. Zheng, D. G. Nocera, *J. Am. Chem. Soc.* **2016**, *138*, 4229.

- [215] Z. Zhuang, W. Sheng, Y. Yan, *Adv. Mater.* **2014**, *26*, 3950.
- [216] B. J. Trzeźniewski, O. Diaz-Morales, D. A. Vermaas, A. Longo, W. Bras, M. T. M. Koper, W. A. Smith, *J. Am. Chem. Soc.* **2015**, *137*, 15112.
- [217] L. Wu, Q. Li, C. H. Wu, H. Zhu, A. Mendoza-Garcia, B. Shen, J. Guo, S. Sun, *J. Am. Chem. Soc.* **2015**, *137*, 7071.
- [218] Y. Kim, D. Dumett Torres, P. K. Jain, *Nano Lett.* **2016**, *16*, 3399.
- [219] S. Yu, A. J. Wilson, J. Heo, P. K. Jain, *Nano Lett.* **2018**, *18*, 2189.
- [220] S. C. Warren, E. Thimsen, *Energy Environ. Sci.* **2012**, *5*, 5133.
- [221] Z. Zhan, F. Grote, Z. Wang, R. Xu, Y. Lei, *Adv. Energy Mater.* **2015**, *5*, 1.
- [222] Z. Zhan, R. Xu, Y. Mi, H. Zhao, Y. Lei, *ACS Nano* **2015**, *9*, 4583.
- [223] Y. Shi, J. Wang, C. Wang, T.-T. Zhai, W.-J. Bao, J.-J. Xu, X.-H. Xia, H.-Y. Chen, *J. Am. Chem. Soc.* **2015**, *137*, 7365.
- [224] J. Guo, Y. Zhang, L. Shi, Y. Zhu, M. F. Mideksa, K. Hou, W. Zhao, D. Wang, M. Zhao, X. Zhang, J. Lv, J. Zhang, X. Wang, Z. Tang, *J. Am. Chem. Soc.* **2017**, *139*, 17964.
- [225] B. Y. Zheng, H. Zhao, A. Manjavacas, M. McClain, P. Nordlander, N. J. Halas, *Nat. Commun.* **2015**, *6*, 1.
- [226] J. Cui, R. Jiang, W. Lu, S. Xu, L. Wang, *Small* **2017**, *13*, 1.

- [227] K. M. Choi, D. Kim, B. Rungtaweeworanit, C. A. Trickett, J. T. D. Barmanbek, A. S. Alshammari, P. Yang, O. M. Yaghi, *J. Am. Chem. Soc.* **2017**, *139*, 356.
- [228] J. S. Duchene, G. Tagliabue, A. J. Welch, W. H. Cheng, H. A. Atwater, *Nano Lett.* **2018**, *18*, 2545.
- [229] S. K. Cushing, J. Li, F. Meng, T. R. Senty, S. Suri, M. Zhi, M. Li, A. D. Bristow, N. Wu, *J. Am. Chem. Soc.* **2012**, *134*, 15033.
- [230] G. Liu, P. Li, G. Zhao, X. Wang, J. Kong, H. Liu, H. Zhang, K. Chang, X. Meng, T. Kako, J. Ye, *J. Am. Chem. Soc.* **2016**, *138*, 9128.
- [231] S. Wang, Y. Gao, S. Miao, T. Liu, L. Mu, R. Li, F. Fan, C. Li, *J. Am. Chem. Soc.* **2017**, *139*, 11771.
- [232] Y. Liu, F. Chen, Q. Wang, J. Wang, J. Wang, T. T. Gebremariam, *J. Mater. Chem. A* **2018**, *6*, 10515.
- [233] C. H. Choi, K. Chung, T.-T. H. Nguyen, D. H. Kim, *ACS Energy Lett.* **2018**, *3*, 1415.
- [234] B. S. Hoener, S. R. Kirchner, T. S. Heiderscheit, S. S. E. Collins, W.-S. Chang, S. Link, C. F. Landes, *Chem* **2018**, *4*, 1560.
- [235] M. A. Modestino, S. Haussener, *Annu. Rev. Chem. Biomol. Eng.* **2015**, *6*, 13.

- [236] V. Augugliaro, G. Camera-Roda, V. Loddo, G. Palmisano, L. Palmisano, J. Soria, S. Yurdakal, *J. Phys. Chem. Lett.* **2015**, *6*, 1968.
- [237] Q. Ding, B. Song, P. Xu, S. Jin, *Chem* **2016**, *1*, 699.
- [238] C. Jiang, S. J. A. Moniz, A. Wang, T. Zhang, J. Tang, *Chem. Soc. Rev.* **2017**, *46*, 4645.
- [239] L. Liu, S. Ouyang, J. Ye, *Angew. Chemie - Int. Ed.* **2013**, *52*, 6689.
- [240] Z. Shan, P. S. Archana, G. Shen, A. Gupta, M. G. Bakker, S. Pan, *J. Am. Chem. Soc.* **2015**, *137*, 11996.
- [241] S. Yu, Y. H. Kim, S. Y. Lee, H. D. Song, J. Yi, *Angew. Chemie Int. Ed.* **2014**, *53*, 11203.
- [242] Q. Yang, Q. Xu, S. H. Yu, H. L. Jiang, *Angew. Chemie - Int. Ed.* **2016**, *55*, 3685.
- [243] A. R. Mainar, L. C. Colmenares, O. Leonet, F. Alcaide, J. J. Iruin, S. Weinberger, V. Hacker, E. Iruin, I. Urdanpilleta, J. A. Blazquez, *Electrochim. Acta* **2016**, *217*, 80.

Acknowledgement

First of all, I would like to show great appreciation to my parents Mr Hengjun Gu (顾恒军) and Ms Liying Guo (郭丽英). They devote all they had to my university fund and give me endless help at any time. Without their support, I would not have the opportunity to live and study like this. In addition, I also appreciate the supports from Royal Society of Chemistry, Institute of Physics, University of Strathclyde, University of Illinois at Urbana-Champaign and Yangzhou University for their various supports.

The experience of my PhD study was tough, especially for a chemistry student working in a physics group. Thanks to my kind and patient supervisor Dr Yu Chen and Prof David J. S. Birch. It is not just about paper publication, it is about how to be a scholar and a scientist. I really appreciate their support and advisements from my heart. Meanwhile, the Photophysics group is really a nice family as well as our Physics Department. I have received tremendous help and support from Philip, Yinan, Guoke, Ben, Olaf, Jens and other staffs during the past few years. I must also give special thanks to my supervisor Prof Catherine J. Murphy at University of Illinois at Urbana Champaign. Her patience and wisdom impressed me very much. Our discussions were always fruitful, and without you I would not have the opportunity to work at a renowned lab with top tier colleges.

Finally, I would like to thank all my friends. When I was down, you were still on my side.

Publication List

1. **P. Gu**, D. J. S. Birch and Y. Chen*, Dye-doped polystyrene-coated gold nanorods: towards wavelength tuneable SPASER, *Methods Appl. Fluoresc.*, 2014, 2, 24004.
2. G. Wei, J. Yu, J. Wang, **P. Gu**, D. J. S. Birch and Y. Chen*, Hairpin DNA-functionalized gold nanorods for mRNA detection in homogenous solution, *J. Biomed. Opt.*, 2016, 21, 97001.
3. S. Patibandla, Y. Zhang, A. M. Tohari, **P. Gu**, J. Reilly, Y. Chen, X. Shu*, Comparative analysis of the toxicity of gold nanoparticles in zebrafish, *J. Appl. Toxicol.*, 2018, 38, 1153
4. J. Xu, **P. Gu***, D. J. S. Birch, Y. Chen*, Plasmon-promoted electrochemical oxygen evolution catalysis from gold decorated MnO₂ nanosheets under green light, *Adv. Funct. Mater.*, 2018, 28, 181573
5. **P. Gu***, J. Li, C. J. Murphy*, D. J. S. Birch, Y. Chen*, Revealing the plasmon enhanced fluorescence *via* Mega 520 doped silica-coated GNRs, in preparation

Abbreviations

2D – 2 dimensional

ADC – analog-to-digital converter

APS – ammonium persulphate

AR – aspect ratio

CFD – constant function discriminator

CPE – constant phase-angle element

CTAB – cetyltrimethylammonium bromide

DAPI – 4',6-Diamidino-2-phenylindole

DNA – deoxyribonucleic acid

EIS – electrochemical impedance spectroscopy

EPR – electron paramagnetic resonance

FAM – carboxyfluorescein

fcc – face centre cubic

FRET – Förster resonance energy transfer

GNR – gold nanorod

GNS – gold nanosphere

HER – hydrogen evolution reaction

HRTEM – high resolution transmission electron microscopy

L mode – longitudinal mode

LSPR – localized surface plasmon resonance

LSV – linear sweep voltammetry

Mega 520 – 6-[4-(7-Diethylamino-2-oxo-1-benzopyran-3-ylvinyl)-3-sulfonatopyridinio]hexanoic acid N-succinimidyl ester

MEM – maximum entropy method

MSMs – mesoporous silica nanoparticles

mRNA – messenger ribonucleic acid

OER – oxygen evolution reaction

ORR – oxygen reduction reaction

PGA – programmable gain amplifier

PS – polystyrene

QY – quantum yield

RC – resistance capacitance

Rh 800 – rhodamine 800

RHE – reversible hydrogen electrode

rpm – round per minute

SAED – selected area electron diffraction

SEM – scanning electron microscopy

SET – surface energy transfer

SHE – standard hydrogen electrode

SP – surface plasmon

SPASER – surface plasmon amplification by stimulated emission radiation

STEM – scanning transmission electron microscopy

T mode – transverse mode

TAC – time-to-amplitude converter

TCSPC – time-correlated single photon counting

TEM – transmission electron microscopy

TEOS – tetraethylorthosilicate

XPS – X-ray photoelectron spectroscopy

XRD – X-ray diffraction